EFFECTS OF HALLOYSITE NANOTUBES ON THE MECHANICAL, CRYSTALLIZATION, AND WEATHERING BEHAVIOUR OF POLYLACTIDE

A THESIS SUBMITTED TO
THE GRADUATE SCHOOL OF NATURAL AND APPLIED SCIENCES
OF
MIDDLE EAST TECHNICAL UNIVERSITY

BY

İLKER KAYGUSUZ

IN PARTIAL FULFILLMENT OF THE REQUIREMENTS
FOR
THE DEGREE OF MASTER OF SCIENCE
IN
MICRO AND NANOTECHNOLOGY

AUGUST 2014

Approval of the Thesis:

EFFECTS OF HALLOYSITE NANOTUBES ON THE MECHANICAL, CRYSTALLIZATION, AND WEATHERING BEHAVIOUR OF POLYLACTIDE

Submitted by **İLKER KAYGUSUZ** in partial fulfillment of the requirements for the degree of **Master of Science in Micro and Nanotechnology Department, Middle East Technical University** by,

Prof. Dr. Canan Özgen
Dean, Graduate School of **Natural and Applied Sciences**

Prof. Dr. Tayfun Akın
Head of Department, **Micro and Nanotechnology**

Prof. Dr. Cevdet Kaynak
Supervisor, **Metallurgical and Materials Eng. Dept., METU**

Prof. Dr. Necati Özkan
Co-Supervisor, **Polymer Science and Technology Dept., METU**

Examining Committee Members:

Prof. Dr. Göknur Bayram
Chemical Engineering Dept., METU

Prof. Dr. Cevdet Kaynak
Metallurgical and Materials Engineering Dept., METU

Prof. Dr. Necati Özkan
Polymer Science and Technology Dept., METU

Assoc. Prof. Dr. Burcu Akata Kurç
Micro and Nanotechnology Dept., METU

Assist. Prof. Dr. İrem Erel Göktepe
Chemistry Dept., METU

Date: 29.08.2014

I hereby declare that all information in this document has been obtained and presented in accordance with academic rules and ethical conduct. I also declare that, as required by these rules and conduct, I have fully cited and referenced all material and results that are not original to this work.

Name, Last name: İlker Kaygusuz
Signature:

ABSTRACT

EFFECTS OF HALLOYSITE NANOTUBES ON THE MECHANICAL, CRYSTALLIZATION, AND WEATHERING BEHAVIOUR OF POLYLACTIDE

Kaygusuz, İlker
M.S., Department of Micro and Nanotechnology
Supervisor: Prof. Dr. Cevdet Kaynak
Co-supervisor: Prof. Dr. Necati Özkan
August 2014, 99 pages

The purpose of the first part of this thesis was to investigate the usability of industrially friendly twin screw extruder melt compounding method and injection molding melt shaping method to produce polylactide (PLA) / halloysite nanotube (HNT) composites for engineering applications. One of the main problems of PLA to be used in engineering applications is its inherent brittleness. Therefore, another goal was to reveal the effects of HNTs on the significant thermal and mechanical engineering properties of PLA nanocomposites, including fracture toughness values. Various procedures applied revealed that these industrial methods could be used successively in the production of PLA/HNT nanocomposites. Mechanical tests and thermal analyses indicated that engineering performance of these nanocomposites could be improved for the use in many applications. For instance, by using only 3 wt% HNT, the increase are 25% in flexural modulus, 54% in fracture toughness, 39% in storage modulus, and 100% in crystallinity amount.

The purpose of the second part of this thesis was to investigate influences of HNTs on the (i) isothermal and (ii) non-isothermal crystallization kinetics of PLA by DSC analyses, and (iii) crystallinity of injection molded and then annealed specimens by DSC and XRD analyses. Due to basically very effective heterogeneous nucleation effect, addition of HNTs resulted in significant increases in the crystallinity of PLA under all three cases. Crystallization time parameters and Avrami rate constants indicated that crystallization rate increased under isothermal crystallization while it decreased under non-isothermal crystallization due to the delayed conformational mobility of PLA chains by the physical barrier actions of HNTs. Avrami exponent also revealed that two-dimensional growth mechanism of crystallites transformed into three-dimensional growth during non-isothermal crystallization while there was no change during isothermal crystallization. Crystallinity determinations of the injection molded and then annealed specimens indicated that, the highest crystallinity degree of PLA, i.e. 47%, could be reached by the addition of only 1 wt% HNT.

The purpose of the third part of this thesis was to explore consequences of accelerated weathering on the behavior of PLA/HNT nanocomposites. Behaviors of the specimens were compared before weathering and after exposure to UV irradiation and humidity steps according to Cycle-C of ISO 4892-3 standards for a total duration of 300 hours. IR studies revealed that photolysis and partly hydrolysis were the main degradation mechanisms leading to random main chain scission of the PLA macromolecular structure, which was reflected with drastic reductions in the mechanical properties of flexural strength and fracture toughness. On the other hand, no reductions were observed in the values of thermal degradation temperatures, storage modulus and flexural modulus of the specimens, which was due to the compensating effect of higher amounts of crystallinity formed during UV irradiation cycles at 70°C.

Keywords: Polylactide, Halloysite Nanotubes, Fracture Toughness, Crystallization Kinetics, Accelerated Weathering

ÖZ

HALOYSİT NANOTÜPLERİN POLİLAKTİTİN MEKANİK, KRİSTALLENME VE ATMOSFERİK YAŞLANMA DAVRANIŞLARINA ETKİLERİ

Kaygusuz, İlker
Yüksek Lisans, Mikro ve Nanoteknoloji Bölümü
Tez Yöneticisi: Prof. Dr. Cevdet Kaynak
Ortak Tez Yöneticisi: Prof. Dr. Necati Özkan
Ağustos 2014, 99 sayfa

Bu tezin ilk bölümünün amacı endüstriyel tarzdaki çift-vidalı ekstrüder ile eriyik kompaundlama ve enjeksiyon kalıplama ile eriyik şekil verme yöntemlerinin polilaktit (PLA)/ haloysit nanotüp (HNT) kompozitlerinin üretilebilirliğinin mühendislik uygulamaları açısından araştırılmasıdır. PLA polimerinin mühendislik uygulamalarında kullanılması açısından en önemli sorunlardan biri doğasında olan kırılganlığıdır. Bu yüzden, bir diğer amaç HNT'lerin PLA nanokompozitlerinin mühendislik açısından önemli olan, kırılma tokluğu dahil, mekanik ve ısıl özellikleri üzerindeki, etkilerini incelemektir. Uygulanan çeşitli işlemler bu endüstriyel yöntemlerin PLA/HNT nanokompozitlerinin başarılı bir şekilde üretilebilimesi için kullanılabilir olduklarını ortaya çıkartmıştır. Mekanik testler ve ısıl analizler bu nanokompozitlerin mühendislik performanslarının bir çok uygulamada kullanılabilecek düzeyde iyileştirilebileceğini göstermiştir. Örneğin, ağırlıkça yalnızca %3 HNT ile eğme modülünde %25, kırılma tokluğunda %54, depolama modülünde %39, ve kristallenme miktarında %100 yükselmeler görülmüştür.

Tezin ikinci bölümünün amacı ise HNT'lerin PLA'nın (i) eşısıl ve (ii) eşısıl olmayan kristallenme kinetiklerinin ve (iii) enjeksiyon kalıplama sonrası tavlanmış numunelerin kristallenmeleri üzerindeki etkileri DSC ve XRD analizleri ile incelenmiştir. Özellikle HNT'nin çok etkin heterojen çekirdeklendirme etkisine bağlı olarak, her üç durumda da, PLA'ya HNT eklenmesi kristallenme miktarlarında önemli artışlara yol açmıştır. Kristalizasyon zaman parametreleri ve Avarami hız sabitleri kristalizasyon hızının eşısıl durumda arttığını eşısıl olmayan durumda ise azaldığını göstermişlerdir. Bu azalmanın nedeni PLA zincirlerinin kristalizasyon için gerekli olan konformasyonel hareketliliğinin HNT'lerin fiziksel bariyer etkisi ile geciktirilmesidir. Avrami üssü ayrıca kristallerin iki-boyutlu büyüme mekanizmasının eşısıl kristalizasyon sırasında bir değişiklik göstermediğini, eşısıl olmayan kristalizasyon sırasında ise üç-boyutlu büyüme mekanizmasına dönüştüğünü ortaya çıkarmıştır. Enjeksiyon kalıplama sonrası tavlanmış numunelerin kristallenme miktar ölçümleri, PLA'in sahip olabileceği en yüksek kristallenme miktarı olan %47 düzeyine ağ. %1 HNT eklenmesi ile ulaşılabildiğini göstermiştir.

Tezin üçüncü bölümündeki amaç ise hızlandırılmış atmosferik yaşlandırmanın PLA/HNT nanokompozitlerinin davranışı üzerindeki sonuçlarının incelenmesidir. Numunelerin davranışları yaşlandırma öncesi ve sonrası durumları için karşılaştırılmıştır. Hızlandırılmış atmosferik yaşlandırma işlemi sırasında numunelere ISO 4892-3 standartının Method-C'de belirtilen UV radyasyonu ve nem döngüleri toplam 300 saat boyunca uygulanmıştır. IR çalışmaları PLA'nın makromoleküler yapısında zincir kesilmeleri oluşturan degredasyon mekanizmalarının özellikle fotoliz ve kısmen hidroliz ile olduğunu göstermiştir. Bu degradasyon mekanizmalarının nanokompozitlerin eğme dayanımı ve kırılma tokluğu mekanik özelliklerinde çok önemli düşüşlere neden oldukları ortaya çıkmıştır. Diğer taraftan, ısıl degredasyon sıcaklığı, depolama modülü ve eğme modülü değerlerinde düşüş gözlenmemiştir. Bunun nedeni numunelerdeki kristallenme miktarının 70°C de uygulanan UV radyasyonu sırasında artması ve bunun yaşlanma sonucu olan düşüşleri telafi etmesidir.

Anahtar Sözcükler: Polilaktit, Haloysit Nanotüp, Kırılma Tokluğu, Kristallenme Kinetiği, Hızlandırılmış Atmosferik Yaşlandırma

to İlknur and Ateş

ACKNOWLEDGEMENTS

I would like to express my sincere gratitude to my supervisor Prof. Dr. Cevdet Kaynak for his guidance, advice and patience at every stage of this dissertation and the opportunity to become a SAN-TEZ project researcher. I would also acknowledge my co-supervisor Prof. Dr. Necati Özkan for his advices during my experimental works.

I would like to gratefully acknowledge Turkish Ministry of Science, Industry and Technology, and FARPLAS A.S. Automotive Parts Manufacturer, Turkey for the grant with the Project number 01531.STZ.2012-2.

I would like to acknowledge all the technical staff and administrative board of the Metallurgical and Materials Engineering Department for supplying all the research facilities required in this thesis. I would also like to thank to METU Wind Energy Center sincerely for allowing use of DMA equipment; and to METU Central Laboratory for GPC analyses.

I want to give my sincere thanks to my colleagues Dr. Nihat Ali Işıtman and Dr. Osman Polat for they have shown me the true example of how a researcher and an academic should be. I hope to follow in their footsteps in my career for the years to come. I would also like to thank Demirhan Demir, who has shown to be a true friend in hard times and tried to show people aren’t inherently bad.

TABLE OF CONTENTS

LIST OFTABLES

LIST OF FIGURES

NOMENCLATURE

$(1-X_T)$: amorphous phase fraction with respect to temperature

$(1-X_t)$: amorphous phase fraction with respect to time

2θ : XRD diffraction angle

β : cooling rate during non-isothermal crystallization

$dH(t)/dt$: rate of heat evolution

ε_f : strain at break (%)

ΔH_f : measured heat of fusion of the specimens

ΔH_f^0 : heat of fusion of 100% crystalline polymer

ΔH_C, ΔH_{CC} : heat of crystallization

ΔH_{ic} : heat of isothermal crystallization

ΔH_{nic} : heat of non-isothermal crystallization

E : Young’s modulus

E_{Flex} : flexural modulus

E' : storage modulus

G_{IC} : Fracture toughness as Critical Strain Energy Release Rate

σ_{TS} : tensile strength

σ_{Flex} : flexural strength

K : crystallization rate constant

K_c : modified Avrami rate constant

K_{IC} : Fracture toughness as Critical Stress Intensity Factor

n : Avrami exponent

$t_{1/2}$: half crystallization time

t_{max} : maximum rate of crystallization

t_∞ : end time of the crystallization

$T_{1/2}$: half crystallization temperature

$T_{5wt\%}$: thermal degradation temperature at 5 wt% mass loss

$T_{10wt\%}$: thermal degradation temperature at 10 wt% mass loss
$T_{25wt\%}$: thermal degradation temperature at 25 wt% mass loss
T_g : glass transition temperature
$T_{MLR\text{-}max}$, T_d : maximum mass loss rate peak, maximum degradation rate temperature
T_0 : onset temperature of crystallization
Tp : peak temperature of crystallization
T_R : temperature range of crystallization
X_C : degree of crystallinity
X_t : time dependent fractional crystallinity
w_{PLA} : weight fraction of polymer

ATR-FTIR : attenuated total reflection-Fourier transform infrared spectroscopy
DMA : dynamic mechanical analysis
DSC : differential scanning calorimetry
DRA : diffuse reflectance analysis
DTA : differential thermogravimetric analysis
HNT : halloysite nanotubes
PLA : polylactide, poly (lactic acid)
ROP : ring opening polymerization
SEM : scanning electron microscopy
TEM : transmission electron microscopy
TGA : thermogravimetric analysis
XRD : X-ray diffraction analysis

CHAPTER 1

INTRODUCTION

1.1 Polylactide

Petroleum based synthetic polymers are produced around 140 million tons per year. They require long periods of time before they degrade, and their discharge after usage poses an environmental problem. This issue led the researchers to biosource and biodegradable polymers.

Poly(lactic acid) or simply named as polylactide (PLA) is widely used in food, medicine, textiles, leather and chemical industries. Lactic acid monomer can be found in two optical active isomers, L- and D- enantiomers, as shown in Figure 1.1. These two enantiomers can be obtained from starch based sources, such as wheat, corn, rice, and molasses, and from cellulose by bacterial fermentation.

There are several methods used to produce polylactide from lactic acid. Two most widely used ones are direct polycondensation of lactic acid and ring opening polymerization (ROP) of lactic acid cyclic dimmer (lactide) [1]. Figure 1.2 shows basic reactions of these methods. Direct condensation requires solvent and higher reaction times, while resulting in low to intermediate molecular weight polymers. ROP of the lactide needs a catalyst. Molecular weight and D- and L- lactic acid ratio can be controlled through this method. An example of proposed mechanism of ROP of

Lactide with 4-(dimethylamino) pyridine (DMAP) and N-Heterocyclic carbene (NHC) as catalysts are shown in Figure 1.3 [2].

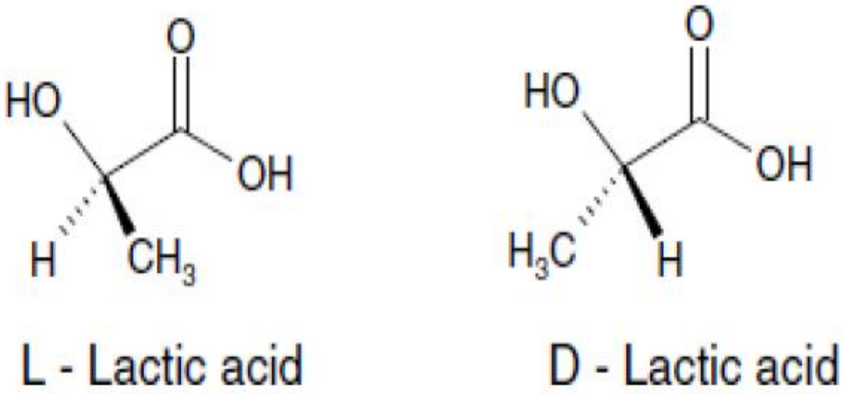

Figure 1.1 Two different optical isomers of PLA monomer

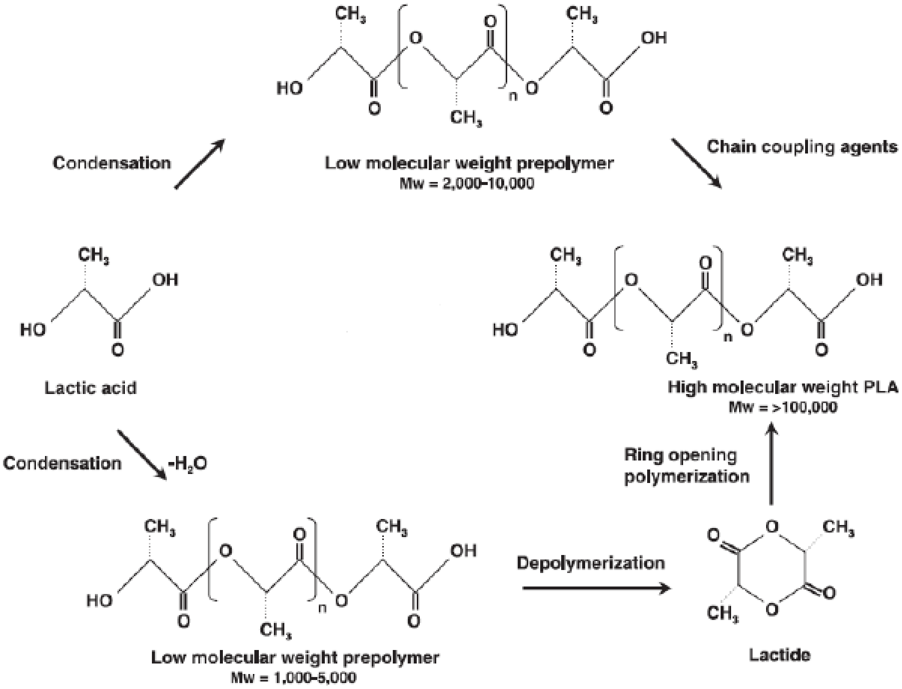

Figure 1.2 Direct condensation and ROP of lactic acid [1]

PLA is an aliphatic polyester with thermoplastic character. Exposure of water and heat can hydrolyze the polyester chains to lower molecular weight oligomers [3]. Apart from toughness other mechanical properties of PLA are comparable with the polymers from petro-chemical based counterparts. However, mechanical properties of PLA show very large scatter depending on the production method and the consequent molecular weight level. On the other hand, the thermal properties of PLA do not vary significantly with the production method. PLA usually have a glass transition temperature (T_g) around 60°C, melting temperature (T_m) around 170°C and a thermal degradation temperature (T_d) around 240°C.

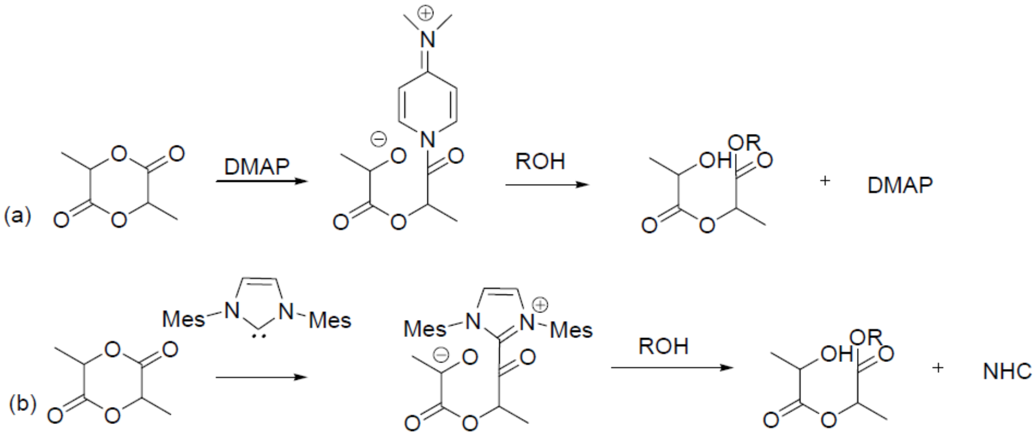

Figure 1.3 ROP of lactic acid with DMAP and NHC as catalysts [2]

PLA is an easy-to-process material compared to other biopolymers. Injection molding, extrusion, thermoforming, drawing and film forming process can be carried out, which means that PLA can be transformed into a desirable shape depending on its application area.

In terms of structural engineering applications, PLA has some challenging properties, such as brittleness, very slow crystallization rate, and rather low weathering resistance. Therefore, in this thesis, toughness, crystallization kinetics, and weathering behavior of PLA were investigated by exploring the influences of halloysite nanotube (HNT) reinforcements.

1.2 Crystal Structure of PLA

The chemical structure of many commercial grade PLA produced are poly(L-lactic acid), and depending on the processing conditions it can crystallize in three different forms; α, β and γ [4-10].

The β phase forms under mechanical stretching during crystallization, corresponding to a fibrillar morphology. To obtain this crystal structure, hot-drawing at high temperatures and high stresses were necessary, as cold drawing at room temperature was not possible [4]. The proposed chain conformations for the β crystal structure is left-handed 3/1 helices as shown in Figure 1.4.

The formation of γ phase is also observed to occur under special circumstances [8]. For instance, epitaxial growth on hexamethylbenzene at 140°C is shown to produce γ-phase crystals. An asymmetrical pattern relative to the chain axis is observed. It is proposed that γ form is based on a three-fold helix conformation [8].

The most common and stable crystal structure of PLA under normal conditions is the α phase. It can develop upon melt or cold crystallization, or from the solution. The unit cell parameters of PLA are not well established. Proposed structures are either pseudo-orthorhombic or orthorhombic having 10_3 helical conformation [6, 10, 11]. Projection of proposed orthorhombic unit cell on ab plane is shown in Figure 1.5 [11], while a chain model of pseudo-orthorhombic conformation is shown in Figure 1.6 [10].

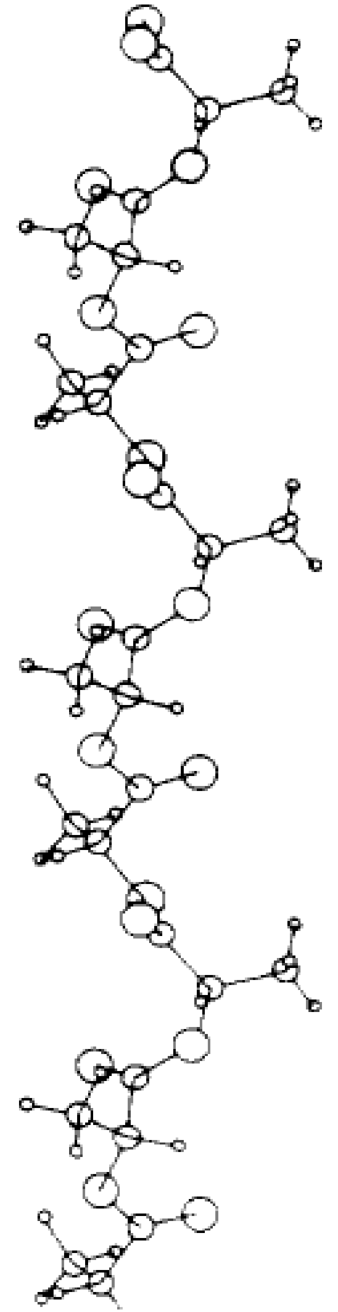

Figure 1.4 Projections along the proposed helical axis of 3/1 helical conformation of the PLA β crystal structure [4]

In the literature there is another PLA crystal phase, named as α′ [12, 13]. It is stated that α′ is observed when the crystallization temperature is below 110°C leading to the loosely packed helical conformation of α phase, resulting in “disordered” structure. The 2θ locations for α and α′ phases are the same and observed at 16.3° and 18.7° assigned to (200/110) and (203) planes, respectively.

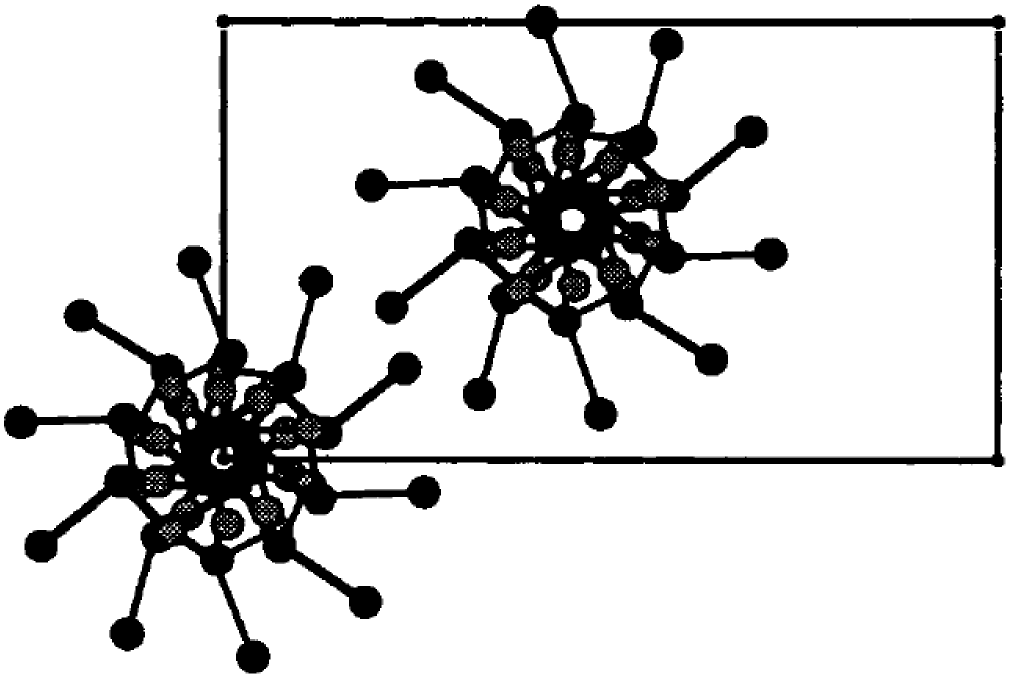

Figure 1.5 Projection of proposed orthorhombic unit cell of PLA α-crystal structure on the ab plane. Full circles: carbon atoms; dotted circles: oxygen atoms [11].

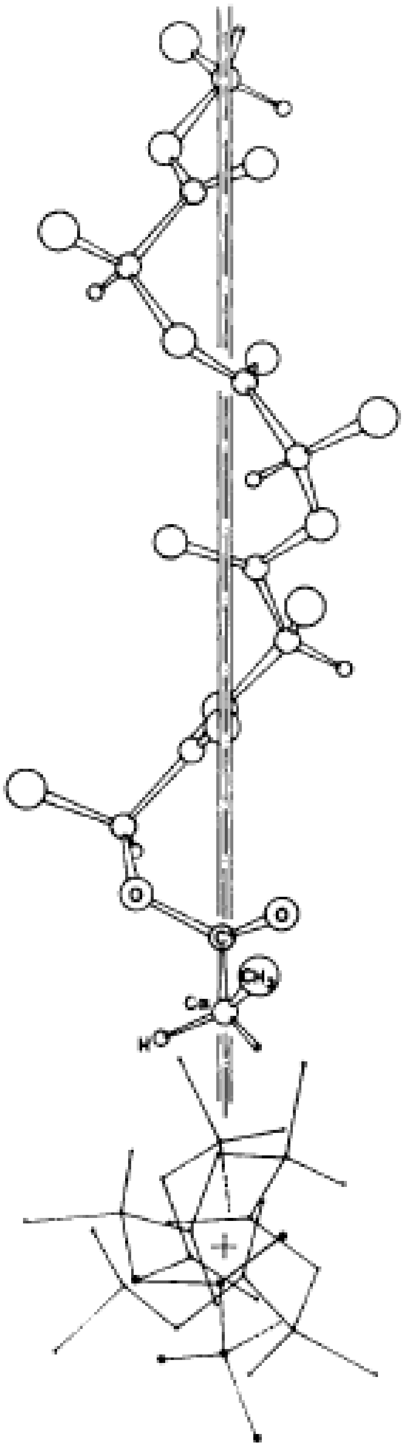

Figure 1.6 Proposed chain conformation of the orthorhombic PLA α-crystal structure [10]

1.3 Weathering of PLA

Weathering of PLA has become a subject of interest with the increase of outdoor applications of PLA. It is thought that there would be two basic degradation mechanisms of weathering; the first one is “photolysis” due to the UV irradiation of sunlight, and the second one is “hydrolysis” due to the environmental moisture.

One of the first UV degradation mechanisms proposed by Ikada [14] was mainchain scission by absorption of photons which is associated with the Norrish II type photo cleavage. The reaction scheme for this mechanism is given in Figure 1.7 [14].

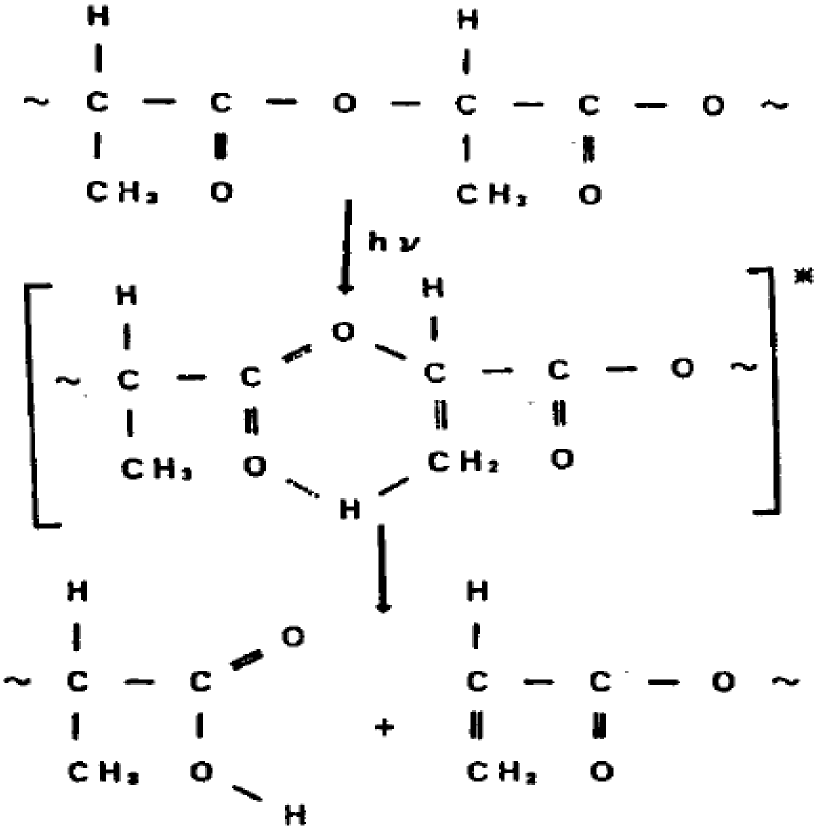

Figure 1.7 Reaction scheme for the photodecomposition of PLA [14]

Then Janorkar et. al. [15] proposed a more detailed mechanism called as “photolysis”. As shown in Figure 1.8, this mechanism leads to the breakage of the C-O backbone bonds, resulting in large decreases in molecular weight and thus deteriorated properties.

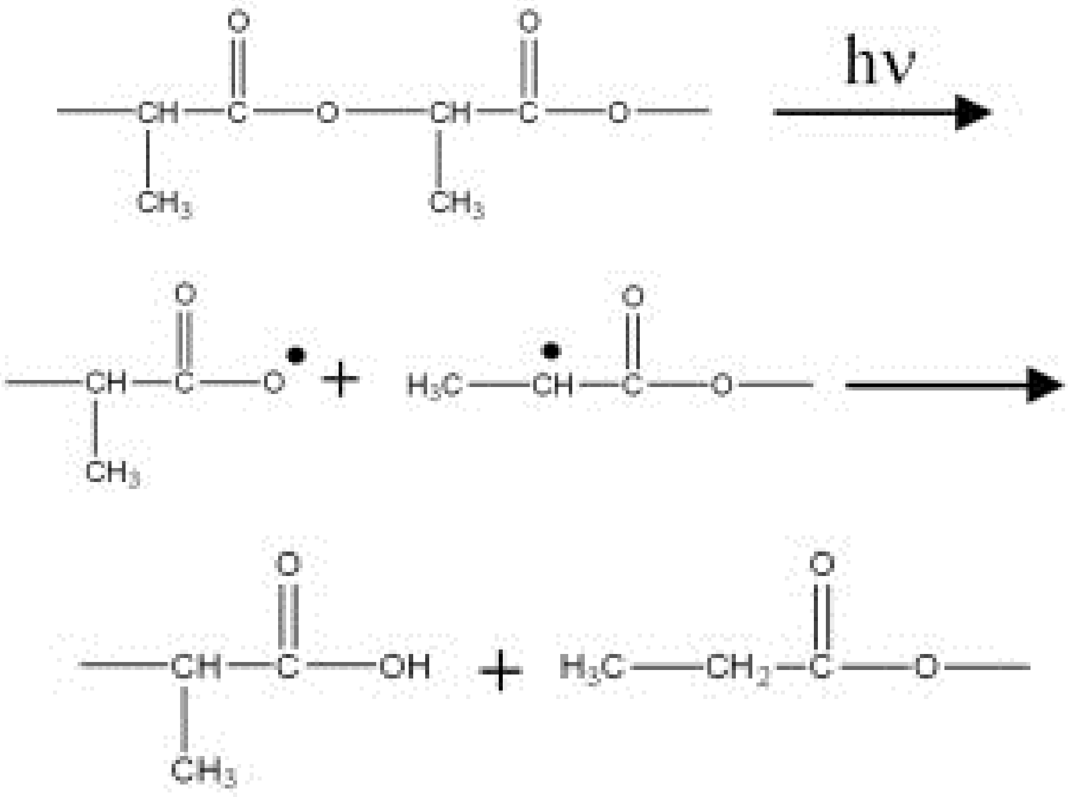

Figure 1.8 Reaction schemes for the photolysis of PLA [15]

Furthermore, they indicated that “photooxidation” could be a simultaneous UV degradation mechanism [15]. As shown in Figure 1.9, this mechanism leads to the formation of carboxylic acid and ketone end groups. A further photolysis of ketone groups may lead to the cleavage of C-C bonds again all leading to deteriorated properties

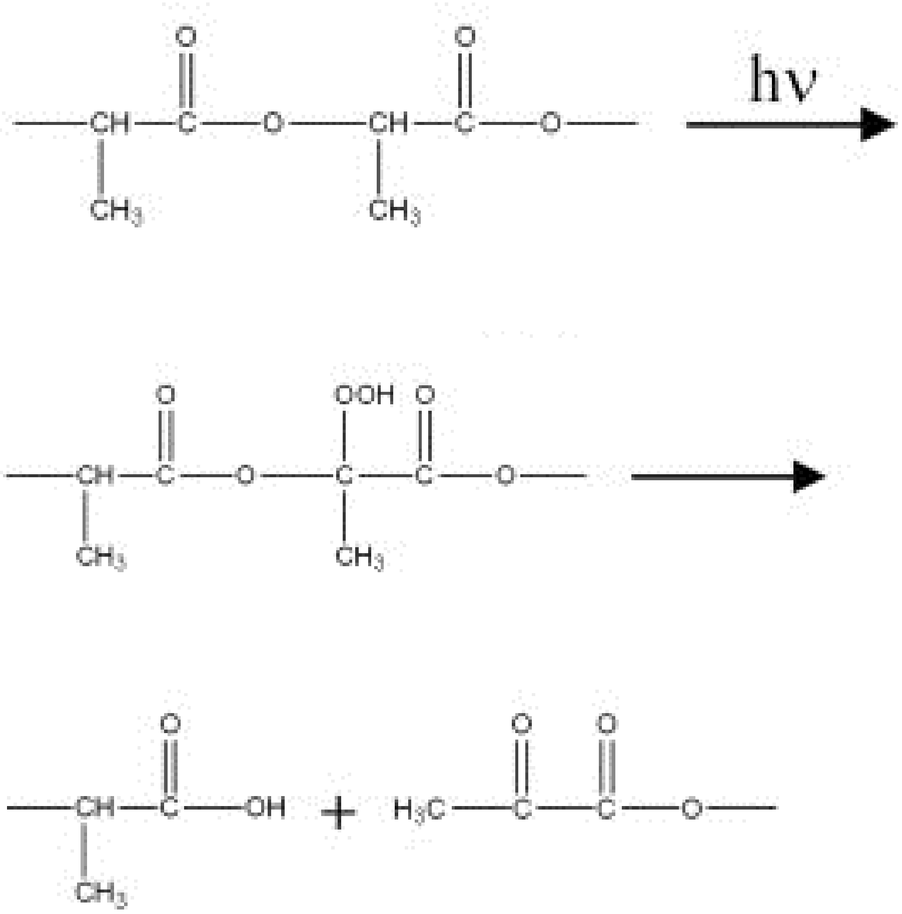

Figure 1.9 Reaction scheme for the photooxidation of PLA [15]

Hydrolysis of the PLA is another important degradation mechanism that should be under consideration during outdoor use. During hydrolysis, ester groups (C-O bonds) are broken [16, 17], leading to the formation of carboxylic acid and diketone end groups. Also, certain hydrophobic property changes are expected to occur in PLA depending on the stretching of $–CH_3$ groups. Temperature and humidity is also known to play an important role on the rate of degradation. It is also stated that if hydrolysis takes place at much higher temperatures then there would be certain resistance of ester bonds against hydrolysis. [17].

During weathering, crystallinity amount of PLA might increase due to two reasons. One reason is that, UV irradiation and outdoor temperature might reach to the cold crystallization start temperature of PLA, which is around 70°C. Another reason could be much higher mobility of the short chains of PLA occurred due to chain scissions. In the literature, the latter crystallization mechanism is cited as "cleavage-induced crystallization" [18, 19].

1.4 Halloysite Nanotubes

Halloysite nanotubes (HNTs) are 1:1 type (silica tetrahedral and gibbsitic octahedral) naturally occurring clay minerals having tubular shape. Even though most commonly observed shape is nanoscale tubular structure, the halloysite mineral can have other morphologies depending on the crystallization and geological conditions [20-24]. These morphologies include spheroidal and plate like structure.

Chemical groups of the crystal layers present in HNT structure are given in Figure 1.10, while the TEM images of HNTs used in this study are shown in Figure 1.11. Normally there is weakly bonded monolayer of water molecules between their rolled walls, which may easily dehydrate at room conditions. Chemical formula of HNTs can be expressed as $Al_2Si_2O_5(OH)_4.nH_2O$, where n is equal to 2 or 0 for hydrated and dehydrated states, respectively. Hydrated HNTs have interlayer spacing of 10 Å, whereas it is 7 Å for completely dehydrated ones. As surface groups concerned, HNTs have hydroxyl groups on the inner surfaces, and have Si groups on the outer surfaces [25-32].

Other typical properties of HNTs are; inner diameter 10–30 nm, outer diameter 50–100 nm, length 150–3000 nm, and cation exchange capacity (CEC) of 8–58 meq/100 g.

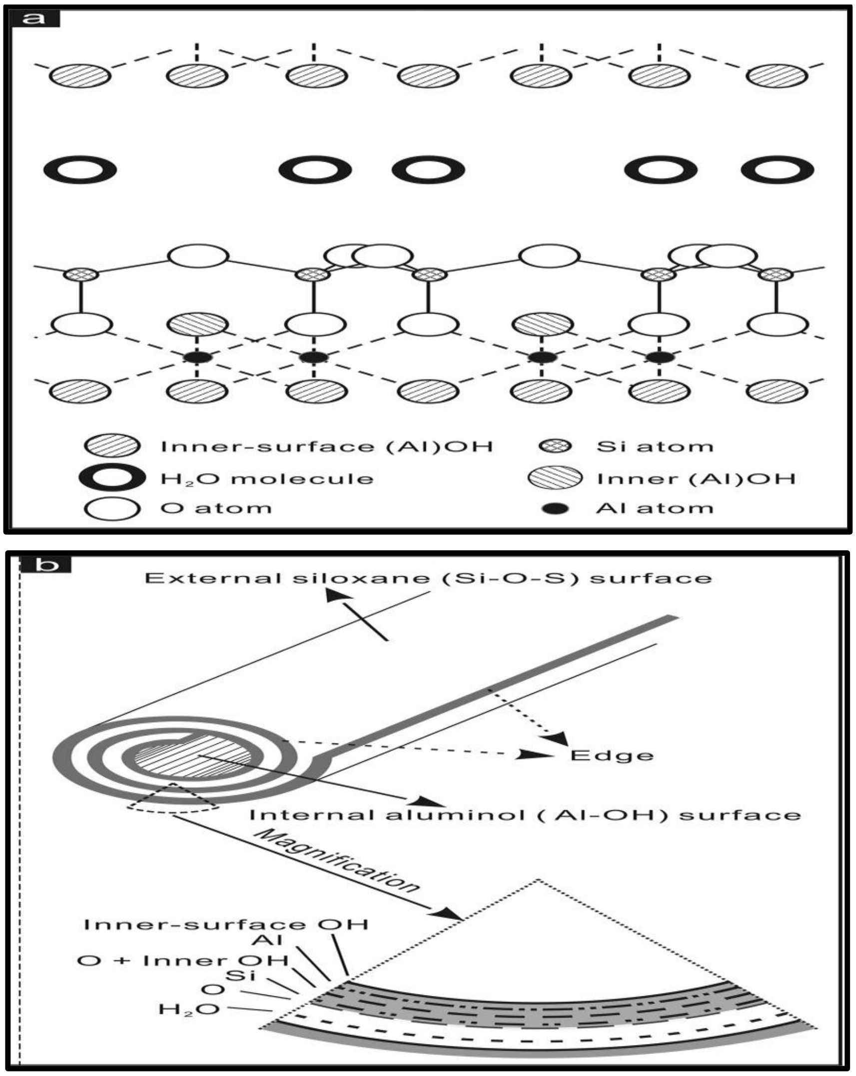

Figure 1.10 Chemical groups in the crystal structure of HNTs; (a) planar, (b) rolled views [32]

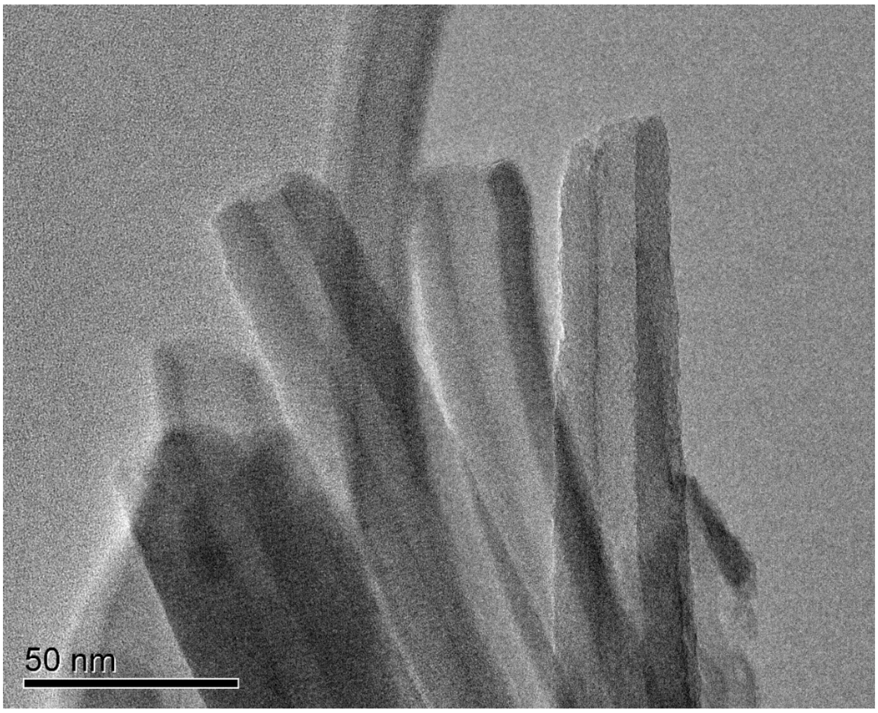

Figure 1.11 TEM images of HNTs used in this thesis

1.5 Literature Survey

1.5.1 Studies on the HNT Reinforced Polymers

HNTs have gained popularity as reinforcing agents after the discovery of carbon nanotubes (CNTs), due to their similarity. Even though their aspect ratio isn’t as high as that of CNTs, HNTs provide certain advantages over CNTs. They do not entangle, they do not need cleaning-purifying procedures, and they are naturally occurring and therefore available.

Uses of HNTs in composites have been investigated by a number of researchers. One of these studies investigated the effects of HNTs on potato starch [33]. The results of this study showed that HNTs dispersed well in the starch, and increased its tensile strength.

Another research [34] revealed behavior of the poly(hydroxybutyrate-co-hydroxyvalerate) PHBV / HNT nanocomposites. HNTs again showed good dispersion. Another important result in this paper was that HNTs increased the Young's modulus without a significant decrease in strain at break.

Two other studies investigated the rubber/HNT composites [35, 36]. The first one studied the effects of ionic liquid coated HNTs. The composites with coated HNTs showed faster curing and higher tensile strength, while the hardness was lowered. The second study investigated natural rubber/HNT composites. Their results indicated that the addition of HNTs lead to higher strength up to a point, and increased scorch and cure time.

A biocompatibility study [37] about chitosan/HNT nanocomposites showed that HNT dispersion in chitosan is uniform and well. Tensile properties and glass transition temperature also reported to be increased.

Polypropylene (PP)/HNT nanocomposites have also been investigated [38]. In accordance with most other studies, HNTs again dispersed well in the PP matrix. They also revealed that HNTs can act as nucleation agents, resulting in increased crystallization rate.

Polyaniline-coated HNT composites were prepared [39] by *in situ* method via soapless emulsion polymerization. In this study, especially the effects of ultrasonic agitation on the dispersion of HNTs were investigated.

Fluoroelastomer/HNT nanocomposites were also investigated [40]. This study showed that mechanical properties can be increased up to 10 phr of HNT, above which agglomerations occur.

Recently the effects of aminosilanization of HNTs on the properties of polyamide-6 (PA6) were investigated by Erdoğan et al. [41]. Different silanization parameters were investigated, and the results showed that the optimum silanization parameters can improve the dispersion state of HNTs and interfacial adhesion between the matrix and the reinforcement, leading to increased mechanical properties of PA6.

1.5.2 Studies on the PLA/HNT Nanocomposites

PLA is a novel biodegradable and biocompatible polymer produced from renewable sources making it one of the most widely used research focus in biomedical devices (such as sutures, pins or screws), tissue engineering, and applications in controlled drug release or diagnostics.

However, PLA needs higher mechanical and thermal properties to be used in engineering applications. For this purpose, some researches studying the effects of nano-reinforcing agents such as montmorillonite [42, 43], sepiolite [42, 44], carbon nanotubes [45], and silica [46] have been conducted. These PLA nanocomposite studies simply showed that nano-reinforcements increase mechanical performance of PLA, but there are contradicting results about thermal properties and crystallinity of PLA matrix.

As stated above, HNTs are becoming another candidate as reinforcing filler for PLA matrix nanocomposites. Current research on PLA/HNT nanocomposites mainly focuses on the biomedical applications, especially their usability for the controlled drug release. These limited number of PLA/HNT studies are summarized below.

Qi et al.[47] investigated drug-delivery performance of drug loaded HNTs mixed with a copolymer of PLA, poly(lactic-*co*-glycolic acid) (PLGA), by electrospinning method. They also conducted tensile tests to determine the mechanical properties of PLGA nanocomposites with only 1 wt% HNTs. Authors claimed that alignment of HNTs in the matrix resulted in increased tensile strength and Young's modulus values by 50% and 16%, respectively.

Dong et al. [48] carried out another PLA/HNT study compounded by electrospinning, too. Along with the effects of certain electrospinning parameters, their DSC analyses simply indicated that 5 wt% HNT decreased the cold crystallization temperature of PLA from 123°C to around 115°C, while melting temperature increase from 154° to 171°C.

Roy et al. [49] investigated behavior of PLA/HNT nanocomposite films compounded by solution casting method with various HNT content. Their tensile tests indicated that using 5 wt% HNT may increase %strain at break value as much as 25%; on the other hand, tensile strength of the nanocomposite decreased almost 40%.

Another study carried out by Isitman, Kaynak et al.[50] on the contribution of HNTs to the flammability of flame retarded PLA revealed that using 17 wt% traditional flame retardant together with 3 wt% HNT may improve many flame retardancy parameters. They also added that tensile strength of these specimens increased by 15%, while there was a decrease in the maximum thermal degradation temperature from 359° to 353°C.

Matusik et al. [51] produced PLA nanocomposites with 1 wt% HNTs by solution casting method. They showed that although there was more than 100% increase in the Young's modulus value of PLA, tensile strength decreased by 6%, which was claimed mainly due to the low ratio of HNTs used in a mixture with kaolinite mineral.

Murariu et. al. [52] studied properties of PLA/HNT nanocomposites compounded by melt mixing (using a bench scale kneader) with 3, 6, and 12 wt% HNT contents. Their results indicated that tensile strength can be increased by 5% with 6wt% HNT without a decrease in % elongation at break or impact toughness values, while storage modulus at 50°C can be increased by 37% with 12 wt% HNT. They also revealed that there were no significant changes in the temperatures of glass transition, crystallization, melting, and thermal degradation.

In the study of Liu et al. [53] PLA and HNTs were mixed using an open two-roll mill with a heating unit. HNT contents used were 5, 10, 20, 30 and 40 parts per hundred of polymer (phr). In this study, the use of 40 phr HNT increased tensile strength by up to 37%, and storage modulus at 37°C by more than 100%. Similar to previous research, there were no significant changes in the thermal degradation temperatures, glass transition and melting temperatures, while cold crystallization temperature decreased from 107°C to 103°C.

1.5.3 Studies on the Crystallization Behavior of PLA

PLA is a partially crystalline thermoplastic polymer. As stated before, depending on the processing conditions PLA can crystallize in three different forms; α, β and γ [4-11]. The β and γ phases form under special conditions, for instance if there is a kind of mechanical stretching during crystallization then β phase is favored, while γ phase can form via epitaxial growth on certain substrates [4, 8]. The most common and stable crystal structure of PLA under normal conditions is the α phase. It can develop upon melt or cold crystallization, or from the solution. It is known that the crystal lattice of α phase is orthorhombic, but the dimensions of the lattice parameters and the helical conformation in the unit cell are still not established well [5-7, 10-11].

However, compared to many commercial grade polymers, the most significant problem from the industrial applications aspect is the very slow crystallization rate of

PLA. For instance, the cooling rate used during injection molding of many industrial products is too fast to allow crystallization of PLA.

In order to regulate crystallization of PLA, there are numerous attempts made in the literature [54, 55], such as using organic or inorganic additives [56, 57] including talc [58], $CaCO_3$ [59], montmorillonite [60, 61] carbon nanotubes [62, 63], etc. These studies generally indicated that second phases used might act as nucleation agents so that certain level of crystallization can be obtained.

However, to the best of our knowledge, there is no literature reported yet, investigating the influences of HNTs on the crystallization behavior of PLA.

1.5.4 Studies on the Weathering of PLA

Apart from food packaging and biomedical items stated before, PLA is now being considered as an alternative polymer to be used in other sectors including automotive industry. In this respect, investigating the outdoor performance of PLA, i.e. weathering properties especially the effects of UV exposure and humidity on the mechanical and other properties of PLA becomes crucial.

However, there are still limited number of investigations reported in the literature [14-19] studying the effects of weathering and their degradation mechanisms. It is generally stated that the main degradation mechanism of UV irradiation is the random “main chain scission” in the chemical bonds of PLA backbone by absorption of a photon [14, 15]. Significant decreases in the molecular weight of PLA occur via “photolysis” of C-O and C-C bonds, and/or “photo-oxidation” leading to formation of carboxylic acid and ketones.

The main degradation mechanism of humidity reported in the literature [16, 17] resulting in again reduction in the molecular weight is the “hydrolysis” of especially

C-O bonds in the ester linkages of the PLA structure, that might form also carboxylic acid and ketones.

There are also certain number of studies investigating the natural and accelerated weathering properties of PLA composites reinforced with keratin [19], montmorillonite [64, 65], hemp-fiber [66], rice starch and epoxidized natural rubber [67], cellulose whiskers [67], and condensed tannin [69]. These studies generally indicated that those fillers used usually increased the rate of degradation with no significant influences on the mechanisms.

However, to the best of our knowledge, there is no literature reported yet, investigating the influences of HNTs on the weathering behavior of PLA, either.

1.6 Aim of the Study

The most widely used compounding method in polymer industry is melt mixing via twin screw extruders. However, the literature review discussed above revealed that none of those studies used this method. Therefore, the purpose of the first part of this thesis was to investigate the usability of twin-screw extruder melt compounding method to produce PLA/HNT nanocomposites. Specimens for testing and analyses were shaped by another most widely used shaping method in industry, i.e. injection molding. For this purpose, the effects of three different compounding and shaping parameters were also evaluated.

For the engineering applications one of the most significant disadvantages of PLA is its inherent brittleness. Although certain thermal and mechanical properties of PLA/HNT nanocomposites were measured in the literature given above, their performance in terms of fracture toughness was not investigated. Therefore, another purpose of the first part of this thesis was to reveal the effects of HNTs on the significant thermal and mechanical engineering properties of PLA nanocomposites, including K_{IC} and G_{IC} fracture toughness values.

In the literature, none of the studies investigated crystallization behavior of PLA/HNT nanocomposites. Therefore, the purpose of the second part of this thesis was, as the first time, to explore influences of HNTs on the crystallization of PLA in three manners; (i) isothermal and (ii) non-isothermal melt crystallization kinetics by DSC, and (iii) crystallinity of injection molded and then annealed specimens by DSC and XRD analyses.

Again, there is no study in the literature investigating the weathering behavior of PLA/HNT nanocomposites. In fact, to best of our knowledge, there is no study reported yet investigating the weathering properties of any polymeric material reinforced with HNTs. Therefore, the purpose of the third part of this thesis was, for the first time, to explore weathering behavior of PLA/HNT nanocomposites by comparing their mechanical and thermal properties before and after accelerated weathering tests.

CHAPTER 2

EXPERIMENTAL WORK

2.1 Materials Used

PLA used in this study was a commercial injection molding grade polymer (NaturePlast, PLI 003). Technical data sheet of this PLA indicates that its melting temperature range is 145°-155°C, degradation temperature range is 240°-250°C, melting flow index range at 190° is 35 g/10min, and its density is 1.25 g/cm^3. In order to determine the molecular weight of this PLA, gel permeation chromatography (GPC) (Polymer Laboratories PL-GPC 220) was conducted giving the results of M_w=978 949 and M_n=156 654 with a polydispersity index of 6.25.

HNT used in this study was also a commercial product (Sigma-Aldrich, product no: 685445) with the given properties; diameter range = 30-70 nm, length range= 1-3 µm, surface area = 64 m^2/g, cation exchange capacity = 8.0 meq/g, and density = 2.53 g/cm^3. Transmission electron microscopy (TEM) (Jeol JEM 2100F) used in this study (Figure 2.1) revealed those given diameter and length ranges of the tubular structures.

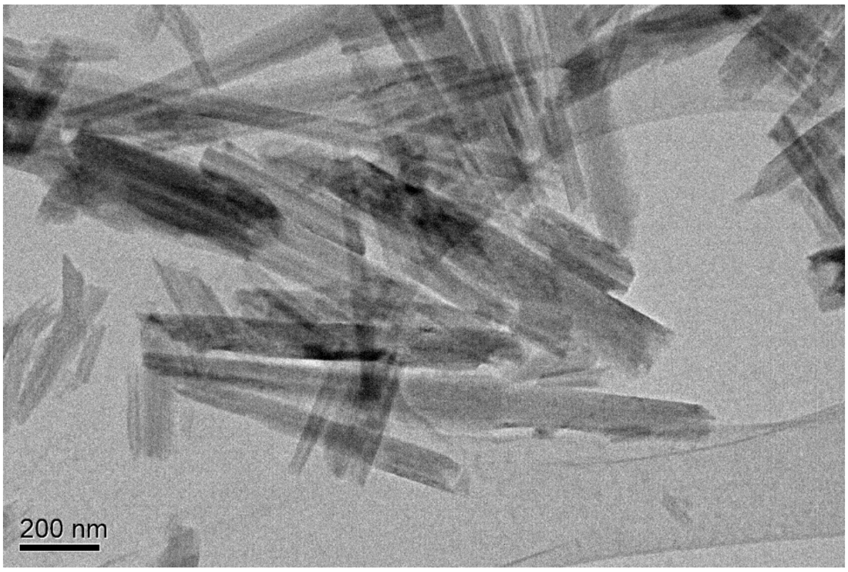

Figure 2.1 TEM image showing diameter and length ranges of the HNTs used

2.2 Compounding and Shaping of PLA/HNT Nanocomposites

PLA nanocomposites were produced with the loadings of 1, 3, 5, 7, and 10 wt% HNTs. These nanocomposites were designated by using the format of "PLA/HNT *x*", where *x* denotes wt% of HNTs used. After several preliminary trials, it was not difficult to determine basic compounding and shaping parameters such as heat profile of twin-screw extruder, barrel and mold temperature of injection molder.

However, effects of other three compounding and shaping parameters (i.e. PLA/HNT dry premixing method prior to melt mixing, twin-screw extruder screw speed during compounding, and drying time prior to injection molding) required special attention. Therefore, these three parameters were investigated in detail to determine their optimum values, and their results are evaluated in Section 3.1.1 of Chapter 3.

Then, all nanocomposites were compounded and shaped using the following optimum parameters: First, PLA granules and HNT powders were pre-dried in a vacuum oven for 12 hours at 60°C and then pre-mixed manually. This mixture was melt compounded via a labsize twin-screw extruder (Rondol Microlab 400) having a screw diameter of 10 mm and L/D ratio of 20. The temperature profile used for this process was 117°-185°-195°-190°-165°C from feeder to die and the screw speed was kept at 80 rpm. Then, the compound was pelletized by using a four-blade cutter into pellets of 2-3 mm.

Before shaping, pellets were re-dried in a vacuum oven for 12 hours at 60°C. Specimens for testing and analyses were shaped by using a laboratory scale injection molder (DSM Xplore Micro). Barrel temperature was selected as 180°C whereas the mold temperature was kept at 35°C. Melting time for the compound in the barrel was 7 minutes, while three-steps pressure-time profile during molding was determined as; 12 bar for 2 s, 10 bar for 5 s, and 10 bar for 5 s, respectively.

2.3 Dispersion Analysis of HNTs by Electron Microscopy

Scanning electron microscopy (SEM) (FEI Nova Nano 430) was conducted in order to observe morphology of fracture surfaces and distribution of HNTs in PLA matrix. Sample surfaces were coated with a thin layer of gold to avoid electrostatic charging and provide conductive surfaces.

2.4 Techniques used for Mechanical Properties

Mechanical tests were carried out to determine significant mechanical properties of all specimens. Tensile and flexural tests were conducted using a 5 kN universal testing machine (Instron 5565A) at a crosshead speed of 1 mm/min according to ISO 527-2 and ISO 178 standards, respectively. K_{IC} and G_{IC} fracture toughness tests were performed on the same machine at a crosshead speed of 10 mm/min according to ISO

13586 standard by using single-edge-notched-bending specimens. On these specimens, required notches and initial precracks were formed by a notching-precracking system (Ceast Notchvis). All mechanical tests were conducted at least for five specimens of each formulation, and the data were evaluated as the average values with standard deviations.

2.5 Techniques used for Thermal Behavior

Three different thermal analyses were carried out to determine the thermal behavior of all specimens. First of all, differential scanning calorimetry analyses (DSC) (SII X-DSC 700 Exstar) were used to determine the important transition temperatures and enthalpies of melting and crystallization of the samples during a heating profile from -50° to 220°C at a rate of 10°C/min under nitrogen flow. Then, thermogravimetric analyses (TGA) (SII TG/DTA 7300 Exstar) were conducted to determine the thermal degradation temperatures of specimens under a heating rate of 10°C/min from 30° to 550°C under nitrogen flow. Dynamic mechanical analyses (DMA) (Perkin Elmer DMA 8000) were also done in order to investigate thermomechanical properties of PLA and its nanocomposite specimens having a size of 40x10x4 mm^3. Analyses were performed in three-point bending mode at a frequency of 1 Hz. The temperature program was run from 20° to 90°C at a heating rate of 2°C/min.

2.6 Techniques used for Crystallization Behavior

The same DSC equipment was used in order to investigate isothermal and non-isothermal melt crystallization kinetics, and crystallinity of injection molded and then annealed PLA and its nanocomposites. Analyses were conducted with an average sample weight of 7-8 mg under nitrogen purge at a constant flow rate of 30 mL/min.

For *isothermal melt crystallization kinetics;* samples were first heated from -50° to 220°C, well above the melting temperature, at a rate of 10°C/min and held at that temperature for 5 min to eliminate any previous thermal history, and then cooled to crystallization temperature (100°C) rapidly at a rate of 50°C/min; and held at this temperature for 30 min until isothermal crystallization was complete. The chosen crystallization temperature of 100°C was determined as an optimum value after a few trials. Heat flow curves as a function of crystallization time were used to study isothermal crystallization kinetics.

For *non-isothermal melt crystallization kinetics;* samples were first heated from -50° to 220°C at a rate of 10°C/min and held at that temperature for 5 min to erase any previous thermal history, followed by cooling to 30°C at a cooling rate of 10°C/min. The chosen non-isothermal cooling rate of 10°C/min was also determined as an optimum value after a few trials. Heat flow curves as a function of temperature during cooling were used to study non-isothermal crystallization kinetics.

For *crystallinity of injection molded and then annealed specimens*; samples were heated to 220°C at a rate of 10°C/min, and this first heating profile was used to determine transition temperatures, melting enthalpies, and crystallinity amounts of the specimens.

Apart from DSC, *X-ray diffraction (XRD) analyses* were also performed in order to determine crystallinity of injection molded and then annealed PLA and its nanocomposites using Rigaku D-Max 2200 X-ray diffractometer with monochromatic CuKa radiation. The anode voltage and current were set at 40 kV and 30 mA, respectively. Diffraction angle 2θ was scanned from 3° to 30° at a scanning speed of 2°/min. In order to estimate amounts of the amorphous phase and α crystalline phase, X-ray intensity versus 2θ data were analyzed by deconvolution, using a profile fitting software PeakFit v.4.11 (SYSTAT Software Incorporation).

2.7 Techniques used for Accelerated Weathering

Weathering tests are used in order to estimate the properties of the materials in the long term use. There are several different types of weathering tests, such as natural weathering, accelerated weathering, UV-only weathering, temperature-only weathering, humidity-only weathering, etc. In these “-only” tests, one of the outdoor parameters is investigated, while in natural and accelerated weathering tests, a combination of UV, temperature, and humidity parameters are explored.

The difference between the natural and the accelerated weathering tests is that, in natural weathering, the specimens are exposed to certain outdoors conditions at certain places for a long period of time, starting from 1 month up to 1 year. On the other hand, in accelerated weathering tests, outdoor conditions are simulated by exposing the specimens to a controlled program with high intensity UV irradiation, temperature, and humidity cycles for much shorter times, starting from 24 hours up to 600 hours.

In this study, an *accelerated weathering tester* (Q-LAB Model QUV/se) was used to investigate the weathering behavior of PLA and its nanocomposites in accordance with the Method-C of the SAE J2020, ASTM G154-05, ISO 4892-3 standards. The schematic of this system is shown in Figure 2.2. Fluorescent lamps (UVB-313) with 0.49 W/m^2 irradiance (at 310 nm) were used with cycles of 8 hr UV irradiation at 70°C, followed by 4 hr dark condensation at 50°C. These consecutive cycles were applied to the specimens attached to the test panels without interruption, for the total duration of 300 hr.

Weathering behavior of the neat PLA and PLA/HNT nanocomposite specimens were compared for the two conditions: “before” and “after”, where “before” means no weathering while “after” means a total accelerated weathering duration of 300 hr.

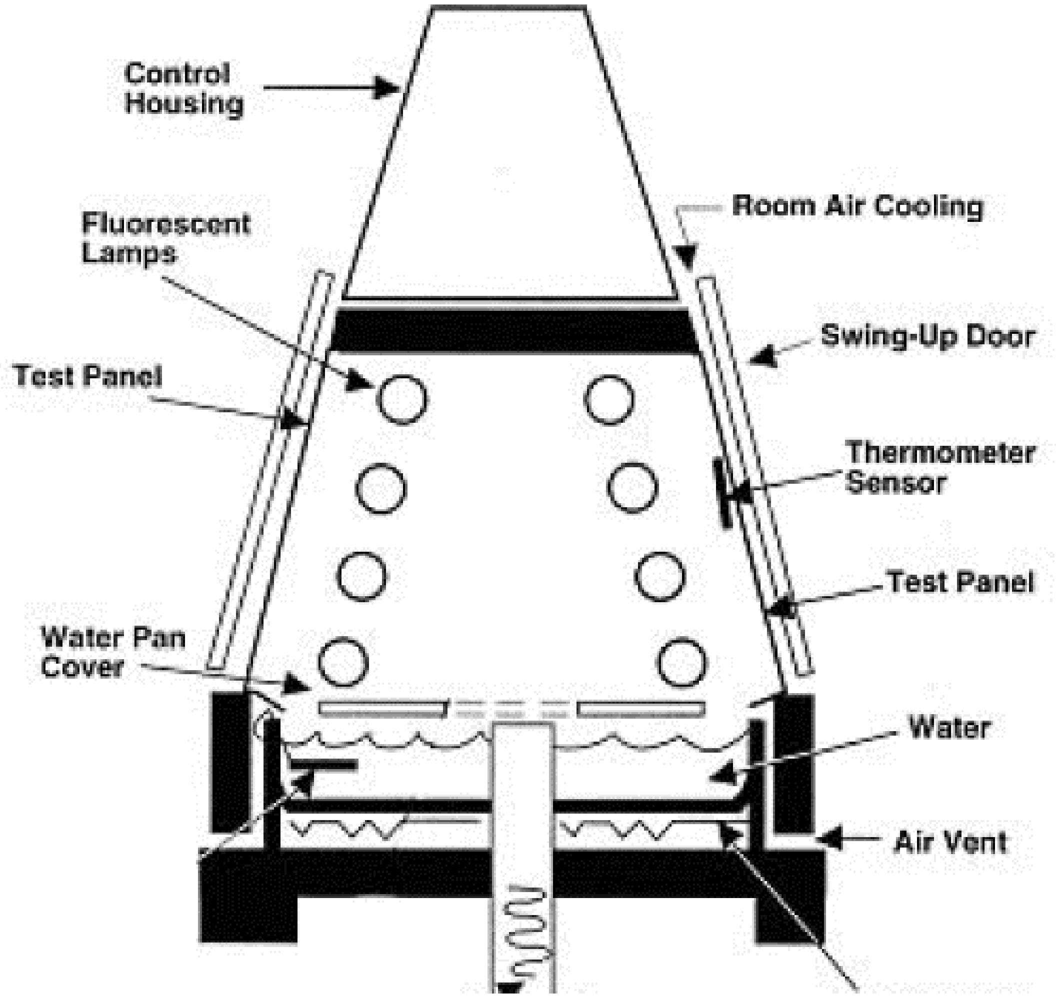

Figure 2.2 Schematic of the accelerated weathering system used in this study [70]

2.8 Techniques used for Changes in Color

The first and the simplest method used to observe the changes in the color of the specimens after accelerated weathering was *macroscopic observation* by photographing their visual images and comparing their color with each other.

The second method used was a quantitavie analysis to determine the CIELab color space parameters (L*, a*, b*) of the specimens before and after weathering, where CIE stands for *Commision Internationale de l'Éclairage*, while the color parameters L*, a* and b* determine the lightness, green-red color and yellow-blue components, respectively. The Lab color space, unlike RGB and CMYK, is designed to approximate human vision. Therefore in order to determine CIELab color parameters, *diffuse reflectance analysis* (DRA) was utilized (via DRA unit of Agilent Cary 60 UV-vis spectrophotometer) in accordance with CIE 1976 standards.

Diffuse reflectance analysis, sometimes known as elastic scattering spectroscopy, is a non-invasive technique that measures the characteristic reflectance spectrum produced as light passed through a medium. The primary mechanisms are absorption, reflection and scattering, all of which vary with wavelength to produce the reflectance spectrum that is recorded. The light is reflected beneath the surface before leaving the material, hence the name diffuse reflectance. This light is collected, and then normalized to the reference light source. A pure white colored standard is recorded for calibration. The light collected from the material is correlated to the pure white standard to obtain the different color wavelengths. Lastly, after the normalization and calibration with respect to light source and pure white standard, the reflectance spectra is converted into color space parameters by the conventions determined by CIE.

2.9 Techniques used for Changes in Chemical Structure

Attenuated total reflectance-Fourier-transform infrared spectroscopy (ATR-FTIR) was used (via ATR unit of Bruker ALPHA) to determine the changes in the chemical bonds of specimens after weathering. A minimum of 32 scans were signal-averaged with a resolution of 4 cm^{-1} in the wavenumber range of 550 to 4000 cm^{-1}.

CHAPTER 3

RESULTS AND DISCUSSION

As stated before, since this thesis has three different parts, their results are presented and discussed successively in the following three subsections.

3.1 Mechanical and Thermal Properties of PLA/HNT Nanocomposites

3.1.1 Effects of Three Compounding and Shaping Parameters

As mentioned in the experimental part, three compounding and shaping parameters were required special attention before investigating the engineering performances of PLA/HNT nanocomposites. These parameters were:

1. PLA/HNT dry-pre-mixing method prior to melt compounding (Manual mixing versus Ball milling)
2. Twin-screw extruder screw speed during melt compounding (25, 50 and 80 rpm)
3. Drying time at 60°C prior to injection molding (12 h versus 24 h)

These three parameters were evaluated by applying eight different procedures which are listed in Table 3.1 in detail. During the lab size twin-screw extruder compounding, the constituents (i.e. matrix granules and reinforcement particles) should be fed into the main feeder together. Therefore, since homogeneity of their dry premixture is important, the first parameter used in the eight different procedures were related to the effects of dry premixing method of the constituents prior to melt compounding. For this purpose, required amounts of PLA granules and HNT powders were premixed by either "manual mixing" or by "ball milling".

Table 3.1. Eight different procedures used to determine the optimum values of three compounding and shaping parameters

Procedures	**PLA/HNT dry pre-mixing method prior to compounding**	**Twin-screw extruder screw speed during compounding (rpm)**	**Drying time at 60°C prior to injection molding (h)**
Procedure 1	Manual	25	12
Procedure 2	Ball Mill	25	12
Procedure 3	Manual	50	12
Procedure 4	Ball Mill	50	12
Procedure 5	Manual	80	12
Procedure 6	Ball Mill	80	12
Procedure 7	Manual	80	24
Procedure 8	Ball Mill	80	24

During melt compounding of nanocomposites, the most significant aspect is to achieve homogeneous distribution of nanoparticles in the molten polymer matrix which is influenced by the shear stress level applied via certain speed of the co-rotating twin-screws. Thus, the second parameter used in the procedures was to evaluate effects of the twin-screw speed of the extruder compounding by comparing rotational screw speeds of 25, 50, and 80 rpm.

It is known that before shaping (e.g. injection molding) of the polymer compounds, they should be dried properly to obtain components without shaping related defects. In this study, since PLA is a biopolymer, a rather lower drying temperature of 60°C in a vacuum oven was selected. However, the period of this drying could be also significant. Therefore, as the third parameter, influences of drying time prior to shaping of the specimens by lab size injection molder were investigated by 60°C vacuum drying for 12 hrs and 24 hrs.

In order to compare effects of these parameters, PLA nanocomposite specimens with only 5 wt% HNTs were produced by using eight different procedures given in Table 3.1. Then, flexural tests were applied to these PLA/HNT 5 nanocomposites produced by each procedure, and the results are tabulated in Table 3.2.

Table 3.2. Flexural mechanical properties of the PLA/HNT 5 nanocomposites produced with eight different procedures

Methods	**Flexural Modulus (GPa)**	**Flexural Strength (MPa)**
Method 1	4.19 ± 0.04	56.2 ± 0.9
Method 2	3.97 ± 0.03	66.5 ± 1.1
Method 3	3.97 ± 0.02	65.7 ± 1.6
Method 4	3.99 ± 0.09	63.9 ± 0.6
Method 5	4.22 ± 0.09	67.3 ± 0.9
Method 6	4.01 ± 0.02	68.0 ± 0.2
Method 7	3.97 ± 0.04	66.5 ± 1.4
Method 8	4.13 ± 0.05	65.9 ± 1.5

Table 3.2 indicates that the optimum flexural strength and modulus were obtained for the specimens produced by Procedure 5, i.e. using “manual mixing” method as dry premixing, using “80 rpm” as twin-screw speed, and using “12 hrs” as drying time before injection. Therefore, these three production parameters together with other parameters explained in the experimental section were used for the production of all nanocomposites in the rest of this study.

3.1.2 Dispersion of HNTs in PLA matrix by Electron Microscopy

Since engineering performance of nanocomposites are strongly dependent on the uniform distribution of nanoparticles, SEM examination was conducted on the fracture surfaces of fracture toughness specimens. SEM fractographs taken rather at a lower magnification of 10000X given in Figure 3.1 show that there is no significant distribution problem in the specimens with low HNT contents. It is seen that when amount of HNTs were above 5 wt%, then certain level of agglomeration may take place.

On the other hand, SEM fractographs taken at a higher magnification of 40000X given in Figure 3.2 reveal the interfacial interactions between the PLA matrix and HNT surfaces. These images simply indicate that HNTs were usually pulled-out basically due to the insufficient interfacial bonding with PLA matrix.

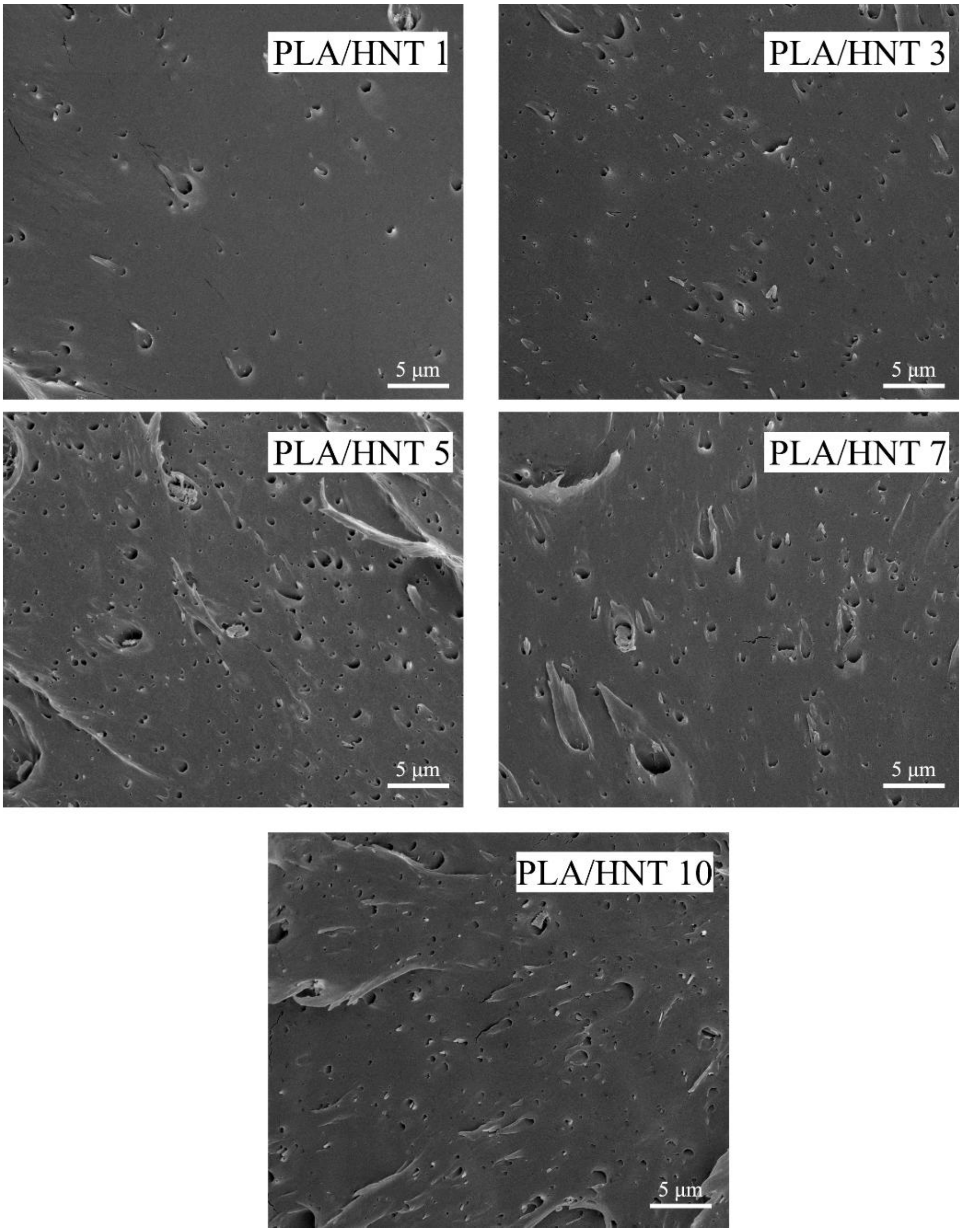

Figure 3.1 SEM fractographs showing dispersion state of HNTs in PLA matrix

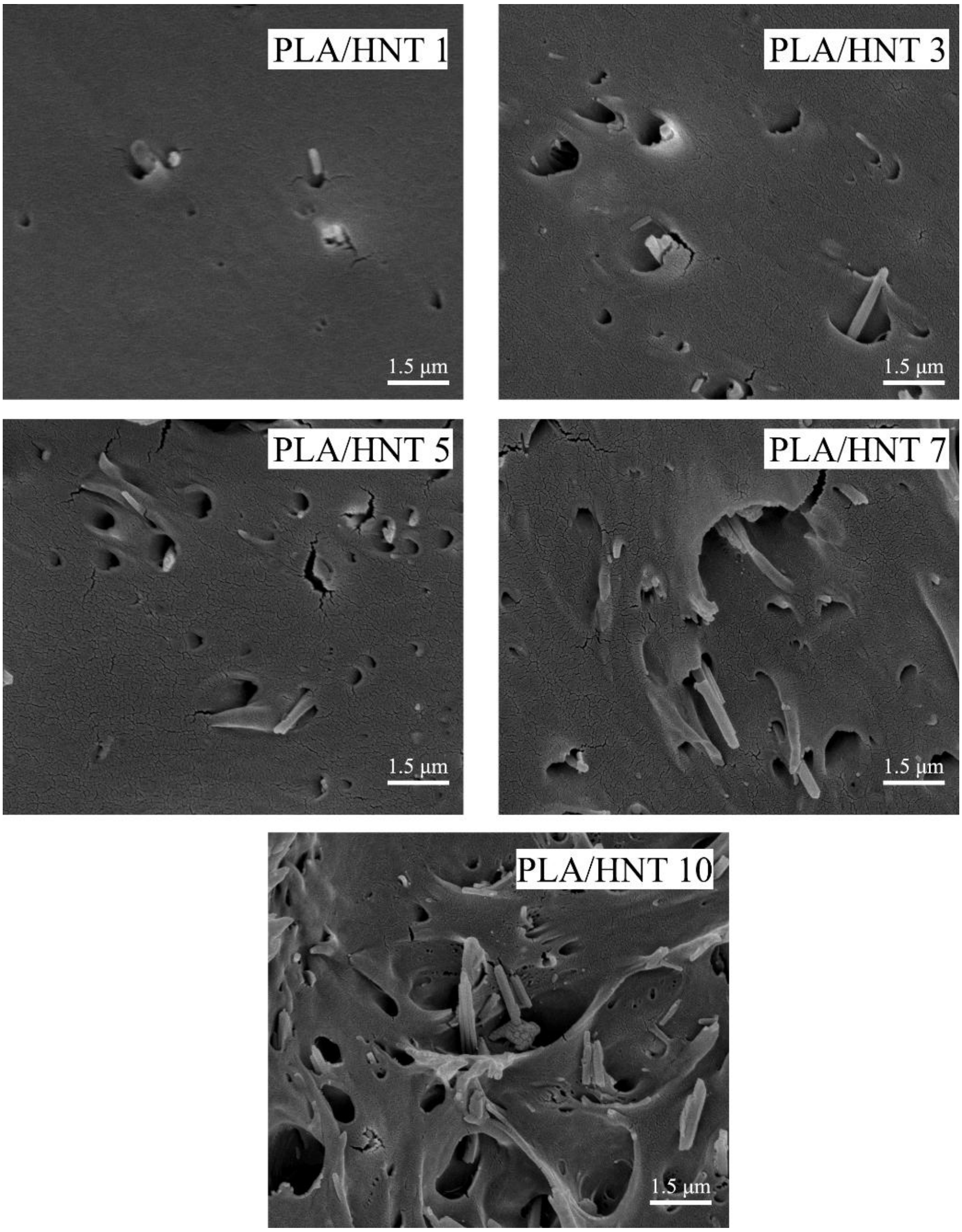

Figure 3.2 SEM fractographs showing pull-out morphology of HNTs in PLA matrix

3.1.3 Mechanical Properties of the Specimens

Elastic modulus and strength of the specimens were examined under two different types of loading; tensile and flexural. That is, both tension and three-point bending tests were applied. Stress-strain curves obtained during these tests were given in Figure 3.3, while values of elastic modules and strength of the specimens determined were tabulated in Tables 3.3 and 3.4. Effects of HNT content on these properties were also evaluated in Figure 3.5.

Table 3.3. Young's Modulus (E), Tensile Strength (σ_{TS}) and Strain at Break (ε_f) values of the specimens

Specimens	E (GPa)	σ_{TS} (MPa)	ε_f (%)
PLA	3.10±0.02	51.43±0.67	1.9 ± 0.03
PLA/HNT 1	3.14±0.06	54.77±1.71	2.5 ± 0.12
PLA/HNT 3	3.16±0.04	55.67±0.63	2.3 ± 0.04
PLA/HNT 5	3.16±0.03	53.47±0.78	2.1 ± 0.06
PLA/HNT 7	3.29±0.12	52.32±2.19	1.9 ± 0.01
PLA/HNT 10	3.44±0.09	51.68±0.06	1.8 ± 0.25

Table 3.4. Flexural Modulus (E_{Flex}) and Flexural Strength (σ_{Flex}) values of the specimens

Specimens	E_{Flex} (GPa)	σ_{Flex} (MPa)
PLA	3.72 ± 0.08	64.17 ± 1.13
PLA/HNT 1	3.94 ± 0.09	69.97 ± 0.97
PLA/HNT 3	4.21 ± 0.04	70.71 ± 0.37
PLA/HNT 5	4.22 ± 0.09	67.32 ± 0.94
PLA/HNT 7	4.29 ± 0.02	66.54 ± 0.37
PLA/HNT 10	4.64 ± 0.08	65.39 ± 1.10

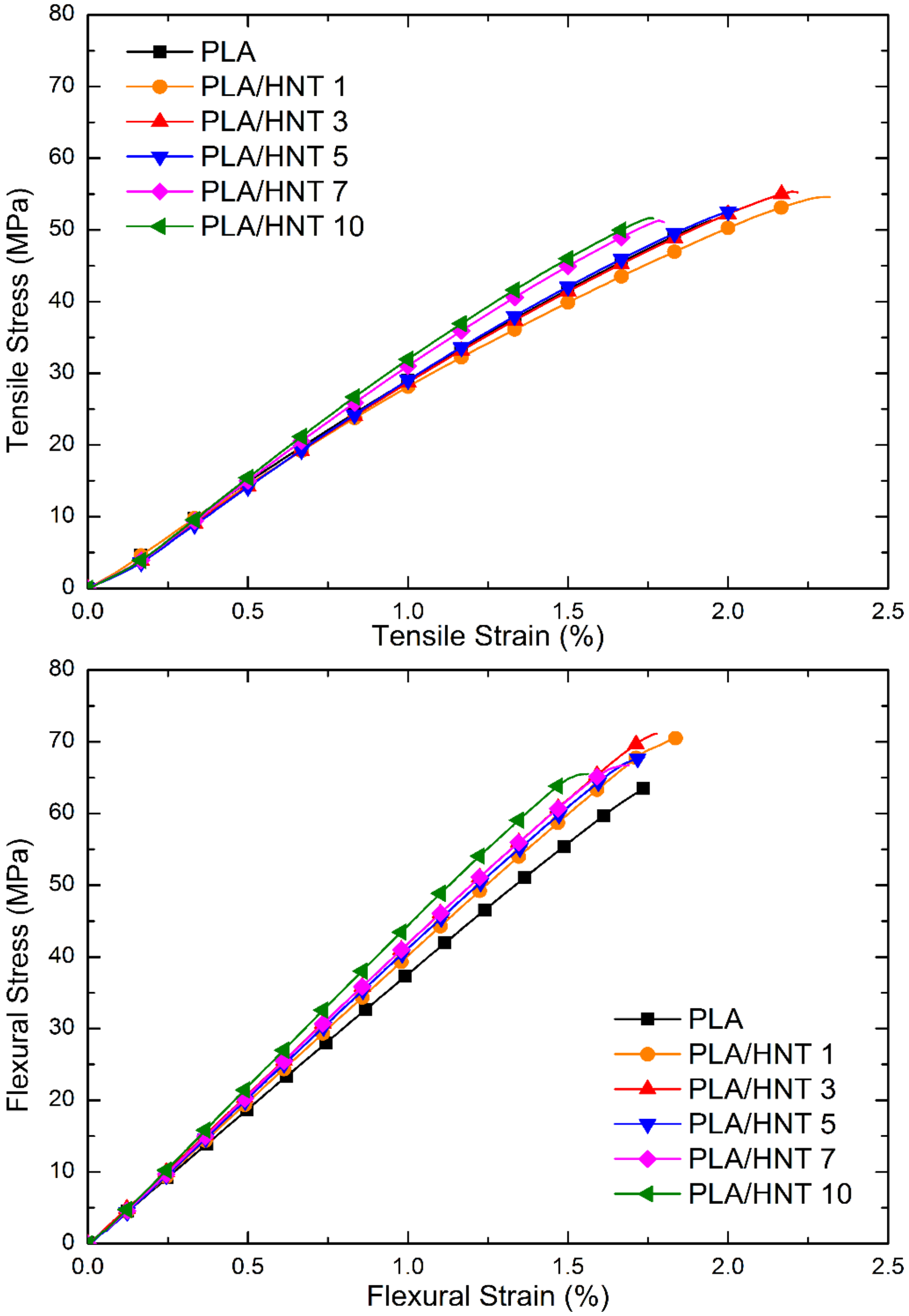

Figure 3.3 Stress-strain curves of the specimens obtained during tensile and three point bending (flexural) tests

These figures and tables indicate that both elastic modulus values, i.e. “Young’s Modulus” (E) determined by tension tests and “Flexural Modulus” (E_{Flex}) determined by bending tests increase almost linearly with the increase of HNT content, basically due to very efficient stiffening effect of rigid HNTs. When the amount of HNT reaches 10 wt%, then E of neat PLA increases by 11%, while this increase in E_{Flex} is as much as 25%.

It was also observed that both “Tensile Strength” (σ_{TS}) and “Flexural Strength” σ_{Flex} of neat PLA increase with the incorporation of HNTs. Since HNT nanoreinforcements are very strong and having relatively high aspect ratio due to their nanotubular structure, both strengthening mechanisms of composites, i.e. “load transfer from the matrix to the reinforcements” and “decrease of the mobility of macromolecular chain structure of matrix polymer”, will be operative. On the other hand, Figure 3.5 shows that the increases in the strength values are not linear. It is especially more significant at lower HNT content. For instance, when 3 wt% HNT was added, σ_{TS} and σ_{Flex} of neat PLA increases 8% and 10%, respectively. At higher HNT contents, e.g. beyond 5 wt% HNT, the improvement in strength values are smaller, due to the difficulty in obtaining very homogeneous distribution of HNTs in the PLA matrix, as discussed in the SEM examination section above.

Table 3.3 shows that there is no detrimental effect of HNT addition on the ductility of PLA matrix. It is seen that “Strain at Break” (ε_f) values of the nanocomposites are not lower than that of the matrix polymer. However, Figure 3.3 indicates that there is no yielding behavior in the tensile stress-strain curves of neat PLA and all PLA/HNT nanocomposites, which is the indication of their brittleness.

The most significant problem of PLA to be used in engineering applications is its inherent brittleness, i.e. low toughness. Therefore, in this study, effects of HNT loading on the toughness of PLA were investigated by fracture toughness tests according to

ISO 13586 standard. Load-deflection curves obtained during these tests are given in Figure 3.4, while "Fracture Toughness" values in terms of both "K_{IC}" (Critical Stress Intensity Factor) and "G_{IC}" (Critical Strain Energy Release Rate) determined from these curves are tabulated in Table 3.5, and effects of HNT content evaluated in Figure 3.5.

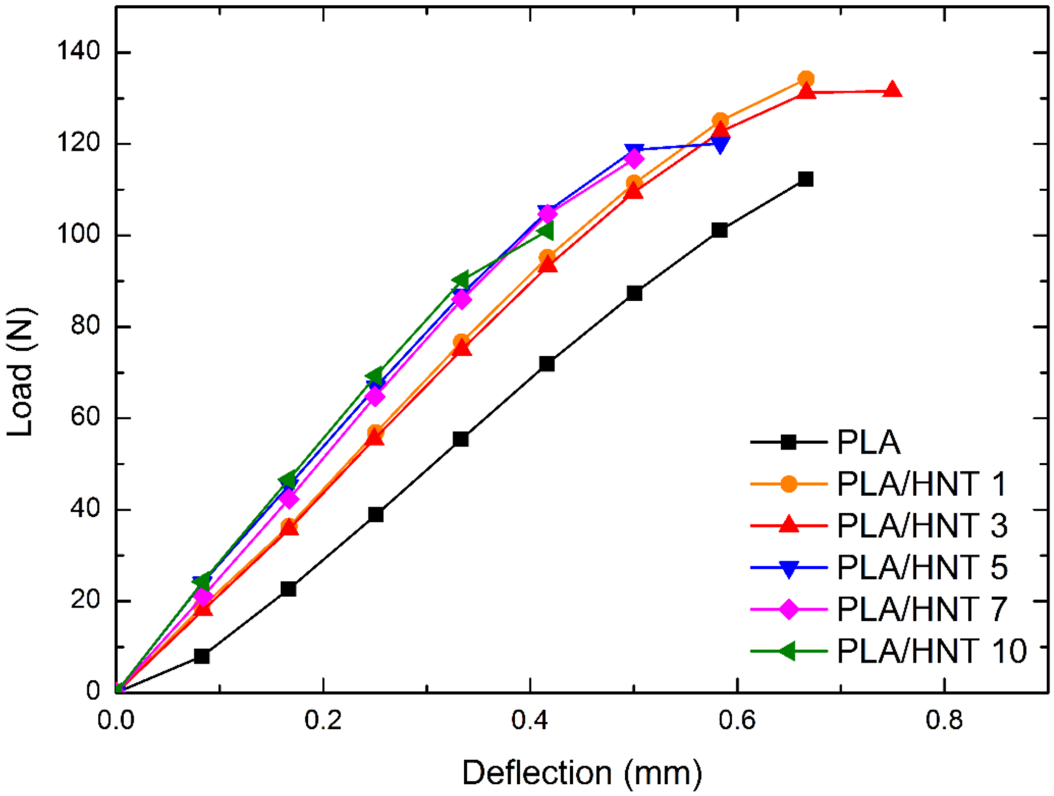

Figure 3.4 Load-deflection curves of the single-edge-notched-bending specimens obtained during fracture toughness tests

Table3.5. Fracture Toughness (K_{IC} and G_{IC}) values of the specimens

Specimens	**K_{IC} (MPa√m)**	**G_{IC} (kJ/m^2)**
PLA	2.93 ± 0.14	3.75 ± 0.02
PLA/HNT 1	3.37 ± 0.02	4.94 ± 0.11
PLA/HNT 3	3.63 ± 0.01	5.79 ± 0.59
PLA/HNT 5	3.22 ± 0.03	4.26 ± 0.10
PLA/HNT 7	3.03 ± 0.07	3.55 ± 0.39
PLA/HNT 10	2.67 ± 0.04	2.42 ± 0.07

These figures and tables reveal that fracture toughness values (K_{IC} and G_{IC}) of very brittle PLA matrix increases especially at low HNT contents due to the effectiveness of the strong and high aspect ratio HNT structure on the toughening mechanisms of “crack deflection”, “debonding” and “pull-out”. Using 3 wt% HNT leads to highest improvements in the fracture toughness values. Compared to neat PLA, the increases in K_{IC} is 24%, while in G_{IC} it is 54%. On the other hand, just like in the strength values, addition of higher HNT content beyond 5 wt% leads to decreases in the values, again due to the higher possibility of agglomeration of nanoreinforcements.

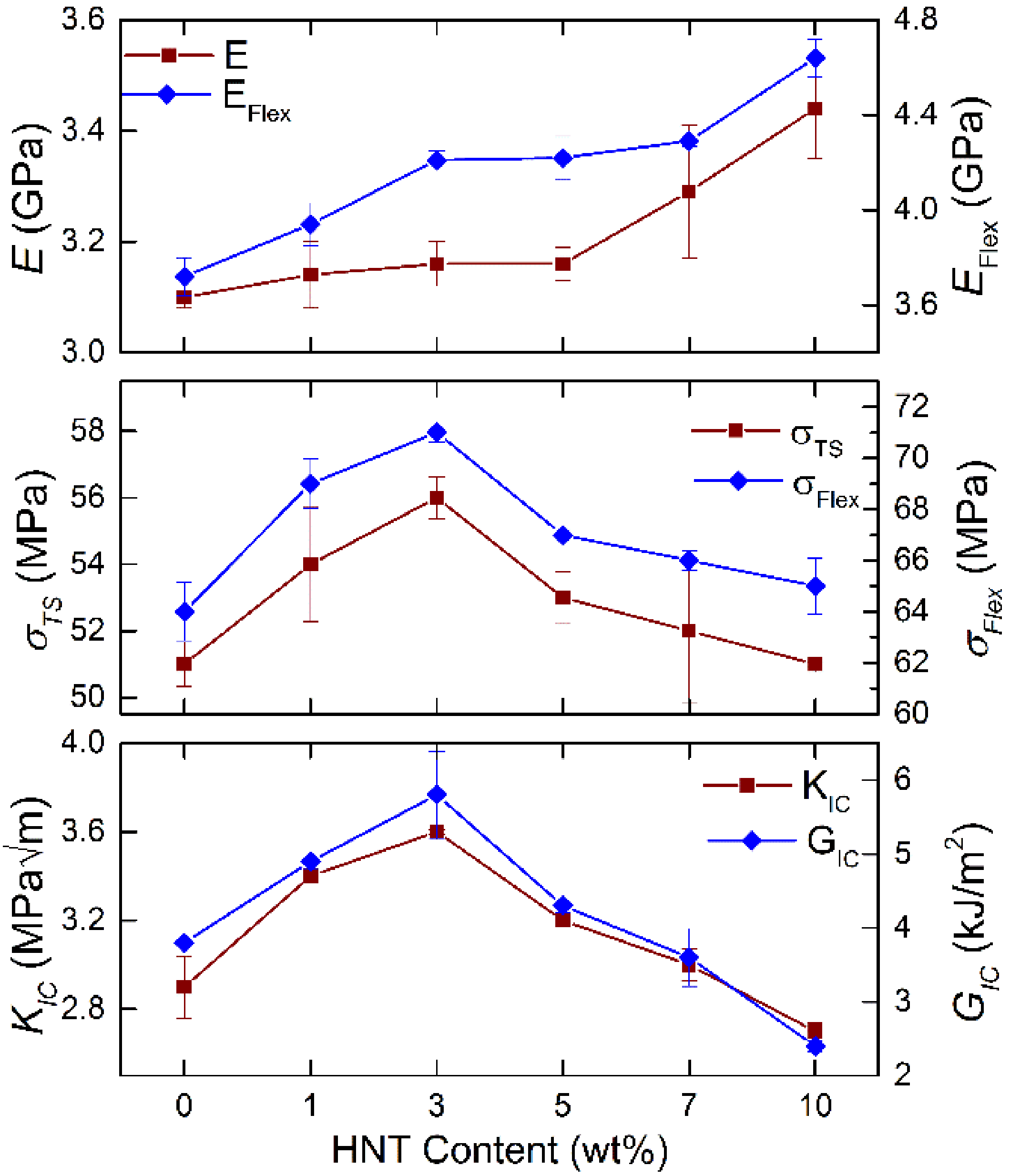

Figure 3.5 Effects of HNT content on the mechanical properties of the specimens

3.1.4 Thermal Behavior of the Specimens

Thermal behaviors of the specimens were first investigated by conducting DSC analyses. Figure 3.6 shows heating thermograms of the specimens obtained after erasing their thermal history. Then, important transition temperatures, i.e. “glass transition, crystallization, melting temperature” (T_g , T_c , T_w), together with “enthalpies of melting and crystallization” (ΔH_m and ΔH_c) were determined and tabulated in Table 3.6. This table also includes “percent crystallinity” (X_C) of the specimens obtained using the following relation:

$$X_C = \frac{\Delta H_m - \Delta H_c}{w_{PLA} \Delta H_m^{\circ}} \times 100 \tag{1}$$

where w_{PLA} is the weight fraction of the PLA matrix, while ΔH_m° is the melting enthalpy of 100% crystalline PLA given as 93.1 J/g in the literature [71]. Effects of HNT content on T_c and X_C were also represented in Figure 3.9.

Table 3.6 indicates that incorporation of HNT has almost no influence on the T_g and T_m values of the PLA matrix, however there are substantial decreases in the T_c of PLA. This should be due to the HNT reinforcements acting as effective heterogeneous nucleation agents leading to the start of crystallization at rather lower temperatures during heating profile. Therefore, percent crystallinity (X_C) of all PLA/HNT nanocomposites are much higher compared to neat PLA matrix. Table 3.6 shows that 15% crystallinity of PLA increases to 30% when only 3 wt% HNTs were added, i.e. an increase of two times.

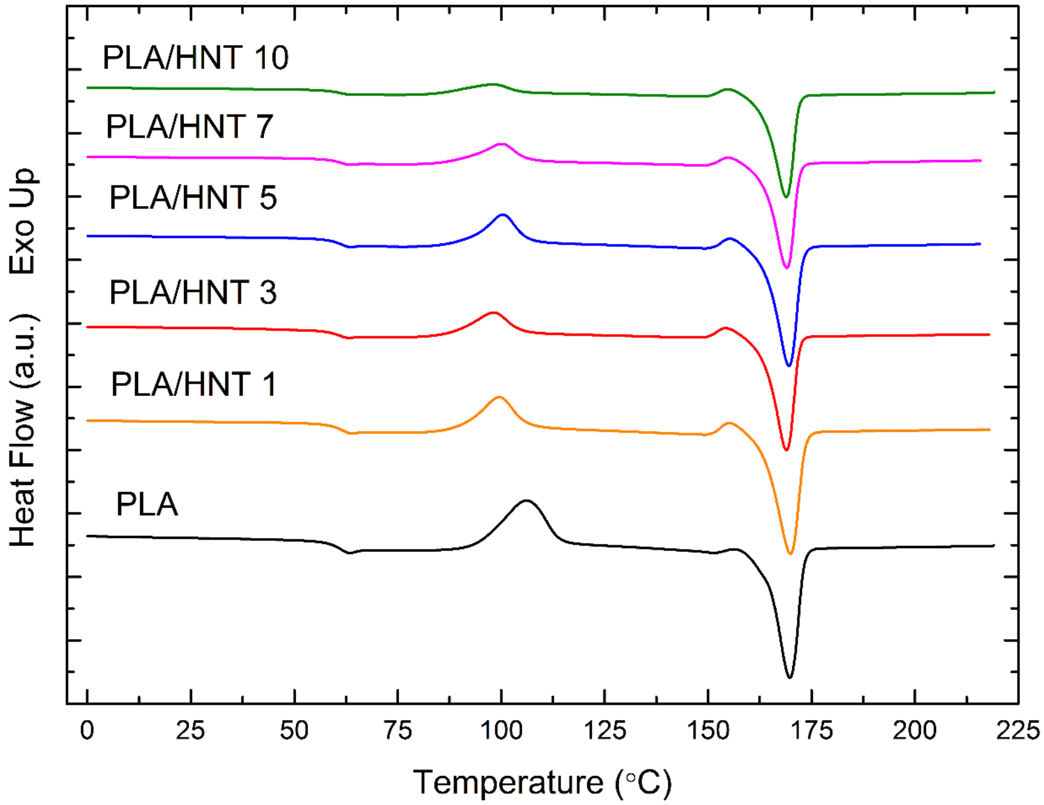

Figure 3.6 DSC heating thermograms of the specimens obtained after erasing their thermal history

Table 3.6. Transition temperatures (T_g, T_c, T_m), enthalpies (ΔH_m, ΔH_c) and crystallinity percent (X_C) of the specimens during heating profile

Specimens	T_g (°C)	T_c (°C)	T_m (°C)	ΔH_m (J/g)	ΔH_c (J/g)	X_C (%)
PLA	60.1	106.2	169.8	41.0	27.3	14.7
PLA/HNT 1	60.4	99.5	169.9	40.6	17.2	25.4
PLA/HNT 3	60.3	98.2	169.0	41.7	14.8	29.8
PLA/HNT 5	60.5	100.4	169.6	39.3	14.8	27.7
PLA/HNT 7	60.8	100.1	169.1	36.5	12.4	27.8
PLA/HNT 10	60.2	98.1	168.9	36.1	11.0	27.2

The second analysis to investigate thermal behavior of the specimens was TGA, where data were evaluated in the form of thermogravimetric (TG) and differential thermogravimetric (DTG) curves, as given in Figure 3.7. These curves show that all specimens mainly degrade at only one step. Certain levels of thermal degradation temperatures determined from these curves are tabulated in Table 3.7. In this table, $T_{5\%}$, $T_{10\%}$, $T_{25\%}$ represent thermal degradation temperatures of the specimens at 5, 10, 25 wt% mass loss in TG curves, while T_{max} represents maximum mass loss rate peak temperature of the specimens in DTG curves. Effects of HNT content on $T_{5\%}$ and T_{max} was also included in Figure 3.9.

Table 3.7. Thermal degradation temperatures ($T_{5\%}$, $T_{10\%}$,$T_{25\%}$) of the specimens at 5, 10, 25 wt% mass losses and maxmimum mass loss rate peak (T_{max})

Specimens	**$T_{5\%}$ (°C)**	**$T_{10\%}$ (°C)**	**$T_{25\%}$ (°C)**	**T_{max} (°C)**
PLA	327	337	350	366
PLA/HNT 1	322	333	347	363
PLA/HNT 3	314	325	340	359
PLA/HNT 5	309	319	335	354
PLA/HNT 7	306	316	331	353
PLA/HNT 10	301	311	326	346

These figures and tables reveal that all thermal degradation temperatures ($T_{5\%}$, $T_{10\%}$, $T_{25\%}$, T_{max}) of PLA decrease gradually with the loading of HNTs. Decreases in the thermal degradation temperatures are around 10°C when 3 wt% HNTs were added, while decreases are as much as 20°C with 10 wt% HNT addition.

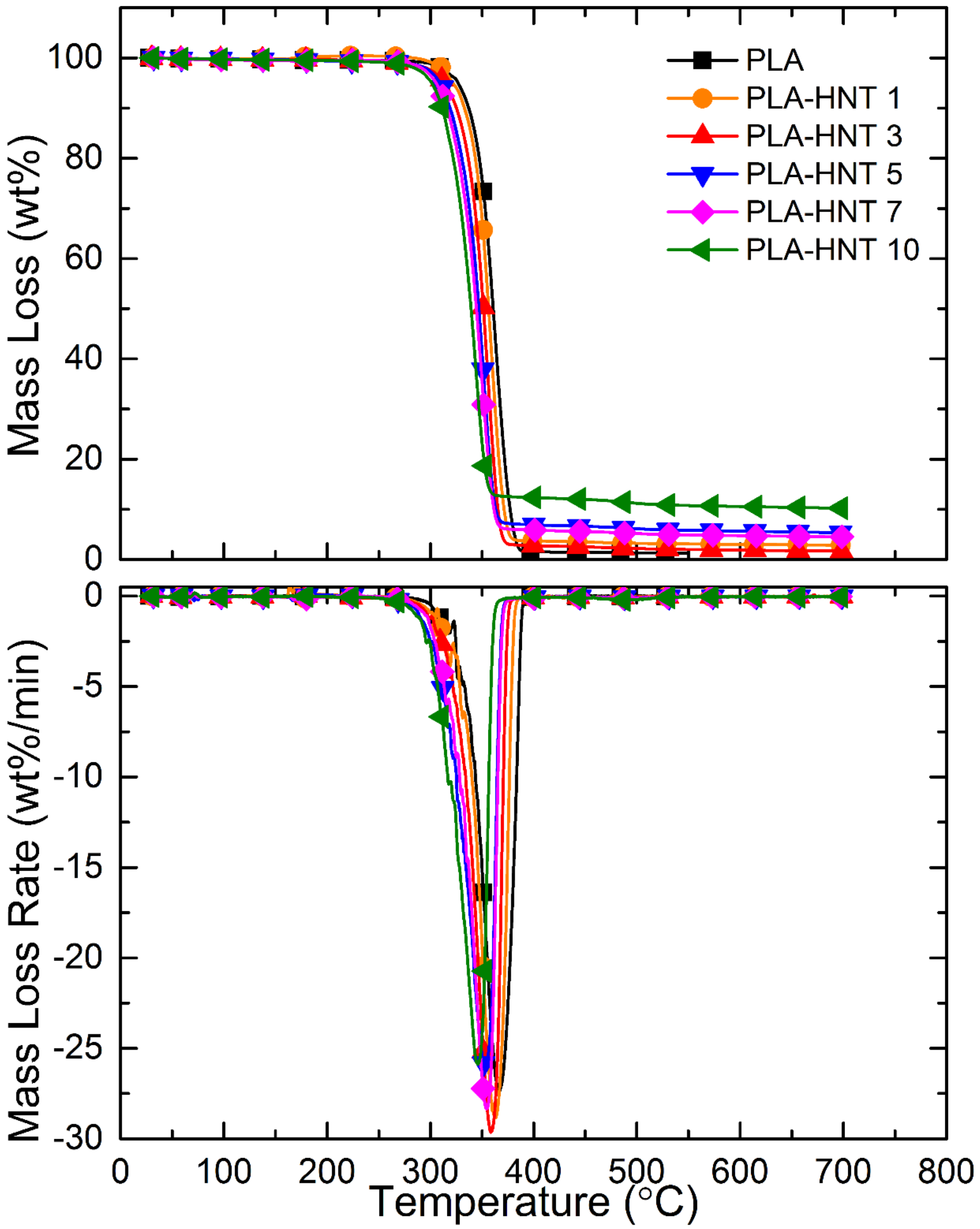

Figure 3.7 Thermogravimetric (TG) and differential thermogravimetric (DTG) curves of the specimens

These detrimental effects of HNTs on the thermal degradation of PLA could be due to the bound water molecules present in between the rolled walls of HNTs' tubular structure. Vacuum oven drying operations at 60°C applied prior to both compounding and shaping in this study might be not enough to release these bound water molecules. However, higher temperatures applied during TGA could release these bound water molecules leading to increased level of thermal degradation combined with hydrolytic degradation of PLA macromolecules. Similar discussions were also made by Murariu et al. [52]

The third analysis DMA was used to study thermomechanical behavior of the specimens. Storage modulus versus temperature curves obtained are given in Figure 3.8. Then, two levels of "Storage Modulus" (E') at 25° and 50°C were determined and tabulated in Table 3.8. Effects of HNT loading on these values are also given in Figure 3.9.

Table 3.8. Storage Modulus (E') values of the specimens at 25° and 50°C

Specimens	**E' at 25°C (GPa)**	**E' at 50°C (GPa)**
PLA	2.78	2.72
PLA/HNT 1	2.97	2.96
PLA/HNT 3	3.16	3.09
PLA/HNT 5	3.47	3.35
PLA/HNT 7	3.78	3.63
PLA/HNT 10	3.89	3.84

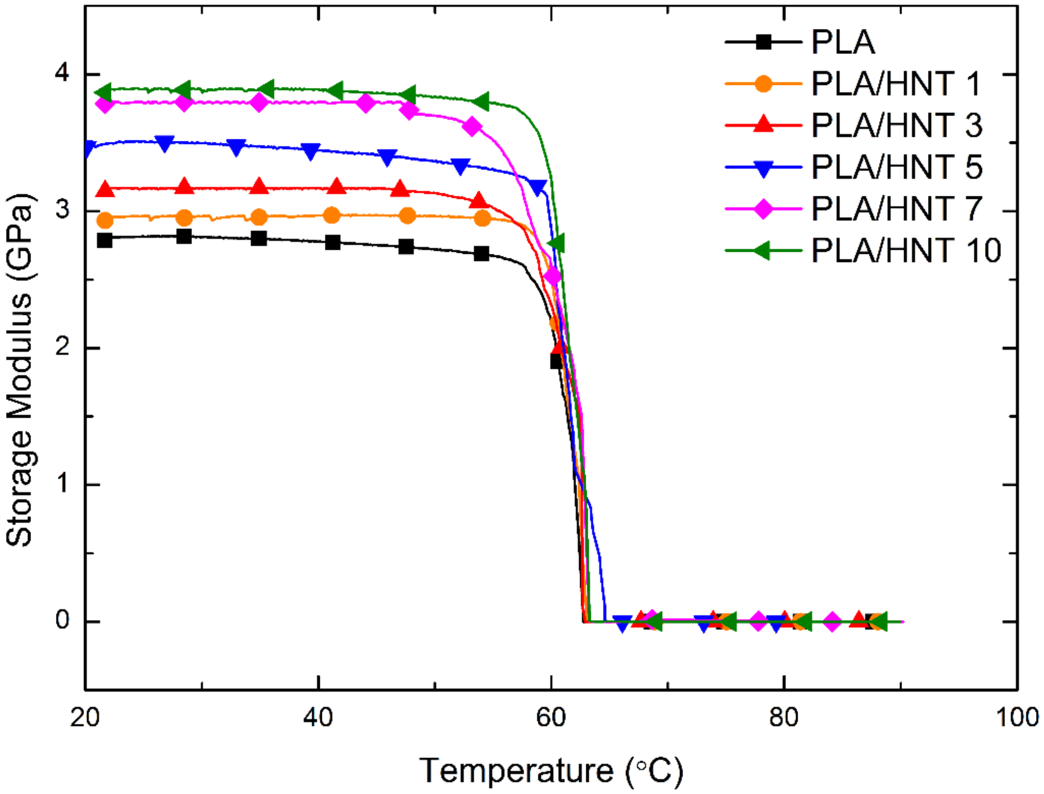

Figure 3.8 Storage modulus curves of the specimens obtained by DMA

Figure 3.8 shows that storage modulus of all specimens vanishes at 60°C which is the T_g of PLA where blocks of polymer chain segments move over each other easily and quickly. However below 50°C, the glassy plateau regions exist where addition of HNTs increases E' values of PLA due to the decreased mobility of the side groups of PLA backbone structure and the strengthening effects of rigid HNTs. Just like it was discussed for the values of E and E_{Flex} in the previous section, Figure 3.9 also indicates that increasing HNT content increases values of E' at 25° and 50°C almost linearly. Compared to neat PLA, increases in E′ values can be as much as 39% when 10 wt% HNT was used.

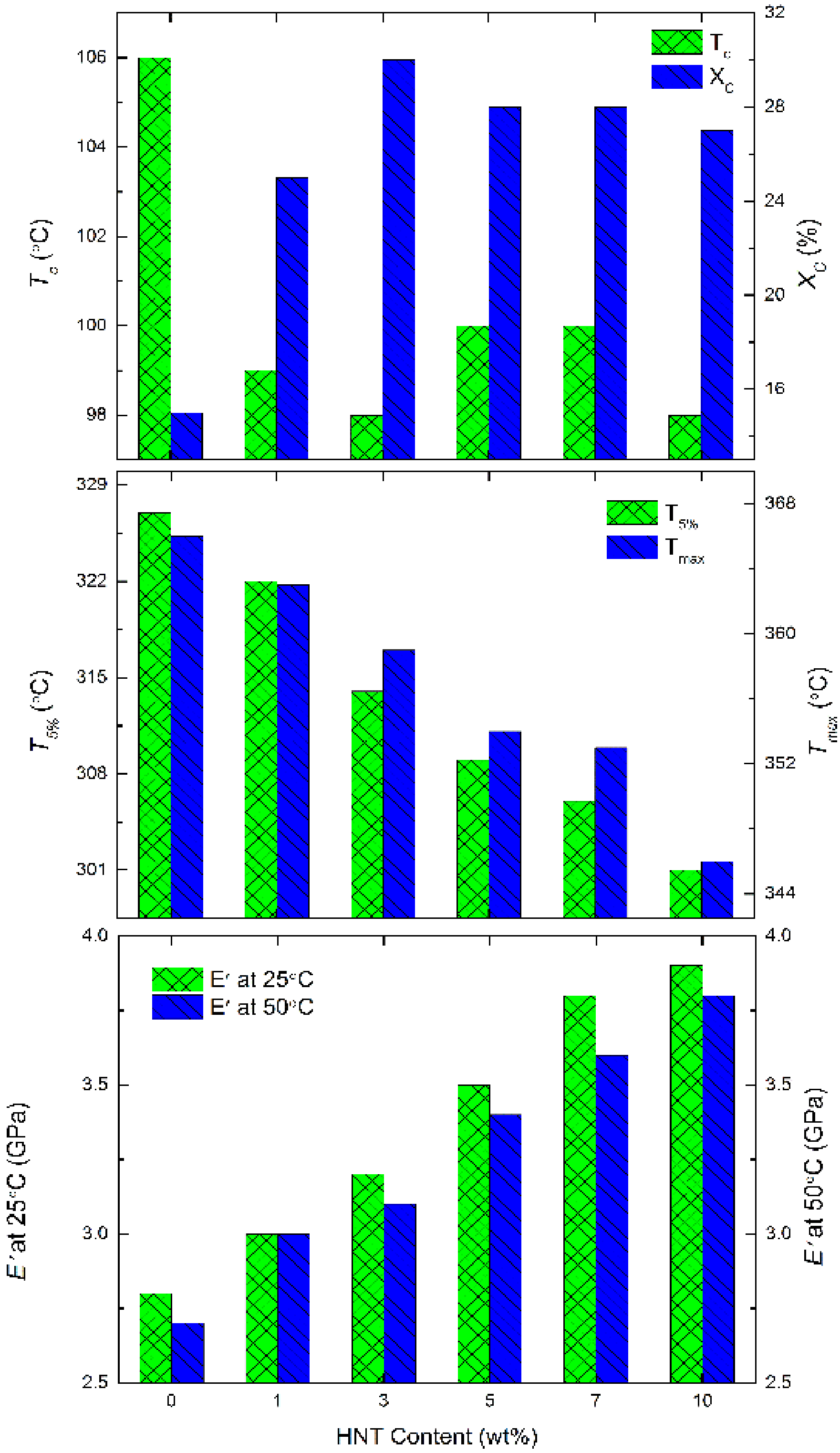

Figure 3.9 Effects of HNT content on the certain thermal properties of the specimens

3.2 Crystallization Kinetics of PLA/HNT Nanocomposites

3.2.1 Isothermal Melt Crystallization Kinetics of the Specimens

In order to reveal the effects of HNT and its loading on the isothermal crystallization kinetics of PLA, DSC procedures explained in the experimental part were applied for all specimens. Figure 3.10 shows isothermal melt crystallization thermograms of the specimens at 100°C.

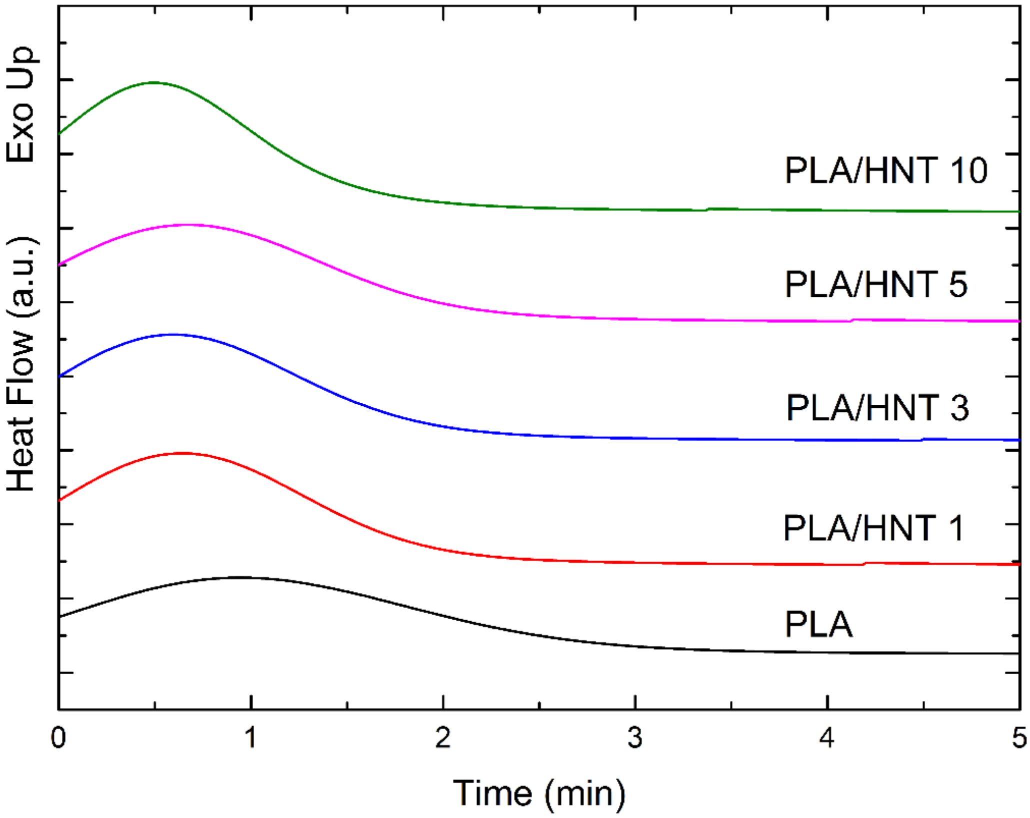

Figure 3.10 DSC isothermal melt crystallization thermograms of the specimens at 100°C

The degree of isothermal crystallinity (X_{ic}) of PLA and PLA/HNT nanocomposites were determined by using the following equation:

$$X_{iC}(\%) = \frac{\Delta H_{ic}}{w_{PLA}\Delta H_m^0}100 \tag{2}$$

where ΔH_{ic} is the measured heat of isothermal melt crystallization of the specimens, ΔH_m^0 is the heat of fusion of 100 % crystalline PLA, and w_{PLA} is the weight fraction of the PLA matrix. In the literature [71] the heat of fusion for the formation of α crystal phase is determined as 93.1 J/g.

The degree of crystallinity together with other isothermal crystallization parameters for PLA and PLA/HNT nanocomposites are given in Table 3.9. It can be stated that just like other micro- and nano-fillers, HNTs could also act as heterogeneous nucleation agents. Thus, Table 3.9 shows that the degree of isothermal crystallinity X_{ic} of PLA increased with the incorporation of HNTs. For instance, using only 3 wt% HNT increased crystallinity of PLA from 24% to 37%, i.e. an increase of 40%.

Table 3.9. Isothermal melt crystallization parameters and Avrami constants of the specimens

Specimens	**ΔH_{ic} (J/g)**	**X_{ic} (%)**	**t_{max} (min)**	**$t_{1/2}$ (min)**	**n**	**K**
PLA	22.01	23.63	0.95	1.53	2.13	0.49
PLA/HNT 1	31.07	33.71	0.65	0.97	2.16	1.12
PLA/HNT 3	33.02	36.56	0.59	0.93	2.16	1.19
PLA/HNT 5	32.00	36.18	0.58	0.92	2.17	1.21
PLA/HNT 10	30.04	35.85	0.49	0.79	2.16	1.79

Exothermic peaks of the isothermal crystallization curves in Figure 3.10 represent t_{max}, which is the time to reach the maximum rate of crystallization. Table 3.9 indicates that t_{max} decreased with increasing HNT content. For example, t_{max} of neat PLA decreased from 0.95 min down to 0.49 min, a decrease of almost two times, with 10 wt% HNT content.

Figure 3.11 indicates fractional crystallinity X_t as a function of isothermal melt crystallization time for PLA and PLA/HNT nanocomposites. X_t can be determined as a function of time by using the following equation:

$$X_t = \frac{\int_0^{t} \frac{dH(t)}{dt} dt}{\int_0^{t\infty} \frac{dH(t)}{dt} dt} \tag{3}$$

where $dH(t)/dt$ is the rate of heat evolution and t_∞ is the end time of the crystallization. In this equation, integral at the numerator indicates generated crystallization enthalpy up to time t, while integral at the denominator shows total crystallization enthalpy at time t_∞.

It is seen in Figure 3.11 that isothermal crystallization curves of PLA and PLA/HNT nanocomposites have characteristic sigmoidal isotherms. In order to characterize rate of isothermal crystallization process, the time at which half crystallization occurs, i.e. $t_{1/2}$ can be used. The larger the $t_{1/2}$ value the slower the crystallization rate. Thus, $t_{1/2}$ values were determined from the onset of crystallization to the point where the crystallization is half completed. Then, all $t_{1/2}$ data obtained were tabulated in Table 3.9.

It can be seen in Table 3.9 that t1/2 of PLA is much larger compared to its nanocomposites which indicates a much slower crystallization rate. Again, just like *t*$_{max}$, *t*$_{1/2}$ decreased with increasing HNT content, e.g. from 1.53 min to 0.79 min with 10 wt% HNTs, again a decrease to half.

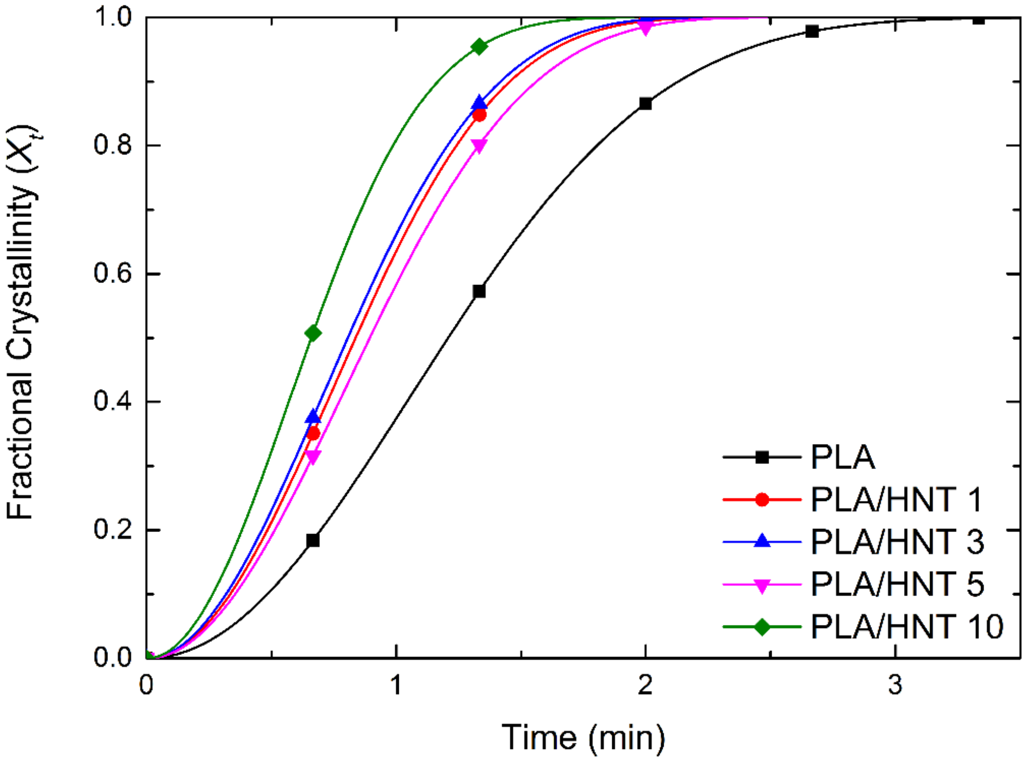

Figure 3.11 Fractional crystallinity versus isothermal melt crystallization time curves of the specimens

Then, isothermal melt crystallization kinetics of the specimens was evaluated by using the well-established Avrami equation:

$$1 - X_t = \exp(-Kt^n) \tag{4}$$

In this equation, X_t is the fractional crystallization at different crystallization times t, whereas K is the crystallization rate constant and n is the Avrami exponent. It is well known that Avrami constants are related to the rate and different mechanisms of nucleation and growth of crystalline phases.

Avrami equation can be rearranged by taking the double logarithm of both sides:

$$\ln[-\ln(1 - X_t)] = n\ \ln t + \ln K \qquad (5)$$

This equation is especially used to describe the initial stage of crystallization, i.e. ‘‘primary crystallization’’, because of almost having no deviation from linearity in this stage. On the other hand, Avrami equation may not obey to describe the late stages of crystallization, i.e. ‘‘secondary crystallization’’ due to the deviation from the linearity.

Figure 3.12 shows Avrami plots of ln[-ln(1-X_t)] versus ln t for PLA and PLA/HNT nanocomposites. Generally, Avrami constants n and K can be determined by fitting isothermal crystallization data at X_t<0.5. Because, up to 50 % relative crystallinity degree, Avrami plots obey linearity. Similarly in this study, since primary crystallization stage comprised even above 50 % relative crystallinity, values of n and K were determined as the slopes and intercepts of the linear part of each curve by using the linear regression analysis. Then, these Avrami constants were tabulated in Table 3.9.

Table 3.9 shows that Avrami exponent n for neat PLA and its nanocomposites is between 2.13 and 2.17 which could be attributed to the two dimensional crystal growth, i.e. the nucleus could not grow in a three dimensional manner as spherulites impinge against each other. The exponent n having values less than 3 was also observed in certain PLA crystallization studies in the literature [72-74].

Table 3.9 also shows that Avrami rate constant K for neat PLA is 0.49, however it increased with increasing HNT content, e.g. up to a value of 1.79 at 10 wt% HNT loading. This means that isothermal crystallization rate constant *K* could be increased more than three times, which is again due to the heterogeneous nucleation on the surfaces of HNTs.

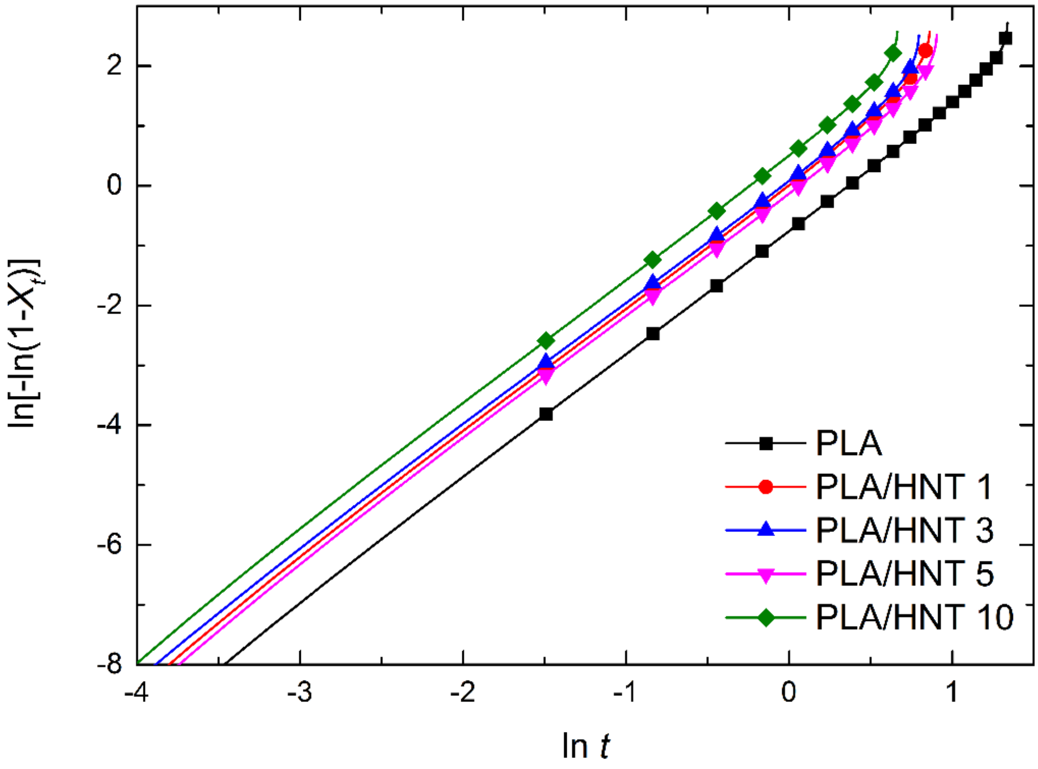

Figure 3.12 Avrami plots of ln[-ln(1-X_t)] versus ln *t* of the specimens during isothermal melt crystallization

3.2.2 Non-isothermal Melt Crystallization Kinetics of the Specimens

Secondly, to investigate influences of HNTs on the non-isothermal melt crystallization kinetics of PLA, DSC procedures explained in the experimental part were applied for the specimens. Figure 3.13 gives DSC non-isothermal crystallization thermograms of PLA and PLA/HNT nanocomposites at a cooling rate of 10°C/min. From these curves, apart from the heat of non-isothermal crystallization (ΔH_{nic}), onset temperature of crystallization (T_0), peak temperature of crystallization (T_p), and temperature range of crystallization (T_R) can be also determined.

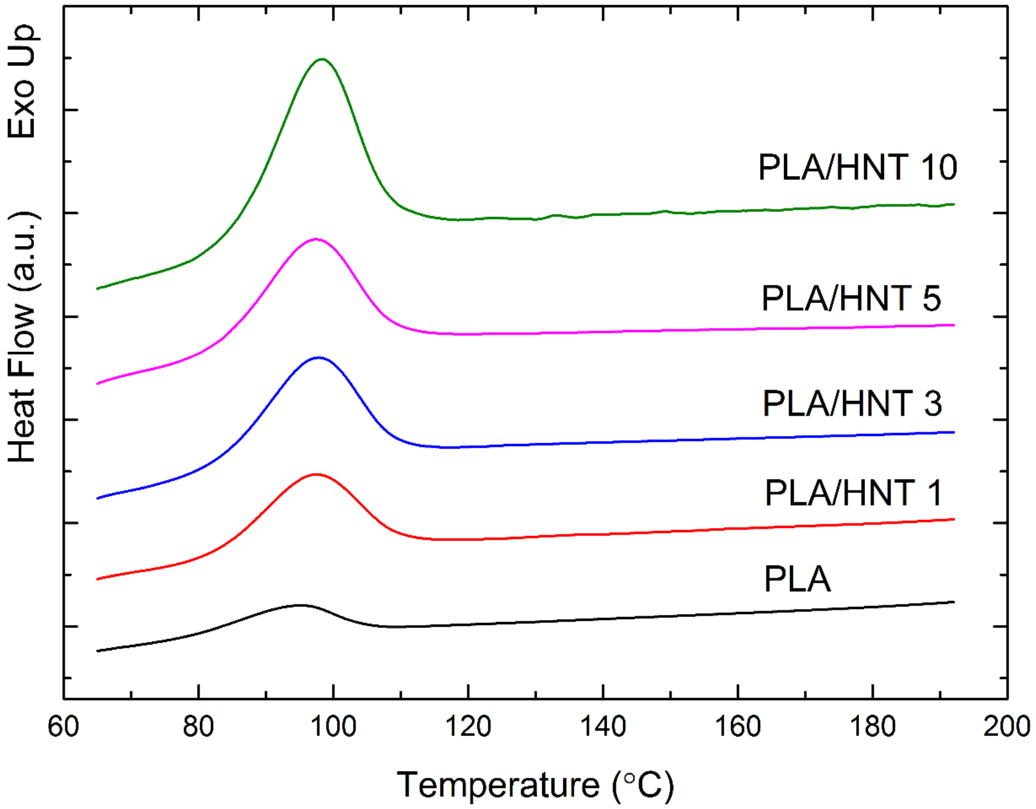

Figure 3.13 DSC cooling thermograms during non-isothermal melt crystallization of the specimens at 10°C/min

After determining ΔH_{nic} of each specimen by integrating the area under the non-isothermal crystallization peaks, the degree of non-isothermal crystallinity (X_{nic}) of PLA and its nanocomposites were compared by using the following equation:

$$X_{nic}(\%) = \frac{\Delta H_{nic}}{w_{PLA}\Delta H_m^0} 100 \tag{6}$$

where ΔH_{nic} is the measured heat of non-isothermal crystallization of the specimens, while ΔH_m^0 and w_{PLA} are the same as discussed in the previous section.

Then, the degree of non-isothermal crystallinity (X_{nic}) together with other non-isothermal crystallization parameters (T_0, T_p, T_R) for PLA and its nanocomposites are tabulated in Table 3.10. Just like in the previous isothermal case, Table 3.10 shows that incorporation of HNTs increased the degree of crystallinity of PLA also during non-isothermal cooling. This time, the increases were enormous. For instance, the crystallinity of PLA which was only 2.84% increased to 29.81% with the addition of only 3 wt% HNT, i.e. an increase of more than 10 times. Because of their nano-size and high aspect ratio, HNTs had very good ability to reduce nucleation activation energy which made them very efficient heterogeneous nucleation agents.

Table 3.10. Non-Isothermal melt crystallization parameters and Avrami constants of the specimens

Specimens	ΔH_c **(J/g)**	X_C **(%)**	T_0 **(°C)**	T_p **(°C)**	T_R **(°C)**	$T_{1/2}$ **(°C)**	$t_{1/2}$ **(min)**	n	K	K_c
PLA	2.64	2.84	114	95.00	44	93.52	2.14	2.85	0.019	0.68
PLA/HNT 1	20.38	22.11	120	97.67	48	96.64	2.28	3.53	0.018	0.67
PLA/HNT 3	26.92	29.81	122	97.75	52	97.75	2.69	3.54	0.015	0.66
PLA/HNT 5	23.88	26.99	123	97.41	51	96.58	2.57	3.76	0.015	0.65
PLA/HNT 10	23.90	28.52	120	98.26	50	97.50	2.26	3.86	0.018	0.66

Table 3.10 also shows that HNTs increased the onset (T_0) and the peak (T_p) temperatures of non-isothermal crystallization to higher temperatures. Similarly, temperature ranges (T_R) of the exothermic peaks of all nanocomposites are broader compared to neat PLA. This means that incorporation of HNTs leads to start of crystallization of PLA chains at higher temperatures and continuation of crystallization in broader ranges.

For the non-isothermal crystallization case, fractional crystallinity X_T can be determined as a function of temperature by using the following equation:

$$X_T = \frac{\int_{T_0}^{T} \frac{dH(T)}{dT} dT}{\int_{T_0}^{T\infty} \frac{dH(T)}{dT} dT} \tag{7}$$

where T_0 and T_∞ are the onset and end crystallization temperatures, respectively. In this equation, integral at the numerator indicates generated crystallization enthalpy up to crystallization temperature T, while integral at the denominator shows total crystallization enthalpy at temperature T_∞. Figure 3.14 shows sigmoidal curves of amorphous fraction ($1 - X_T$) versus non-isothermal crystallization temperature T for PLA and its nanocomposites.

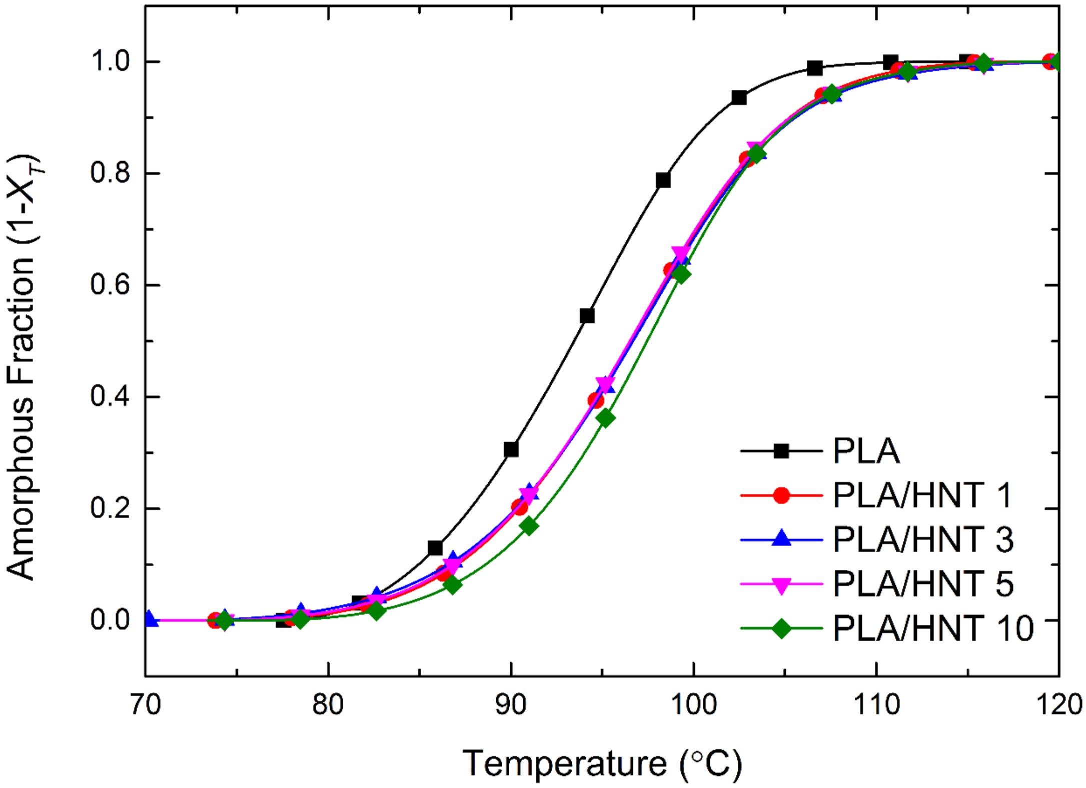

Figure 3.14 Amorphous fraction versus non-isothermal crystallization temperature curves of the specimens

From these curves it was also possible to determine $T_{1/2}$ values, i.e. the temperature at which half crystallization occurs. Similar to the values of T_0, T_p, T_R determined from non-isothermal cooling thermograms, values of $T_{1/2}$ given in Table 3.10 indicate that crystallization for the nanocomposites takes place at higher temperatures than neat PLA. For example, $T_{1/2}$ of neat PLA (93°C) increased by 4°C reaching to a value of 97°C for the nanocomposite PLA/HNT 3.

Then, in order to obtain sigmoidal crystallization curves with respect to time, the following relation between crystallization temperature T and crystallization time t

$$t = \frac{T_0 - T}{\beta} \tag{8}$$

can be used; where β is the cooling rate during non-isothermal crystallization. Figure 3.15 shows amorphous fraction (1 - X_t) versus non-isothermal crystallization time t curves of the specimens. It is seen that crystallization curves of the nanocomposites shift to longer times compared to neat PLA matrix.

From these curves it is again possible to characterize rate of non-isothermal crystallization by determining the values of $t_{1/2}$, i.e. the time at which half crystallization occurs. Table 3.10 shows that compared to neat PLA, all nanocomposites have much slower crystallization rate. For instance, values of $t_{1/2}$ increased from 1.66 min for neat PLA to 2.78 min for the nanocomposite with 3 wt% HNTs, i.e. an increase of almost two times. It was considered that under non-isothermal conditions HNTs could act as physical obstacles, thus delaying the necessary conformational mobility of PLA chains to crystallize in a regular manner.

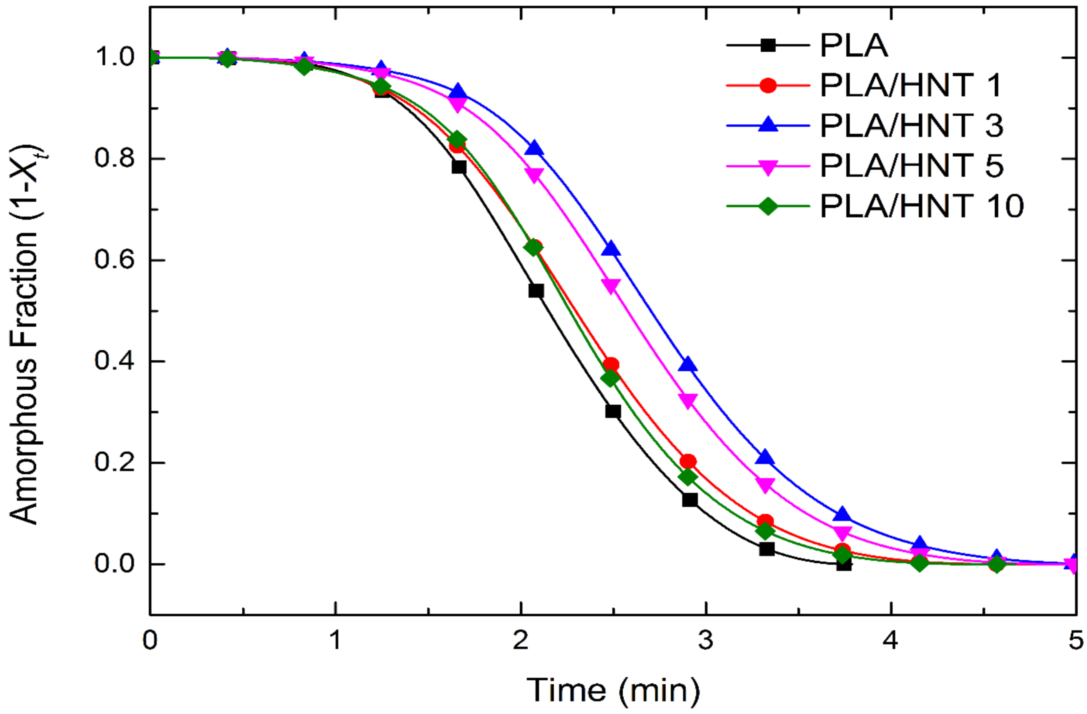

Figure 3.15 Amorphous fraction versus non-isothermal crystallization time curves of the specimens

In order to evaluate Avrami constant of non-isothermal crystallization kinetics, the basic Avrami relation given in Equation 4 above should be modified, because the rate of non-isothermal crystallization depends on the cooling rate. In the literature, one of the most widely used modification of Avrami relation was made by Jeziorny [75]. He suggested that the rate constant K should be corrected by cooling rate β to obtain the modified rate constant K_C, i.e.:

$$\ln K_C = \frac{\ln K}{\beta} \tag{9}$$

Thus, by taking the double logarithm of both sides of basic Avrami equation (Equation 3), and introducing the modification of Jeziorny, the final form of modified Avrami equation becomes:

$$\ln[-\ln(1-X_t)] = n \ln t + \beta \ln K_c \tag{10}$$

By using the above relation, modified Avrami plots of $\ln[-\ln(1-X_t)]$ versus $\ln t$ were constructed for the specimens. Figure 3.16 shows these curves for PLA and its nanocomposites. In this study, just like in the previous case of isothermal crystallization, modified Avrami plots all obeyed linearity beyond 50 % relative crystallinity X_t. Therefore, modified Avrami constants n, K and K_c were determined in the linear range of the curves, and tabulated in Table 3.10.

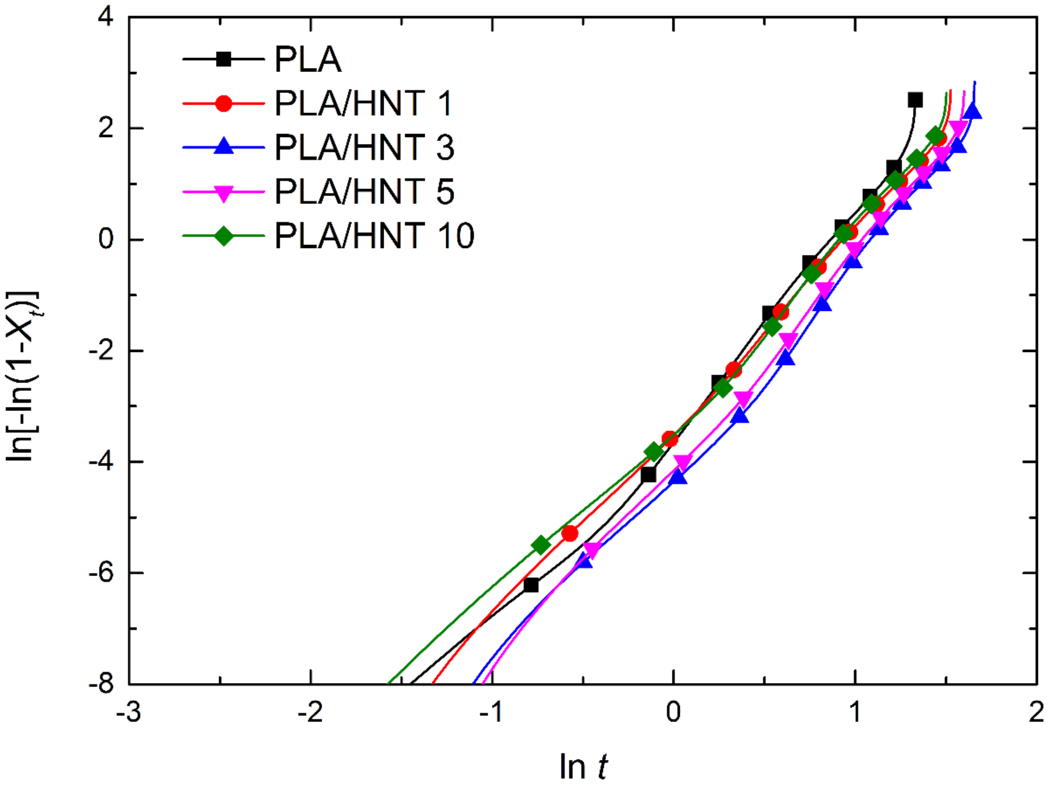

Figure 3.16 Modified Avrami equation plots of ln[-ln(1-X_t)] versus ln *t* during non-isothermal crystallization of the specimens

Table 3.10 shows that the value of modified Avrami exponent *n* for neat PLA is 2.85, while it increased above 3.8 when HNTs were incorporated. This means that two-dimensional growth mechanism of spherulites in PLA transformed into three-dimensional growth in PLA/HNT nanocomposites. On the other hand, compared to neat PLA, values of modified Avrami rate constants *K* and K_C decreased slightly for the nanocomposites. As discussed for the values of $t_{1/2}$ above, the decreases in the rate constants could be due to the physical barrier effects of HNTs delaying the conformational arrangements of PLA chains for crystallization. Similar results were reported [76], especially at high HNT loadings in the polypropylene (PP) matrix.

3.2.3 Crystallinity of the Injection Molded and then Annealed Specimens

Injection molding is one of the most common methods to shape thermoplastic components in the industry. During this process, molten polymer is injected into a mold or cavity under high pressure. The temperature of mold which is well below the melting point influences the crystalline structure, and consequently mechanical and physical properties of the component.

However, unlike the other conventional polymers used in the industry, the cooling rate during injection molding is too fast for the PLA molecular chains to crystallize, thus leading to the formation of amorphous structure. One of the solutions for the polymers requiring rather slow cooling rate for crystallization is to heat them right after their injection molding process. This heating operation at around crystallization temperature for sufficient time is named as “annealing”.

Therefore, in order to investigate crystallinity of the injection molded bar specimens, they were annealed in an oven at 100°C for 20 min. These annealing parameters were determined as the optimum values after many trials. Crystallinities of these specimens were characterized using two techniques; DSC and XRD as defined in the experimental part.

Figure 3.17 shows DSC first heating thermograms of the injection molded and then annealed specimens. Then, important transition temperatures, i.e. “glass transition, cold crystallization, melting” (T_g, T_{cc}, T_m), together with “enthalpies of melting and cold crystallization” (ΔH_m and ΔH_{cc}) were determined and tabulated in Table 3.11. This table also includes “percent crystallinity of the annealed specimens” ($X_{ac\text{-}DSC}$) obtained using the following equation:

$$X_{ac-DSC}(\%) = \frac{\Delta H_m - \Delta H_{cc}}{w_{PLA} \Delta H_m^0} 100 \qquad (11)$$

where ΔH_m and ΔH_{cc} are the measured heat of melting and cold crystallization of the specimens, respectively; while ΔH_m^0 and w_{PLA} are the same as discussed in the previous sections.

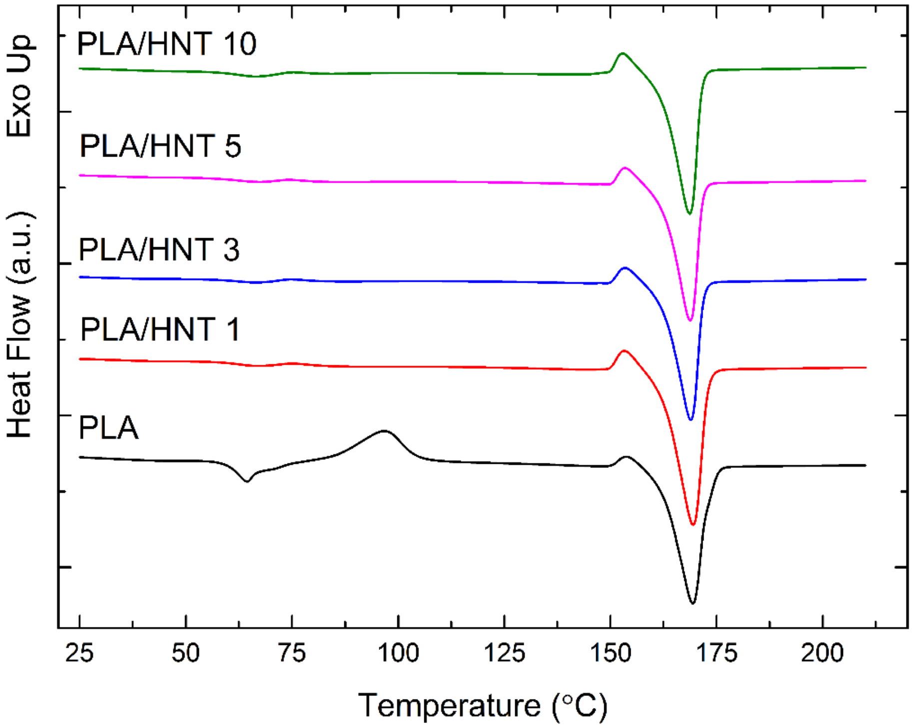

Figure 3.17 DSC first heating thermograms of the injection molded and then annealed specimens

Table 3.11 indicates that incorporation of HNT had almost no influence on the T_g and T_m values of the PLA matrix, however cold crystallization temperature T_{cc} of nanocomposites are 20°C lower compared to neat PLA. This should be due to the HNT reinforcements acting as effective heterogeneous nucleation agents leading to the start of cold crystallization at rather lower temperatures during the first heating profile. On the other hand, Table 3.11 also indicates that cold crystallization enthalpies ΔH_{cc} of the nanocomposites were negligible. This means that compared to neat PLA, PLA/HNT nanocomposites attained their full crystallinity degree during annealing operation. Therefore, Table 3.11 shows that the amount of crystallinity of the annealed specimens determined by DSC, X_{ac}-*DSC* , increased from 31% for neat PLA to 47% for PLA/HNT 1, i.e. a further increase of 50%.

Table 3.11. Crystallinity and other parameters of the injection molded and then annealed specimens, determined by DSC and XRD

Specimens	T_g (°C)	T_{cc} (°C)	T_m (°C)	ΔH_m (J/g)	ΔH_{cc} (J/g)	$X_{ac\text{-}DSC}$ (%)	$X_{ac\text{-}XRD}$ (%)
PLA	60.9	96.7	169.4	47.01	18.65	30.77	21.84
PLA/HNT 1	59.9	75.1	169.5	44.13	0.80	47.01	47.00
PLA/HNT 3	61.2	74.9	168.9	43.03	0.79	46.77	46.02
PLA/HNT 5	59.8	74.3	168.6	39.06	0.62	43.46	36.31
PLA/HNT 10	60.4	75.4	168.7	32.00	0.72	37.33	29.69

After DSC, XRD analyses were also carried out to determine the crystallinity of the injection molded and then annealed specimens by comparing their XRD peaks, as shown in Figure 3.18. As discussed in the introduction part, under normal conditions, PLA crystallizes as orthorhombic α-phase. In the literature [12, 13] the 2θ locations for the α-phase are established. α-phase crystallizes at two diffraction peaks of 16.3° and 18.7° assigned to (200)/(110) and (203) planes, respectively.

In order to determine crystallinity amount of the injection molded and then annealed specimens, X_{ac}-*XRD* , deconvolution of the total curves in terms of amorphous phase and α-crystalline phase was necessary. During deconvolution, the peak locations of α-phase were held constant, while the peak heights and widths were allowed to vary. For the amorphous phase, the broad peak location was allowed to float around 15.5°. In order to start curve fitting algorithm reasonably, heights and breadths of each peak were adjusted manually, then they were modeled using a Gaussian–Lorentzian peak shape. Figure 3.19 shows two examples of deconvoluted XRD peaks for neat PLA and its nanocomposite with 1 wt% HNT. For clarity, curves were shifted.

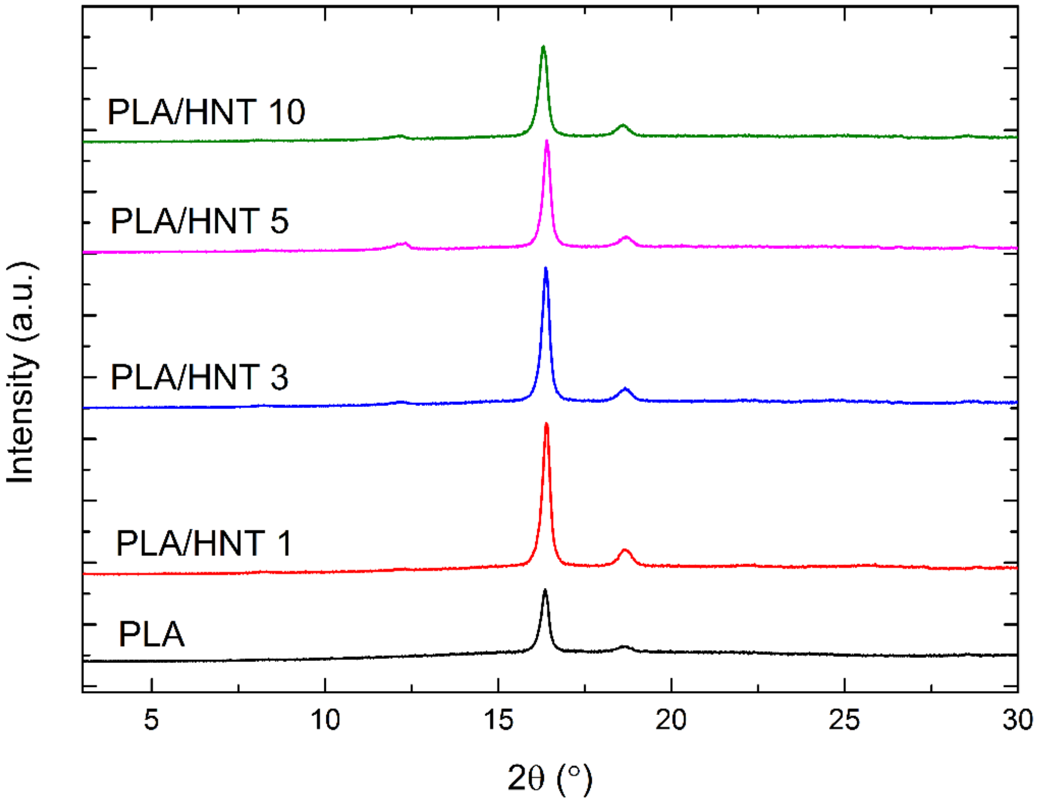

Figure 3.18 XRD patterns of the injection molded and then annealed specimens

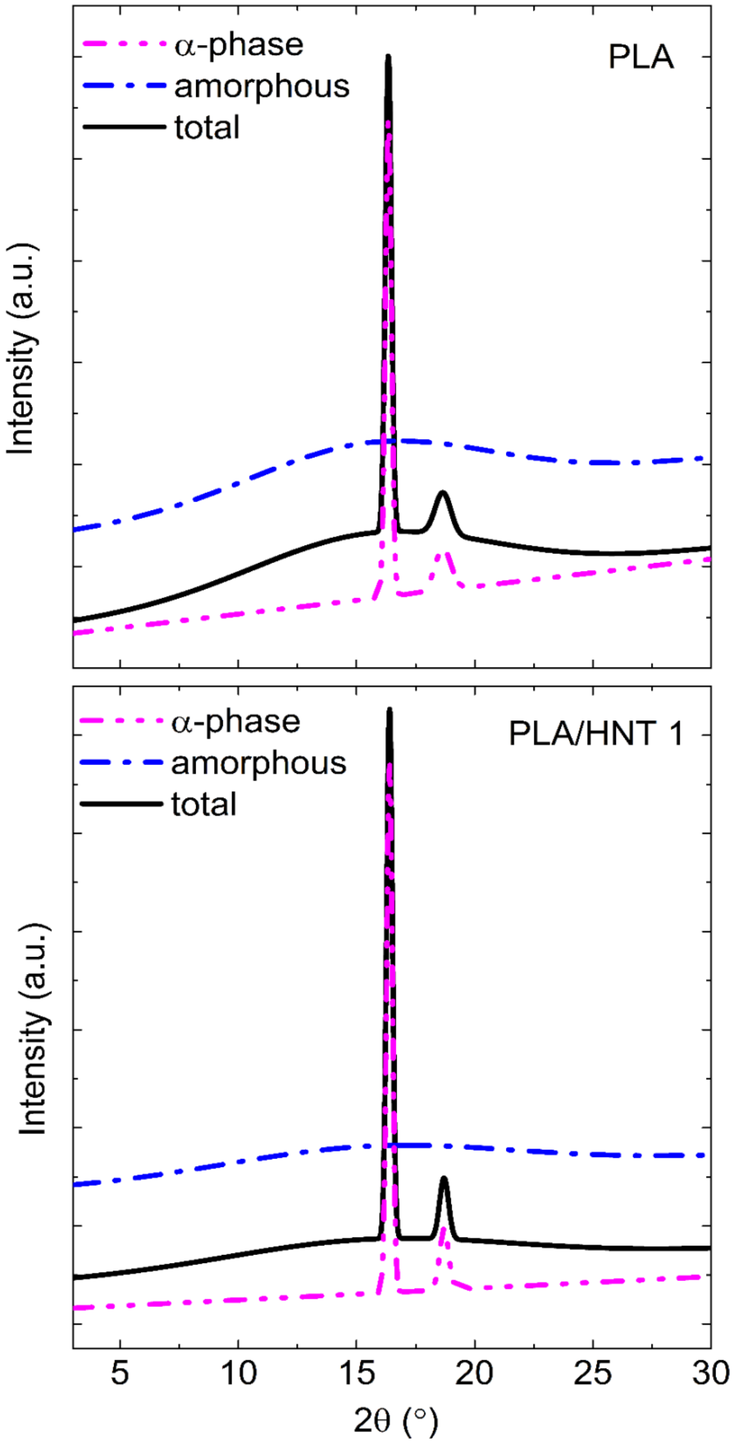

Figure 3.19 Two examples of deconvoluted XRD peaks of the injection molded and then annealed specimens

In order to estimate the degree of crystallinity of each annealed specimen, the ratio of the area of the crystalline phase to that of total area of the curve (amorphous + crystalline) was used. Small XRD peaks of the HNT structure observed above 3 wt% HNT content were also taken into consideration for accuracy. The data and the model predictions agreed well with determination coefficients R^2 being above 0.98. Then, estimated $X_{ac\text{-}XRD}$ values are tabulated also in Table 3.11.

In Table 3.11, it is seen that values of $X_{ac\text{-}DSC}$ and $X_{ac\text{-}XRD}$ were very well matched. That is, crystallinity amounts of the annealed specimens determined by DSC and XRD were consistent with each other. Table 3.11 also shows that, just like in the isothermal and non-isothermal crystallization cases discussed above, the degree of crystallinity of injection molded and then annealed PLA increased significantly after incorporation of HNTs basically due to their heterogeneous nucleation site effect. For example, crystallinity of annealed neat PLA increased from 22% to 47% (an increase of more than two times) by only adding 1 wt% HNT.

3.3 Accelerated Weathering of PLA/HNT Nanocomposites

In this part, influences of accelerated weathering on the specimens were investigated by comparing the changes in the color, chemical structure, mechanical properties and thermal behavior of the specimens before and after weathering.

3.3.1 Changes in the Color of the Specimens

For the consumers’ eye, the most significant change during outdoor use of polymeric components, such as automotive parts, is the gradual change in the color of the components. Therefore, to evaluate macroscopic changes in the color of the specimens, their photographic images before and after weathering were compared as shown in Figure 3.20.

It is known that due to the fast cooling rate during injection molding of the specimens, PLA chains have no conformational ability to crystallize. Thus, Figure 3.21 shows that before weathering neat PLA looks very transparent owing to its amorphous structure. When 1 wt% HNT was added, the color turned into light brown, and increasing the HNT content resulted in darker brown.

After weathering, Figure 3.20 indicates that the color of the neat PLA and PLA/HNT nanocomposites all turned into milk-white, which should be due to both the changes in the chemical structure and the transition from amorphous to partially crystalline structure of PLA matrix. It is known that cold crystallization of PLA starts at around 70°C, which was the temperature level during UV irradiation cycles of accelerated weathering.

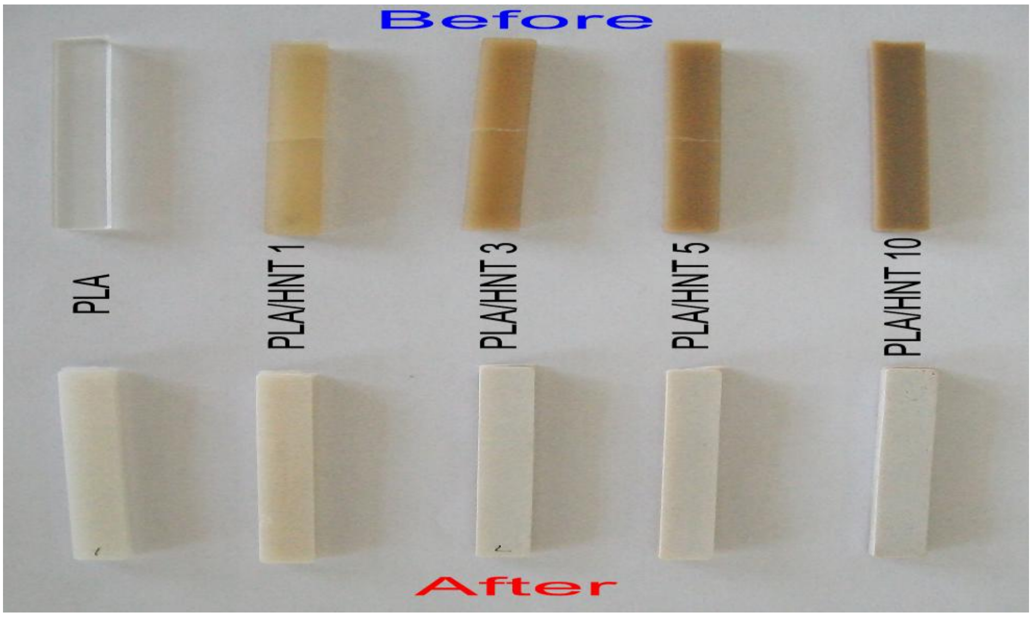

Figure 3.20 Macroscopic changes in the color of the specimens before and after weathering

As the second analysis, in order to have quantitative evaluation of the changes in the color of the specimens, CIELAB color space parameters L*, a*, b* and the total color difference parameter ΔE*, diffuse reflectance analysis (DRA) was applied to the surfaces of specimens before and after weathering. An example of color space graph determined by DRA is given in Figure 3.21, while the color parameters determined for all specimens are tabulated in Table 3.12.

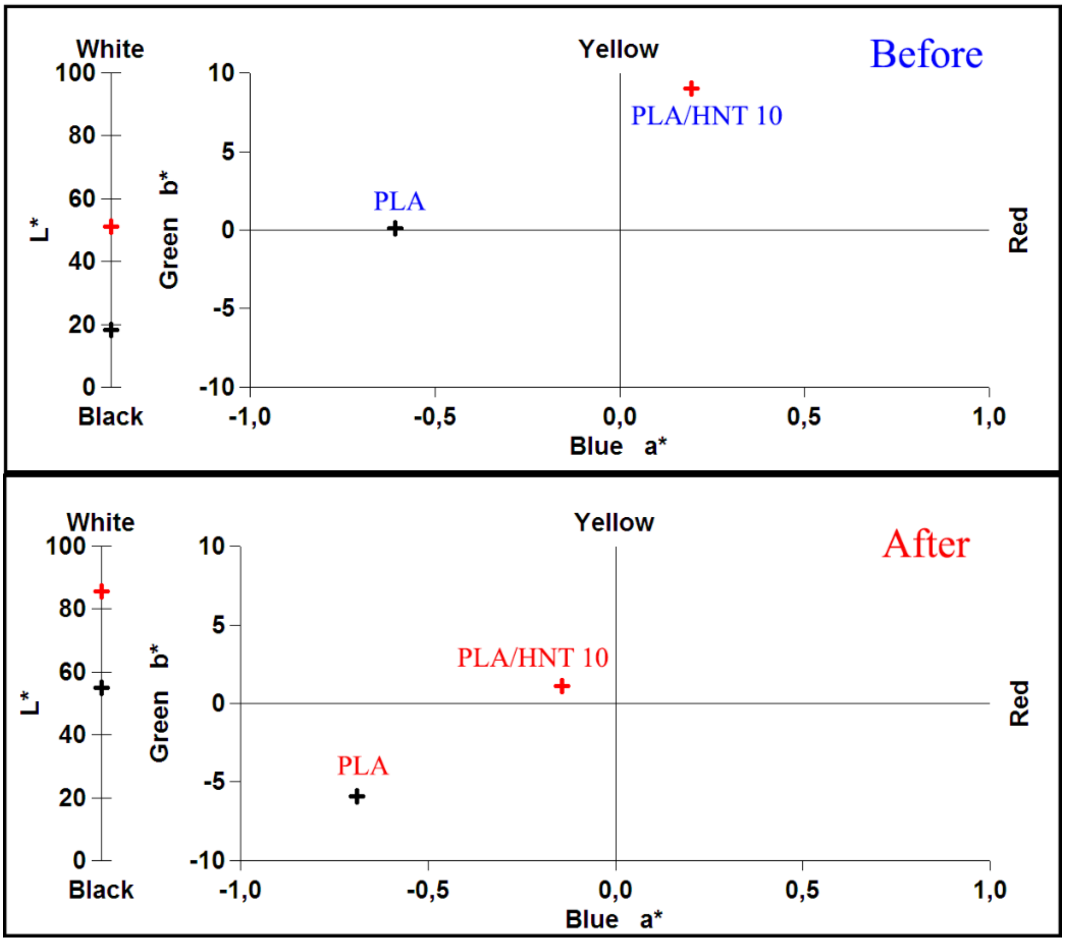

Figure 3.21 An example of the CIELAB color space graph for the neat PLA and PLA/HNT 10 nano-composite specimens before and after weathering obatined by DRA

Note that the color difference parameter ΔE* was determined using the following equation:

$$\Delta E^{*} = \sqrt{(L_2{}^{*} - L_1{}^{*})^2 + (a_2{}^{*} - a_1{}^{*})^2 + (b_2{}^{*} - b_1{}^{*})^2} \tag{12}$$

where the subscript "1" refers to "before weathering" and "2" refers to "after weathering".

Table 3.12 reveals that there were slight changes in the color parameter of a*, but significant decreases in b* and significant increases in L* which all lead to whiteness. Consequently, large changes in the color difference ΔE* values were also obtained. Therefore, it can be stated that macroscopic changes in the color of the specimens in Figure 3.20 was in accordance with the quantitative color space parameters in Table 3.12.

Table 3.12. CIELAB color space parameters (*L*, a*, b**) and color change difference (*ΔE**) values of the specimens before and after weathering determined by DRA

Specimens		**L***	**a***	**b***	**ΔE***
PLA	**Before**	18.34	-0.61	0.12	
	After	54.92	-0.69	-5.89	37.07
PLA/HNT 1	**Before**	27.88	-0.73	1.25	
	After	68.39	-0.76	-3.76	40.82
PLA/HNT 3	**Before**	38.88	-0.41	2.57	
	After	80.15	-0.40	-0.03	41.35
PLA/HNT 5	**Before**	45.00	-0.43	5.04	
	After	84.29	-0.35	0.89	39.50
PLA/HNT 10	**Before**	51.05	0.19	8.98	
	After	88.67	-0.14	1.08	38.44

3.3.2 Changes in the Chemical Structure of the Specimens

In order to reveal changes in the chemical structure of the specimens, ATR-FTIR analyses were conducted first for the neat PLA specimens before and after weathering as given in Figure 3.22. Before weathering, Figure 3.23 shows that IR spectrum of PLA has mainly five regions; the C-C stretching at 871 cm^{-1}, the C-O stretching peaks at 1265, 1180, 1129, 1090, 1045 cm^{-1}, the C-H deformation with peaks at 1360, 1370, 1384, 1454 cm^{-1}, C=O ester carbonyl groups at 1755 and 1760 cm^{-1}, and the C-H stretching at 2995, 2944, 2985 cm^{-1}. All these bands observed and tabulated in Table 3.13 were in well accordance with the ones discussed in the literature [14-18].

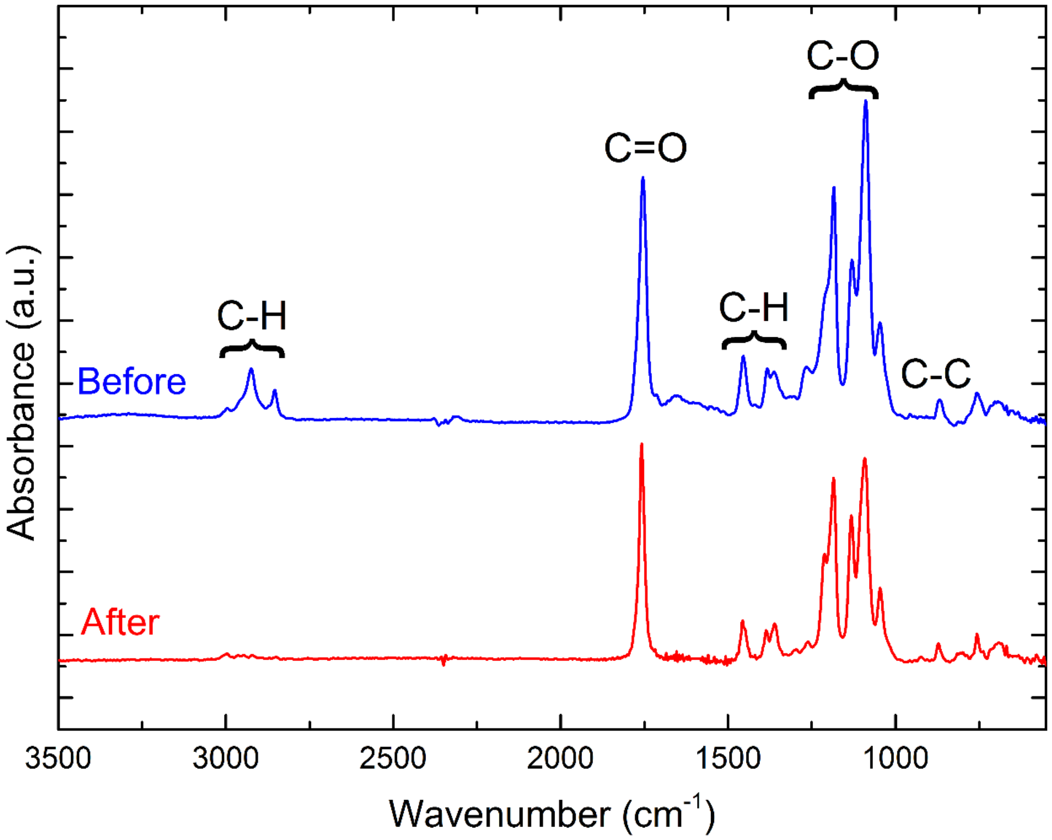

Figure 3.22 ATR-FTIR spectra of neat PLA specimens before and after weathering

Table 3.13. Positions and assignments of distinctive IR bands for PLA [14-18]

Position (cm^{-1})	**Assignments**
871	Stretching of C-C
1265, 1180, 1129, 1090, 1045	Stretching of C-O
1360, 1370, 1384, 1454	Deformation of C-H
1755, 1760	C=O of ester carbonyl groups
2995, 2944, 2985	Stretching of C-H

After weathering, Figure 3.22 reveals that intensities of all the distinctive IR bands of PLA were decreased due to the “photolysis” and “hydrolysis” actions leading to random main chain scission. Similar findings were also discussed in the literature [15-17].

It was also reported that the main consequences of the degradation mechanisms of “photo-oxidation” and/or “hydrolysis” leading to formation of carboxylic acid and ketones could be the shift of the ester carbonyl group C=O band from 1755 cm^{-1} to 1721 cm^{-1}, and the shift of C-O stretching of alcohol from 1090 cm^{-1} to 1050 cm^{-1}. However, shifts of these C=O and C-O band positions were not observed in this study. Therefore, it can be said that the main weathering degradation mechanisms observed in this study were by “photolysis” and partially by “hydrolysis”.

In order to determine whether there is any influence of HNT addition on the weathering degradation mechanisms of PLA, ATR-FTIR analyses were also utilized on all PLA/HNT nanocomposite specimens before and after weathering. In Figure 3.23, their IR spectra are given only after weathering.

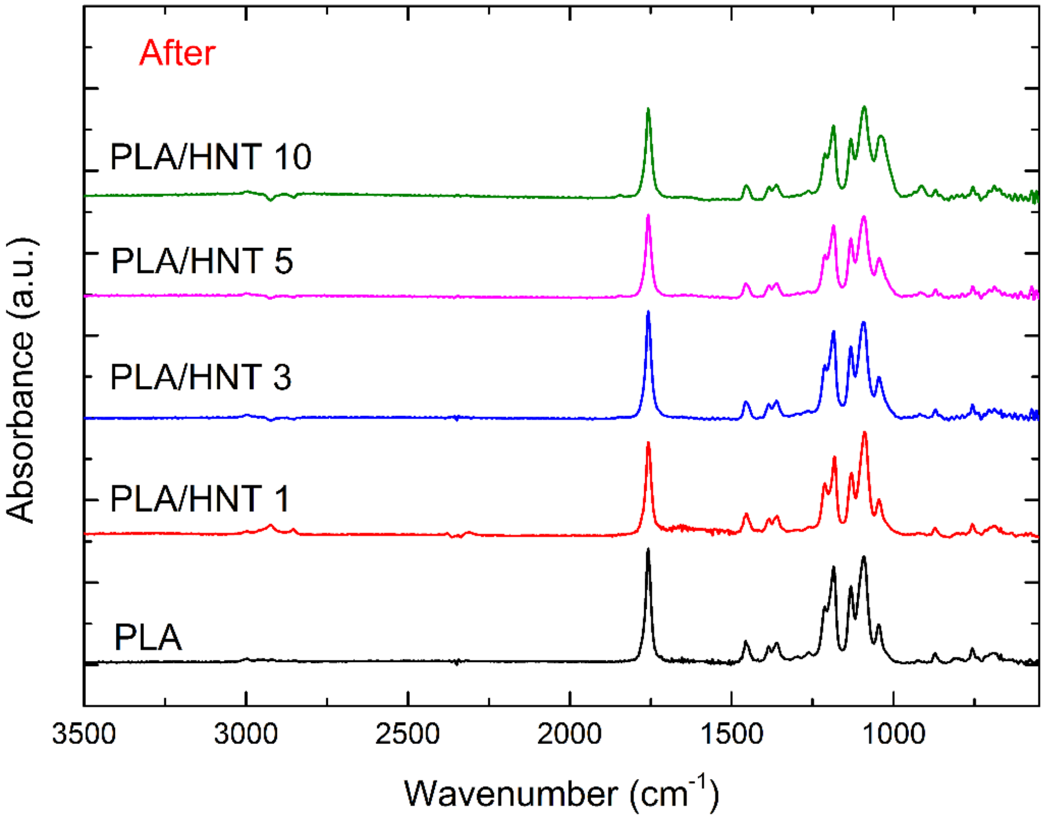

Figure 3.23 ATR-FTIR spectra of PLA and PLA/HNT nanocomposite specimens all after weathering

It was observed that the only change in the IR spectra of all PLA/HNT nanocomposite specimens was again decreased intensities of the distinctive IR bands of PLA. There was neither significant band position shifts nor formation of new bands. Therefore, it can be stated that addition of HNTs has no influence on the weathering degradation mechanisms of PLA.

3.3.3 Changes in the Mechanical Properties of the Specimens

In order to compare mechanical properties of the specimens before and after weathering, two important tests were conducted. The first one was "three-point bending" tests to determine "flexural strength, σ_{Flex}" and "flexural modulus, E_{Flex}" of the specimens. The second was "fracture toughness" tests to determine the toughness of the specimens in terms of "critical stress intensity factor K_{IC}" and "critical strain energy release rate G_{IC}". Flexural stress-strain curves of the specimens are given in Figure 3.24, while all the mechanical properties determined were tabulated in Table 3.14. Effects of HNT content on these properties were also evaluated in Figure 3.25.

Table 3.14. Flexural strength (σ_{Flex}), flexural modulus (E_{Flex}) and fracture toughness (K_{IC} and G_{IC}) of the specimens before and after weathering

Specimens		**E_{Flex} (GPa)**	**σ_{Flex} (MPa)**	**K_{IC} (MPa√m)**	**G_{IC} (kJ/m^2)**
PLA	**Before**	3.72 ± 0.08	64.17 ± 1.13	2.93 ± 0.14	3.75 ± 0.02
	After	3.82 ± 0.16	10.76 ± 0.32	0.27 ± 0.11	0.04 ± 0.02
PLA/HNT 1	**Before**	3.94 ± 0.09	69.97 ± 0.97	3.37 ± 0.02	4.94 ± 0.11
	After	3.82 ± 0.01	10.21 ± 0.17	0.32 ± 0.10	0.11 ± 0.01
PLA/HNT 3	**Before**	4.21 ± 0.04	70.71 ± 0.37	3.63 ± 0.01	5.79 ± 0.59
	After	3.83 ± 0.13	14.59 ± 0.67	0.32 ± 0.01	0.14 ± 0.03
PLA/HNT 5	**Before**	4.22 ± 0.09	67.32 ± 0.94	3.22 ± 0.03	4.26 ± 0.10
	After	3.98 ± 0.23	14.88 ± 0.07	0.67 ± 0.04	0.23 ± 0.10
PLA/HNT 10	**Before**	4.64 ± 0.08	65.39 ± 1.10	2.67 ± 0.04	2.42 ± 0.07
	After	4.33 ± 0.16	18.53 ± 2.08	0.84 ± 0.04	0.28 ± 0.11

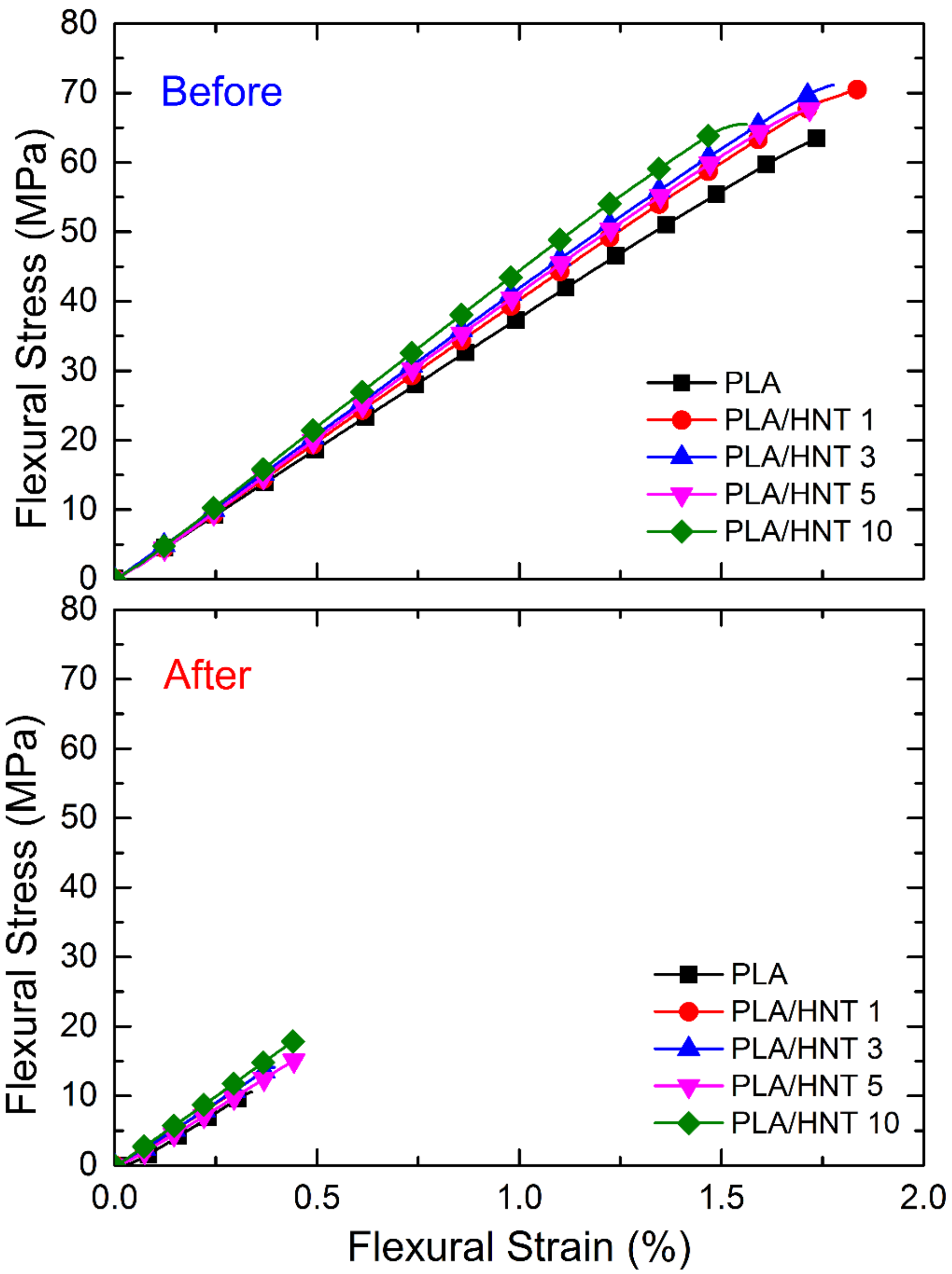

Figure 3.24 Flexural stress-strain curves of the specimens before and after the weathering tests

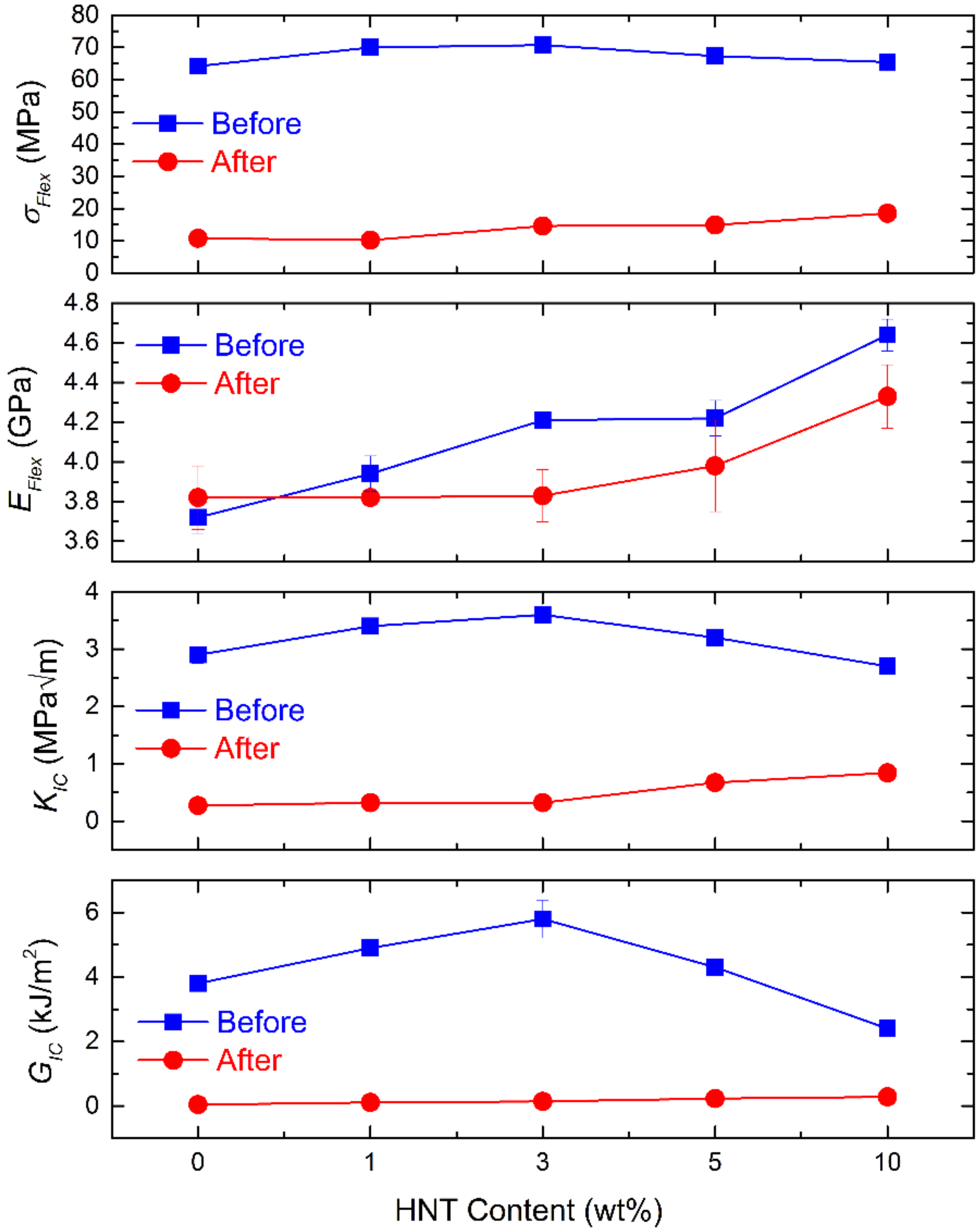

Figure 3.25 Effects of HNT content on the Flexural strength (σ_{Flex}), flexural modulus (E_{Flex}) and fracture toughness (K_{IC} and G_{IC}) of the specimens before and after weathering

Before weathering, these figures and the table show that incorporation of HNTs into PLA matrix increased all mechanical properties. For instance, addition of only 3 wt% HNT increased E_{Flex} and σ_{Flex} of neat PLA by 13% and 10%, respectively, while increases in the K_{IC} and G_{IC} fracture toughness values were as much as 24% and 54%, respectively.

Increases in modulus were due to the stiffening effect of rigid HNTs, while increases in strength were due to the efficient load transfer mechanism from the matrix to HNTs, and the decrease of the mobility of PLA chains by the high aspect ratio nanotubular structure of HNTs. Increases in fracture toughness values were again due to the very effective toughening mechanisms of HNTs via crack deflection, debonding, and pull-out. At higher HNT contents, due to the certain level of agglomeration of HNTs, the increases in strength and fracture toughness values started to decline.

After weathering, Figure 3.24, 3.25 and Table 3.13 indicate that severe actions of mainly photolysis and partly hydrolysis resulted in drastic reductions in the strength and fracture toughness values of the specimens. For instance, σ_{Flex} of neat PLA decreased from 64 MPa down to 10 MPa, i.e. a decrease of 6 times. Flexural strength of PLA/HNT nanocomposite specimens after weathering were in the range of 10-18 MPa, i.e. higher than that of neat PLA, however, this range is still very low to be used in engineering applications.

It was also seen that K_{IC} and G_{IC} fracture toughness values of neat PLA after weathering almost disappeared, values were just above zero. Values for PLA/HNT nanocomposite specimens were slightly higher, but still extremely low; this means that the specimens became extremely brittle, again not to be used for any application.

The only mechanical property which was not decreased after weathering was flexural modulus. E_{Flex}. As stated before, PLA matrix before weathering has amorphous structure. During weathering, UV irradiation cycles at 70°C resulted in crystallization of the PLA chains. Thus, it can be stated that the loss of stiffness of the structure due to photolysis and hydrolysis could be compensated by the stiffening effect of the partially crystalline structure of PLA matrix.

3.3.4 Changes in the Thermal Behavior of the Specimens

The first thermal analysis utilized for the specimens before and after weathering was DSC. The first heating thermograms given in Figure 3.26 were used to determine the important transition temperatures, i.e. “glass transition, cold crystallization, melting” (T_g , T_{cc} , T_w), together with “enthalpies of melting and cold crystallization” (ΔH_m and ΔH_{cc}) and they are tabulated in Table 3.15. This table also includes “percent crystallinity” (X_C) of the specimens obtained by using the following relation:

$$X_C = \frac{\Delta H_m - \Delta H_{cc}}{w_{PLA} \Delta H_m{}^{\circ}} \times 100 \tag{13}$$

where w_{PLA} is the weight fraction of the PLA matrix, while $\Delta H_m{}^{\circ}$ is the melting enthalpy of 100% crystalline PLA given as 93.1 J/g in the literature [71].

After weathering, Figure 3.26 and Table 3.15 indicate that due to the main chain scission effects of photolysis and partly hydrolysis glass transition T_g and melting temperature T_m of the specimens decreased. The decrease in T_g values were up to 7°C, while in T_m only 1-2°C.

However, the most significant influence of weathering observed in DSC analyses was the loss of cold crystallization. Figure 3.27 shows that exothermic peaks of the cold crystallization (ΔH_{cc}) of the specimens observed before weathering disappeared after weathering. Because, as stated before, very fast cooling rate of injection molding prevents crystallization of PLA chains leading to amorphous structure. During weathering, the temperature level and duration of UV irradiation cycles, which was

70°C and 8 hr, led to sufficient energy and time required for the conformational mobility of PLA chains to crystallize.

Table 3.15. Transition temperatures (T_g , T_{cc} , T_m), enthalpies (ΔH_m , ΔH_{cc}) and crystallinity percent (X_C) of the specimens before and after weathering obtained during the DSC first heating profiles

Specimens		T_g (°C)	T_{cc} (°C)	T_m (°C)	ΔH_m (J/g)	ΔH_{cc} (J/g)	X_C (%)
PLA	**Before**	67	102	169	38.18	25.21	13.93
	After	59	-	168	44.31	-	47.60
PLA/HNT 1	**Before**	64	98	170	37.17	16.56	22.36
	After	57	-	167	52.21	-	56.64
PLA/HNT 3	**Before**	63	99	168	36.08	13.83	24.64
	After	58	-	167	53.31	-	59.03
PLA/HNT 5	**Before**	64	95	169	35.09	14.71	23.04
	After	61	-	168	47.55	-	53.76
PLA/HNT 10	**Before**	63	93	169	35.54	16.44	22.80
	After	62	-	168	43.26	-	51.63

Therefore, after weathering, partial crystallinity amount (X_C) of neat PLA increased from 14% to 48%. Due to the additional nucleation site contribution of HNTs, the amount of crystallinity of the nanocomposites were even higher, reaching to 59% in the specimen of PLA/HNT 3, i.e. an increase of more than 4 times.

Thermal degradation behavior and thermomechanical properties of the specimens before and after weathering were compared by conducting TGA and DMA, as given in Figures 3.27 and 3.28, respectively. The values of the maximum mass loss rate degradation temperatures T_d of the specimens determined from TGA, and the storage modulus values E′ at 25°C and 50°C of the specimens determined from DMA were all tabulated in Table 3.16.

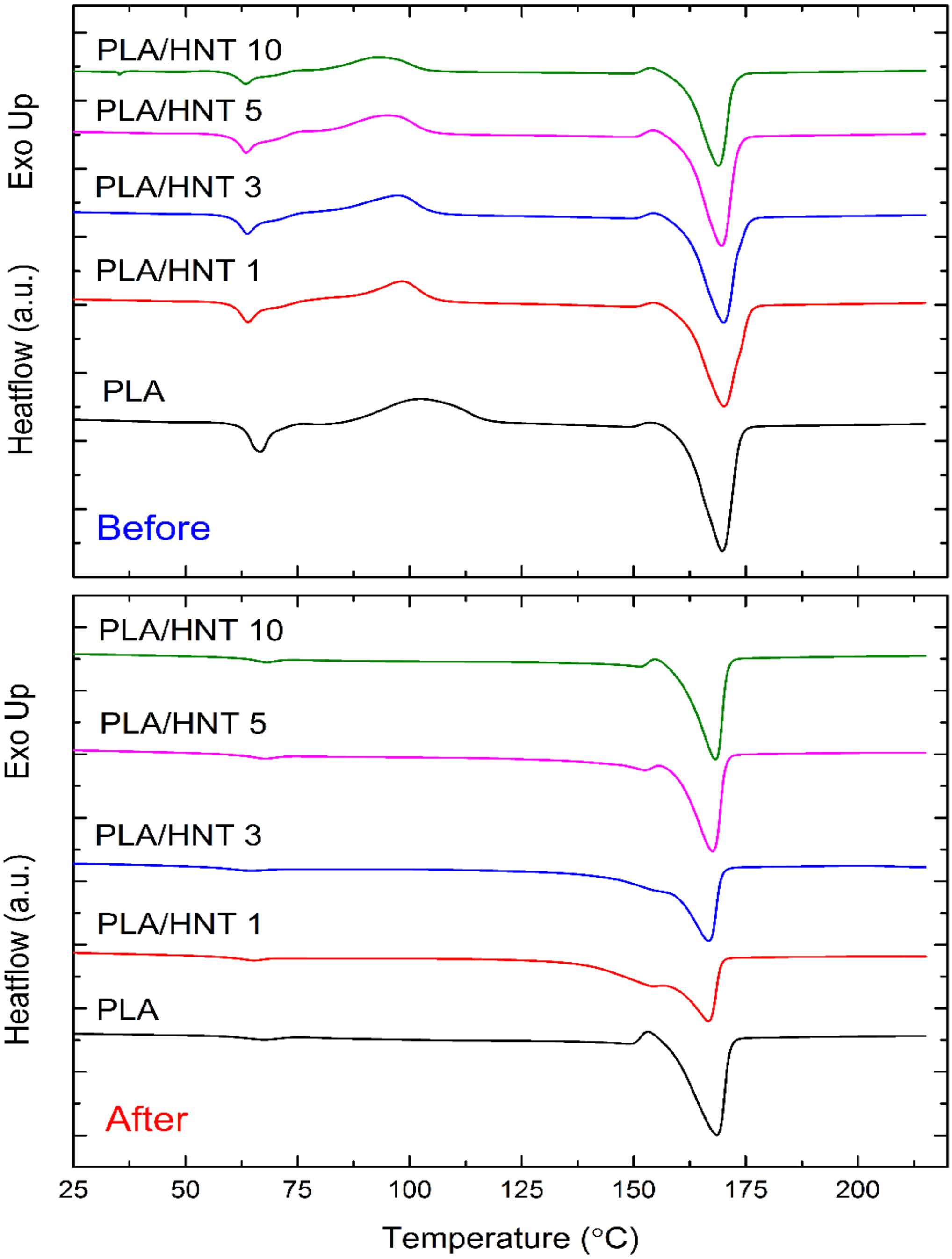

Figure 3.26 DSC first heating thermograms of the specimens before and after weathering

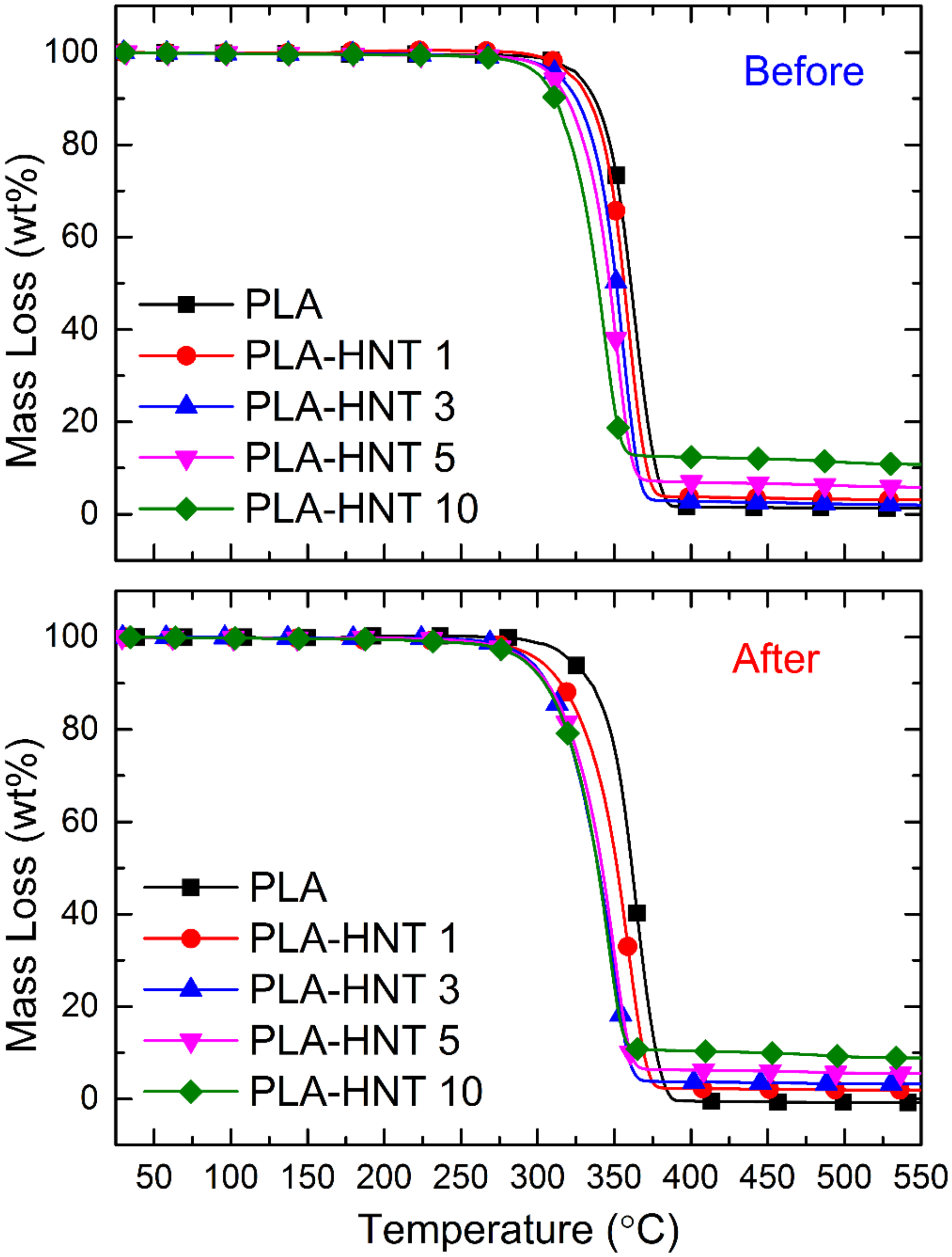

Figure 3.27 Thermogravimetric (TGA) curves of the specimens before and after weathering

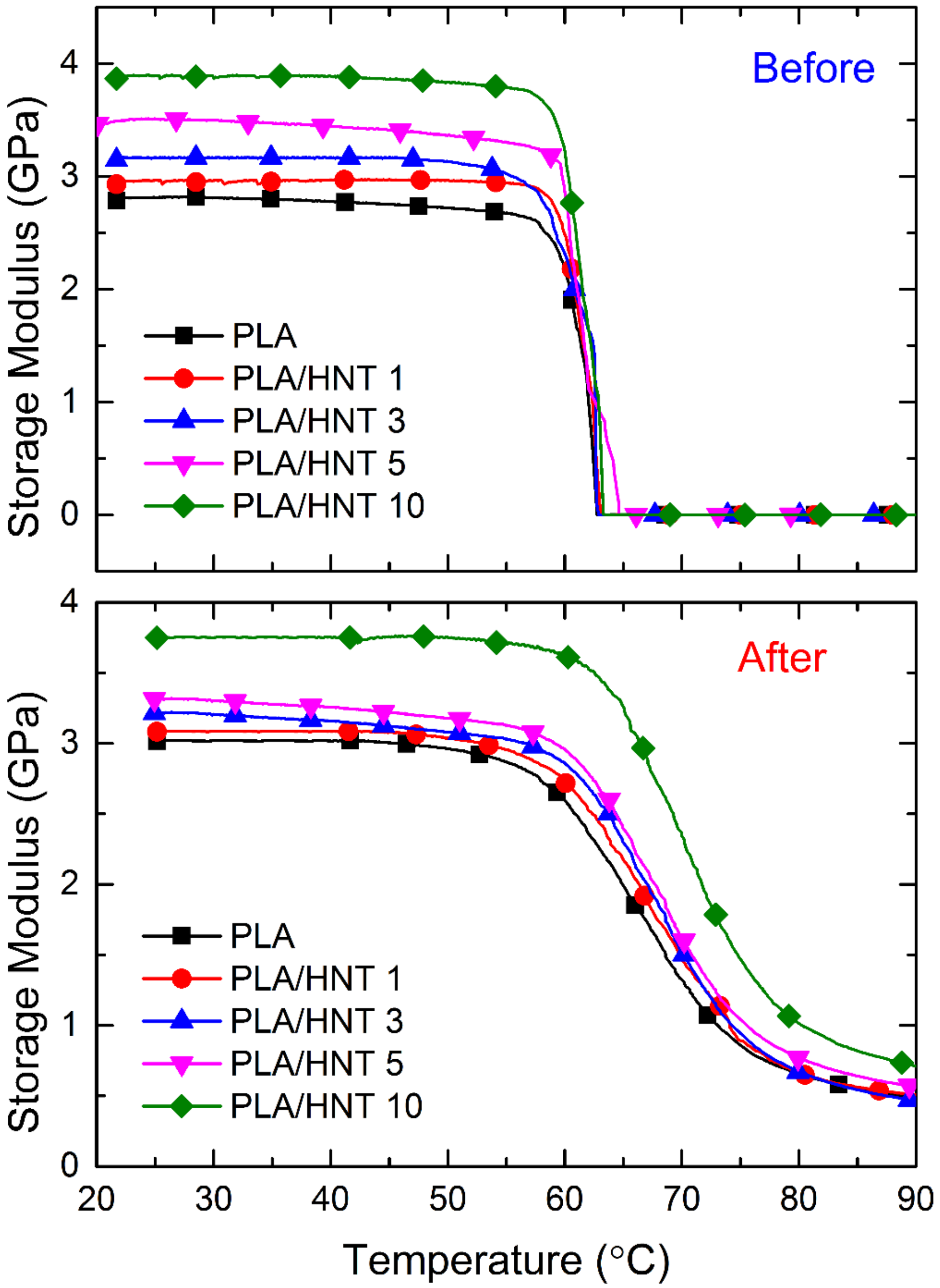

Figure 3.28 Storage modulus curves of the specimens before and after weathering obtained by DMA

Table 3.16. TGA thermal degradation temperatures (T_d) and DMA storage modulus (E′ at 25° and 50°C) of the specimens before and after weathering

Specimens		**T_d (°C)**	***E′* at 25 °C (GPa)**	***E′* at 50 °C (GPa)**
PLA	**Before**	366	2.78	2.72
	After	368	3.01	2.96
PLA/HNT 1	**Before**	362	2.97	2.96
	After	361	3.08	3.04
PLA/HNT 3	**Before**	358	3.16	3.09
	After	352	3.15	3.08
PLA/HNT 5	**Before**	354	3.47	3.35
	After	352	3.34	3.31
PLA/HNT 10	**Before**	346	3.89	3.84
	After	348	3.76	3.74

Before weathering, Figure 3.27 and Table 3.16 show that thermal degradation temperature T_d of neat PLA decreased gradually with the loading of HNT, basically due to release of the bound water molecules present in between the rolled walls of HNTs' tubular structure, as also discussed by Murariu et al. [52]. After weathering on the other hand, there was almost no further reduction in the T_d values of the specimens that should be due to the very high amount of partial crystallinity of the PLA matrix formed during weathering.

Before weathering, Figure 3.28 and Table 3.16 indicate that storage modulus values, i.e. both E' at 25°C and 50°C of neat PLA increased almost linearly with increasing HNT content, due to the very efficient strengthening mechanism of high aspect ratio nanotubular structure of HNTs. After weathering, it was seen that there was no reduction in the E' values of the specimens, again due to the higher crystallinity levels. That is, detrimental effects of main chain scission via weathering degradation mechanisms of photolysis and partly hydrolysis were compensated by the stiffening effect of higher crystallinity levels obtained during weathering.

CHAPTER 4

CONCLUSIONS

The main conclusions drawn from the three different parts of this thesis can be summarized as follows:

(i) Mechanical and Thermal Properties of PLA/HNT Nanocomposites

- By comparing the flexural mechanical properties of PLA/HNT 5 nanocomposite specimens produced by eight different procedures, it was concluded that three important compounding and shaping parameters, i.e. using “manual mixing” method as dry premixing, using “80 rpm” as twin-screw speed, and using “12 h” as drying time before injection molding, can be used as the optimum parameters.

- SEM studies revealed that HNTs can be uniformly distributed in the matrix at low filler contents; whereas there could be certain level of agglomeration above 5 wt%. It was also observed that HNTs were usually pulled-out basically due to the insufficient interfacial bonding with PLA matrix.

- Tension and bending tests indicated that elastic modulus values (Young’s modulus and flexural modulus) increased almost linearly with the increase of rigid and stiff HNT fillers. Strong and high aspect ratio structure of HNTs were also capable of making the composite strengthening mechanisms operative leading to increased levels of tensile strength and flexural strength values. For instance, using only 3 wt% HNT resulted in 25% increase in flexural modulus and 10% increase in flexural strength.

- Incorporation of HNTs was also very effective in compensating the brittleness problem of PLA. Due to the contribution of nano-scale toughening mechanisms, the increase in the fracture toughness values of PLA was as much as 54% with only 3 wt% HNT.

- DSC analyses indicated that HNTs might act as effective heterogeneous nucleation agents leading to two times increase in the crystallinity level of PLA. Although TGA revealed 10°-20°C decreases in the thermal degradation temperatures of PLA, DMA analyses showed that storage modulus values of PLA at 50°C could be increased by 39%.

- It can be generally concluded that use of industrially friendly melt compounding method (via twin-screw extruder) and melt shaping method (via injection molding) could be used successively in the production of PLA/HNT nanocomposites, and due to their improved mechanical and thermal properties, these nanocomposites could be used for many engineering applications.

(ii) Crystallization Kinetics of PLA/HNT Nanocomposites

- Isothermal melt crystallization procedure indicated that, due to heterogeneous nucleation effect, addition of HNTs resulted in higher crystallinity X_{ic} (up to 40% increase), and lower crystallization times t_{max} and $t_{1/2}$ (up to 2 times decreases for each) compared to neat PLA. Values of Avrami exponent n indicated that there is no influence of HNTs on the two-dimensional growth mechanism of PLA spherulites, while Avrami rate constant K of PLA increased more than 3 times with the addition of 10 wt% HNT.

- Non-isothermal melt crystallization procedure indicated that, heterogeneous nucleation action of HNTs were much more effective leading to increased crystallinity X_{nic} as much as 10 times more. Besides, HNTs shifted all temperature parameters (T_0, T_p, $T_{1/2}$) to higher temperatures, i.e. non-isothermal crystallization started at higher temperatures. HNTs also increased the value of modified Avrami exponent n above 3, which means that two-dimensional growth mechanism of PLA spherulites transformed into three-dimensional growth. Reciprocal of time ($1/t_{1/2}$) and modified Avrami rate constants K and K_C decreased with the addition of HNTs that could be due to the delayed conformational mobility of PLA chains by the physical barrier actions of HNTs.

- Crystallinity determinations of the injection molded and then annealed specimens by both DSC and XRD analyses indicated that, the highest crystallinity degree of PLA, i.e. 47%, could be reached by the addition of only 1 wt% HNT.

(iii) Accelerated Weathering of PLA/HNT Nanocomposites

- Macroscopic observations and quantitative measurements of the CIELAB color space parameters (L*, a*, b*) and color difference (ΔE*) values via DRA (diffused reflectance analysis) indicated that after weathering the color of the specimens turned into milk-white due to the chemical changes and crystallization of the PLA.

- Infrared spectroscopic analyses revealed that, after weathering, intensities of all the distinctive IR bands of PLA were decreased mainly due to the weathering degradation mechanisms of photolysis and partly due to hydrolysis, leading to random chain scission of the PLA macromolecular structure.

- Mechanical tests pointed out that weathering degradation could result in drastic reductions in the strength and toughness of PLA. For example flexural strength σ_{Flex} of PLA decreased 6 times, while the K_{IC} and G_{IC} fracture toughness values of PLA diminished to almost zero.

- After weathering, due to reinforcing actions of rigid HNTs, the mechanical properties of the PLA/HNT nanocomposite specimens were above the values of the neat PLA. However, these values were still very low to be used in engineering applications.

- DSC analyses revealed that due to the cold crystallization of the PLA matrix during UV irradiation cycles at 70°C, the total crystallinity amout of the specimens increased significantly, e.g. from 14% to 48% in neat PLA and to 59% in PLA/HNT 3 specimens.

- TGA, DMA and flexural tests also showed that, after weathering there were no reductions in the thermal degradation temperatures T_d, storage modulus E', and flexural modulus E_{Flex} values of the specimens. In these properties, detrimental effects of weathering degradation were compensated by the stiffening effect of higher crystallinity levels obtained during weathering.

Conclusive Remarks

First of all this thesis indicated that production of PLA/HNT nanocomposites is possible by using the industrially friendly twin-screw extruder melt compounding and injection molding shaping methods. It was also revealed that HNTs can improve performance of the PLA required for certain structural engineering applications mainly by decreasing the brittleness problem of PLA significantly. Moreover, by acting as heterogeneous nucleation agents, HNTs enhanced many crystallization parameters of PLA.

On the other hand, compared to outdoor performance of other engineering polymers such as polyamide, accelerated weathering tests indicated that, PLA has rather very weak resistance to UV irradiation and humidity leading to very drastic decreases in mechanical properties. Addition of HNTs have slight influences, but not sufficient for long term outdoor use.

REFERENCES

[1] Lasprilla, A. J. R., Martinez, G. A. R., Lunelli, B. H., Figueroa, J. E. J., Jardini, A. L., Filho, R. M., Synthesis and Characterization of Poly (Lactic Acid) for Use in Biomedical Field, *The Italian Association of Chemical Engineering,*

[2] Porter, K. A., Ring Opening Polymerization of Lactide for The synthesis of Poly (Lactic Acid), 2006.

[3] Drumright, R. E., Gruber, P. R., Henton, D. E., Polylactic Acid Technology, *Advanced Materials,* 12:1841-1846, 2000.

[4] Hoogsteen, W., Postema, A. R., Pennings, A.J., ten Brinke, G., Crystal Structure, Conformation, and Morphology of Solution-Spun Poly(L-lactide) Fibers, *Macromolecules,* 23:634-642, 1990.

[5] Sawai, D., Takahashi, K., Sasashige, A., Kanamoto, T., Preparation of Oriented β-Form Poly(L-lactic acid) by Solid-State Coextrusion: Effect of Extrusion Variables, *Macromolecules,* 36:3601-3605, 2003.

[6] Puiggali, J., Ikada, Y., Tsuji, H., Cartier, L., Okihara, T., Lotz, B., The frustrated structure of poly(l-lactide), *Polymer*, 41:8921-8930, 2000.

[7] Brizzolara, D., Cantow, H., Diederichs, K., Keller, E., Domb, A. J., Mechanism of the Stereocomplex Formation between Enantiomeric Poly(lactide)s, *Macromolecules,* 29:191-197, 1996.

[8] Cartier, L., Okihara, T., Ikada, Y., Tsuji, H., Puiggali, J., Lotz, B., Epitaxial crystallization and crystalline polymorphism of polylactides, *Polymer*, 41:8909-8919, 2000

[9] Kishore, K., Vasanthakumari, R., Isothermal Melting Behavior of Poly(L-Lactic Acid), *Journal of Polymer Science: Polymer Physics Edition*, 22:537-542, 1984.

[10] DE SANTIS, P., J. KOVACS, A., Molecular Conformation of Poly (S-lactic Acid), *Biopolymers*, 6:299-306, 1968.

[11] Marega, C., Marigo, A., Di Noto, V., Zannetti, R. , Structure and crystallization kinetics of poly(Lactic acid), *Makromolekulare chemie-macromolecular chemistry and physics (Makromol. Chem.)*, 193:1599-1606, 1992.

[12] Zhang, J., Tashiro, K., Domb, A.J., Tsuji, H., Confirmation of Disorder α Form of Poly(L-lactic acid) by the X-ray Fiber Pattern and Polarized IR/Raman Spectra Measured for Uniaxially-Oriented Samples, *Macromolecular Symposia*, 242:274-278, 2006.

[13] Zhang, J., Tashiro, K., Tsuji, H.,. Domb, A. J , Disorder-to-Order Phase Transition and Multiple Melting Behavior of Poly(L-lactide) Investigated by Simultaneous Measurements of WAXD and DSC, *Macromolecules*, 41:1352-1357, 2008.

[14] Ikada, E., Photo- and Bio-degradable Polyester. Photodegradation Behaviors of Aliphatic Polyesters, *Journal of Photopolymer Science and Technology*, 10:265-270, 1997.

[15] Janorkar, A. V., Metters, A. T., Hirt, D. E., Degradation of poly(L-lactide) films under ultraviolet-induced photografting and sterilization conditions, *Journal of Applied Polymer Science*, 106: 1042-1047, 2007.

[16] Copinet, A., Bertrand, C., Govindin, S., Coma, V.Couturier, Y., Effects of ultraviolet light (315 nm), temperature and relative humidity on the degradation of polylactic acid plastic films, *Chemosphere*, 55: 763-73, 2004.

[17] Ndazi, B. S., Characterization of hydrolytic degradation of polylactic acid/rice hulls composites in water at different temperatures, *eXPRESS Polymer Letters*, 5: 119-131, 2011.

[18] Shinzawa, H., Nishida, M., Tanaka, T.Kanematsu, W., Accelerated weathering-induced degradation of poly(lactic acid) fiber studied by near-infrared (NIR) hyperspectral imaging, *Applied spectroscopy*, 66: 470-4, 2012.

[19] Spiridon, I., Paduraru, O. M., Zaltariov, M. F., Darie, R. N., Influence of Keratin on Polylactic Acid/Chitosan Composite Properties. Behavior upon Accelerated Weathering, *Industrial & Engineering Chemistry Research*, 52: 9822-9833, 2013.

[20] Joussein, E., Petit, S., Churchman, J., Theng, B., Righi, D., Delvaux, B., Halloysite clay minerals, a review, *Clay Minerals*, 40: 383-426, 2005.

[21] Cheng, H., Yang, J., Liu, Q., He, J., Frost, R. L., Thermogravimetric analysis–mass spectrometry (TG–MS) of selected Chinese kaolinites, *Thermochimica Acta*, 507-508: 106-114, 2010.

[22] Hope, E. W., Kittrick, J. A., Surface Tension And The Morphology Of Halloysite, *The American Mineralogist*, 49: 859-866, 1964.

[23] Wada, S., Mizota, C., Iron-rich halloysite (10Å) with crumpled lamellar morphology from Hokkaido, Japan, *Clays and Clay Minerals*, 30: 315-317, 1982.

[24] Papoulis, D., Tsolis-Katagas, P., Kalampounias, A. G., Tsikouras, B., Progressive formation of halloysite from the hydrothermal alteration of biotite and the formation mechanisms of anatase in altered volcanic rocks from Limnos Island, northeast Aegean Sea, Greece, *Clays and Clay Minerals,* 57:566-577, 2009.

[25] Cheng, H., Frost, R. L., Yang, J., Liu, Q.He, J., Infrared and infrared emission spectroscopic study of typical Chinese kaolinite and halloysite, *Spectrochimica acta. Part A, Molecular and biomolecular spectroscopy*, 77:1014-20, 2010.

[26] Frost, R.L., Shurvell, H.F., Raman Microprobe Spectroscopy of Halloysite, *Clays and Clay Minerals,* 45: 68-72, 1997.

[27] Kristof, J., Frost, R.L., Felinger, A., Mink, J., FTIR spectroscopic study of intercalated kaolinite, *Journal of Molecular Structure*, 410-411: 119-122, 1997.

[28] Kadi, S., Lellou, S., Marouf-Khelifa, K., Schott, J., Gener-Batonneau, I.Khelifa, A., Preparation, characterisation and application of thermally treated Algerian halloysite, *Microporous and Mesoporous Materials,* 158:47-54, 2012.

[29] Luo, P., Zhang, B., Zhao, Y., Wang, J., Zhang, H., Liu, J., Removal of methylene blue from aqueous solutions by adsorption onto chemically activated halloysite nanotubes, *Korean Journal of Chemical Engineering*, 28:800-807, 2011.

[30] Alamri, H.Low, I. M., Effect of water absorption on the mechanical properties of nano-filler reinforced epoxy nanocomposites, *Materials & Design*, 42:214-222, 2012.

[31] Jia, Z., Luo, Y., Guo, B., Yang, B., Du, M., Jia, D., Reinforcing and Flame-Retardant Effects of Halloysite Nanotubes on LLDPE, *Polymer-Plastics Technology and Engineering*, 48: 607-613, 2009.

[32] Yuan, P., Southon, P.D., Liu, Z., Green, M. E. R., Hook, J. M., Anthill, S. J., Kepert, C. J., Functionalization of Halloysite Clay Nanotubes by Grafting with γ-aminopropyltriethoxysilane, *Journal of Physical Chemistry,* 112: 15742-15751, 2008.

[33] He, Y., Kong, W., Wang, W., Liu, T., Liu, Y., Gong, Q., Gao, J., Modified natural halloysite/potato starch composite films, *Carbohydrate Polymers,* 87:2706-2711, 2012.

[34] Carli, L. N., Crespo, J. S., Mauler, R. S., PHBV nanocomposites based on organomodified montmorillonite and halloysite: The effect of clay type on the morphology and thermal and mechanical properties, *Composites Part A: Applied Science and Manufacturing*, 42: 1601-1608, 2011.

[35] Guo, B., Liu, X., Zhou, W. Y., Lei, Y., Jia, D., Adsorption of Ionic Liquid onto Halloysite Nanotubes: Mechanism and Reinforcement of the Modified Clay to Rubber, *Journal of Macromolecular Science, Part B,* 49: 1029-1043, 2010.

[36] Ismail, H., Salleh, S.Z., Ahmad, Z., Curing Characteristics, Mechanical, Thermal, and Morphological Properties of Halloysite Nanotubes (HNTs)-Filled Natural Rubber Nanocomposites, *Polymer-Plastics Technology and Engineering*, 50: 681-688, 2011.

[37] Liu, M., Zhang, Y., Wu, C., Xiong, S.Zhou, C., Chitosan/halloysite nanotubes bionanocomposites: structure, mechanical properties and biocompatibility, *International journal of biological macromolecules*, 51:566-75, 2012.

[38] Ning, N., Yin, Q., Luo, F., Zhang, Q., Du, R., Fu, Q., Crystallization behavior and mechanical properties of polypropylene/halloysite composites, *Polymer*, 48: 7374-7384, 2007.

[39] Zhang, L., Wang, T., Liu, P., Polyaniline-coated halloysite nanotubes via in-situ chemical polymerization, *Applied Surface Science*, 255: 2091-2097, 2008.
[40] Rooj, S., Das, A., Heinrich, G., Tube-like natural halloysite/fluoroelastomer nanocomposites with simultaneous enhanced mechanical, dynamic mechanical and thermal properties, *European Polymer Journal*, 47:1746-1755, 2011.

[41] Erdogan, A. R., Kaygusuz, I. Kaynak, C., Influences of aminosilanization of halloysite nanotubes on the mechanical properties of polyamide-6 nanocomposites, *Polymer Composites*, 35: 1350-1361, 2014.

[42] Nieddu, Erika, Mazzucco, L., Gentile, P., Benko, T., Balbo, V., Mandrile, R.Ciardelli, G., Preparation and biodegradation of clay composites of PLA, *Reactive and Functional Polymers*, 69:371-379, 2009.

[43] Chang, J., An, Y.U., Sur, G. S. , Poly(lactic acid) Nanocomposites with Various Organoclays. I. Thermomechanical Properties, Morphology, and Gas Permeability, *Journal of Polymer Science: Part B: Polymer Physics*, 41: 94–103, 2003.

[44] Fukushima, K., Tabuani, D.Camino, G., Nanocomposites of PLA and PCL based on montmorillonite and sepiolite, *Materials Science and Engineering: C*, 29:1433-1441, 2009.

[45] Wu, Defeng, Wu, Liang, Zhou, Weidong, Zhang, MingYang, Tao, Crystallization and biodegradation of polylactide/carbon nanotube composites, *Polymer Engineering & Science*, 50:1721-1733, 2010.

[46] Fukushima, K., Tabuani, D., Abbate, C., Arena, M.Rizzarelli, P., Preparation, characterization and biodegradation of biopolymer nanocomposites based on fumed silica, *European Polymer Journal*, 47:139-152, 2011.

[47] Qi, R., Guo, R., Shen, M., Cao, X., Zhang, L., Xu, J., Yu, J., Shi, X., Electrospun poly(lactic-co-glycolic acid)/halloysite nanotube composite nanofibers for drug encapsulation and sustained release, *Journal of Materials Chemistry*, 20: 10622, 2010.

[48] Dong, Y., Chaudhary, D., Haroosh, H.Bickford, T., Development and characterisation of novel electrospun polylactic acid/tubular clay nanocomposites, *Journal of Materials Science*, 46: 6148-6153, 2011.

[49] Roy, P. K., Hakkarainen, M., Albertsson, A., Nanoclay effects on the degradation process and product patterns of polylactide, *Polymer Degradation and Stability*, 97:1254-1260, 2012.

[50] Isitman, N. A., Dogan, M., Bayramli, E., Kaynak, C., The role of nanoparticle geometry in flame retardancy of polylactide nanocomposites containing aluminium phosphinate, *Polymer Degradation and Stability*, 97:1285-1296, 2012.

[51] Matusik, J., Stodolak, E., Bahranowski, K., Synthesis of polylactide/clay composites using structurally different kaolinites and kaolinite nanotubes, *Applied Clay Science*, 51: 102-109, 2011.

[52] Murariu, M., Dechief, A., Paint, Y., Peeterbroeck, S., Bonnaud, L., Dubois, P., Polylactide (PLA)—Halloysite Nanocomposites: Production, Morphology and Key-Properties, *Journal of Polymers and the Environment*, 20: 932-943, 2012.

[53] Liu, M., Zhang, Y., Zhou, C., Nanocomposites of halloysite and polylactide, *Applied Clay Science*, 75-76: 52-59, 2013.

[54] Iannace, S., Nicolais, L., Isothermal Crystallization And Chain Mobility Of Poly (L-Lactide), *Journal Of Applied Polymer Science*, 64: 911-919, 1997.

[55] Di Lorenzo, Maria Laura, Crystallization behavior of poly(l-lactic acid), *European Polymer Journal*, 41:569-575, 2005.

[56] Xiao, Hanwen, Liu, Fen, Jiang, TaoYeh, Jen-Taut, Kinetics and crystal structure of isothermal crystallization of poly(lactic acid) plasticized with triphenyl phosphate, *Journal of Applied Polymer Science*, n/a-n/a, 2010.

[57] Shi, Q. F., Mou, H. Y., Gao, L., Yang, J.Guo, W. H., Double-Melting Behavior of Bamboo Fiber/Talc/Poly (Lactic Acid) Composites, *Journal of Polymers and the Environment*, 18:567-575, 2010.

[58] Xiao, H. W., Li, Peng, Ren, Xiaomin, Jiang, TaoYeh, Jen-Taut, Isothermal crystallization kinetics and crystal structure of poly(lactic acid): Effect of triphenyl phosphate and talc, *Journal of Applied Polymer Science*, 118:3558-3569, 2010.

[59] Liao, Ruogu, Yang, Bin, Yu, WeiZhou, Chixing, Isothermal cold crystallization kinetics of polylactide/nucleating agents, *Journal of Applied Polymer Science*, 104:310-317, 2007.

[60] Katiyar, Vimal, Gerds, Nathalie, Koch, Christian Bender, Risbo, Jens, Hansen, Hans Christian B.Plackett, David, Melt processing of poly(L-lactic acid) in the presence of organomodified anionic or cationic clays, *Journal of Applied Polymer Science*, 122:112-125, 2011.

[61] As’habi, Ladan, Jafari, Seyed Hassan, Khonakdar, Hossein Ali, Häussler, Liane, Wagenknecht, UdoHeinrich, Gert, Non-isothermal crystallization behavior of PLA/LLDPE/nanoclay hybrid: Synergistic role of LLDPE and clay, *Thermochimica Acta*, 565:102-113, 2013.

[62] Park, Sang Ho, Lee, Seung GooKim, Seong Hun, Isothermal crystallization

behavior and mechanical properties of polylactide/carbon nanotube nanocomposites, *Composites Part A: Applied Science and Manufacturing*, 46:11-18, 2013.

[63] Tang, H., Chen, J. B., Wang, Y., Xu, J. Z., Hsiao, B. S., Zhong, G. J.Li, Z. M., Shear flow and carbon nanotubes synergistically induced nonisothermal crystallization of poly(lactic acid) and its application in injection molding, *Biomacromolecules*, 13:3858-67, 2012.

[64] Zaidi, Lynda, Kaci, Mustapha, Bruzaud, Stéphane, Bourmaud, AlainGrohens, Yves, Effect of natural weather on the structure and properties of polylactide/Cloisite 30B nanocomposites, *Polymer Degradation and Stability*, 95:1751-1758, 2010.

[65] Jandas, P. J., Mohanty, S.Nayak, S. K., Sustainability, Compostability, and Specific Microbial Activity on Agricultural Mulch Films Prepared from Poly(lactic acid), *Industrial & Engineering Chemistry Research*, 52:17714-17724, 2013.

[66] Islam, M. S., Pickering, K. L.Foreman, N. J., Influence of accelerated ageing on the physico-mechanical properties of alkali-treated industrial hemp fibre reinforced poly(lactic acid) (PLA) composites, *Polymer Degradation and Stability*, 95:59-65, 2010.

[67] Yew, G. H., Chow, W. S., Mohd Ishak, Z. A.Mohd Yusof, A. M., Natural Weathering of Poly (Lactic Acid): Effects of Rice Starch and Epoxidized Natural Rubber, *Journal of Elastomers and Plastics*, 41:369-382, 2009.

[68] Grigsby, Warren, Bridson, James, Lomas, ColeElliot, Jaime-Anne, Esterification of Condensed Tannins and Their Impact on the Properties of Poly(Lactic Acid), *Polymers*, 5:344-360, 2013.

[69] Bolio-Lopez, G.I., Veleva, L., Valadez-Gonzalez, A., Quintana-Owen, P., Weathering And Biodegradatıon Of Polylactic Acid Composite Reinforced With Cellulosewhiskers, *Revista Mexicana de Ingeniería Química*, 12: 143-153, 2013.

[70] Q-Lab Corporation, QUV Accelerated Weathering Tester Technical Manual, 2012.

[71] Fischer E-W, Sterzel H-J, Wegner G. Investigation of Structure of Solution Grown Crystals of Lactide Copolymers by Means of Chemical Reactions. *Colloid and Polymer Science*, 251:980-990, 1973.

[72] Wu, D., Wu, L., Wu, L., Xu, B., Zhang, Y., Zhang, M., Nonisothermal cold crystallization behavior and kinetics of polylactide/clay nanocomposites, *Journal of Polymer Science Part B: Polymer Physics*, 45, 1100-1113, 2007.

[73] Mano, J. F., Wang, Y., Viana, J. C., Denchev, Z., Oliveira, M. J., Cold Crystallization of PLLA Studied by Simultaneous SAXS and WAXS, *Macromolecular Materials and Engineering*, 289: 910-915, 2004.

[74] Zhang, J., Tsuji, H., Noda, I., Ozaki, Y., Structural Changes and Crystallization Dynamics of Poly(L-lactide) during the Cold-Crystallization Process Investigated by Infrared and Two-Dimensional Infrared Correlation Spectroscopy, *Macromolecules*, 37: 6433-6439, 2004.

[75] Jeziorny A., Parameters Characterizing Kinetics of Non-isothermal Crystallization of Poly(Ethylene-Terephthalate) Determined by DSC, *Polymer*, 19(10): 1142-1144, 1978.

[76] Du, M., Guo, B., Wan, J., Zou, Q., Jia, D., Effects of halloysite nanotubes on kinetics and activation energy of non-isothermal crystallization of polypropylene, *Journal of Polymer Research*, 17: 109-118, 2009.